NAVAL POSTGRADUATE SCHOOL

MONTEREY, CALIFORNIA

THESIS

AN EVALUATION OF SEA ICE DEFORMATION AND ITS SPATIAL CHARACTERISTICS FROM THE REGIONAL ARCTIC SYSTEM MODEL

by

Thomas J. Mills

December 2012

Thesis Co-Advisors: Wieslaw Maslowski
                                                     Andrew Roberts

Approved for public release; distribution is unlimited

THIS PAGE INTENTIONALLY LEFT BLANK

REPORT DOCUMENTATION PAGE		*Form Approved OMB No. 0704–0188*

Public reporting burden for this collection of information is estimated to average 1 hour per response, including the time for reviewing instruction, searching existing data sources, gathering and maintaining the data needed, and completing and reviewing the collection of information. Send comments regarding this burden estimate or any other aspect of this collection of information, including suggestions for reducing this burden, to Washington headquarters Services, Directorate for Information Operations and Reports, 1215 Jefferson Davis Highway, Suite 1204, Arlington, VA 22202–4302, and to the Office of Management and Budget, Paperwork Reduction Project (0704–0188) Washington, DC 20503.

1. AGENCY USE ONLY *(Leave blank)*	2. REPORT DATE December 2012	3. REPORT TYPE AND DATES COVERED Master's Thesis
4. TITLE AND SUBTITLE AN EVALUATION OF SEA ICE DEFORMATION AND ITS SPATIAL CHARACTERISTICS FROM THE REGIONAL ARCTIC SYSTEM MODEL		5. FUNDING NUMBERS
6. AUTHOR(S) Thomas J. Mills		

7. PERFORMING ORGANIZATION NAME(S) AND ADDRESS(ES)
    Naval Postgraduate School
    Monterey, CA 93943–5000
		8. PERFORMING ORGANIZATION REPORT NUMBER

9. SPONSORING /MONITORING AGENCY NAME(S) AND ADDRESS(ES) N/A		10. SPONSORING/MONITORING AGENCY REPORT NUMBER

11. SUPPLEMENTARY NOTES The views expressed in this thesis are those of the author and do not reflect the official policy or position of the Department of Defense or the U.S. Government. IRB Protocol number ____N/A____.

12a. DISTRIBUTION / AVAILABILITY STATEMENT Approved for public release; distribution is unlimited	12b. DISTRIBUTION CODE A

13. ABSTRACT (maximum 200 words)

The Regional Arctic System Model (RASM) is used to investigate the process and frequency of extreme sea ice shear deformation events resulting in pycnocline upwelling due to Ekman pumping as described in McPhee et al. (2005). RASM is a fully coupled land, atmosphere, sea ice, and ocean model with high spatial and temporal resolution. Time series analysis of the upper ocean temperature structure, basal melt rate, total deformation rate, and ice-ocean stress curl yield the identification of individual events. Shear deformation events generate an upper ocean response given a positive ice-ocean stress curl, i.e., induced by counterclockwise rotation in the ice velocity field relative to the underlying ocean. Spatial and temporal characterization of the total deformation rate indicates that fine spatial and temporal resolution, on a statistical scale, is important for the energy budget of the Arctic. Results demonstrate a power law relationship between the mean deformation rate and length scale. This is hypothesized as being due to RASMs fully coupled system allowing for naturally occurring high frequency noise and the cascade of energy among model components. Simulated events are infrequent and their relative impact on large scale energy exchange remains undetermined, which warrants further research of these phenomena.

14. SUBJECT TERMS Arctic Ocean, Sea Ice, RASM, Coupled Ice-Ocean Model, Sea Ice Dynamics, Sea Ice Thickness Distribution, Sea Ice Variability	15. NUMBER OF PAGES 196
	16. PRICE CODE

17. SECURITY CLASSIFICATION OF REPORT Unclassified	18. SECURITY CLASSIFICATION OF THIS PAGE Unclassified	19. SECURITY CLASSIFICATION OF ABSTRACT Unclassified	20. LIMITATION OF ABSTRACT UU

i

THIS PAGE INTENTIONALLY LEFT BLANK

AN EVALUATION OF SEA ICE DEFORMATION AND ITS SPATIAL CHARACTERISTICS FROM THE REGIONAL ARCTIC SYSTEM MODEL

Thomas J. Mills
Lieutenant, United States Navy
B.S., University of Colorado, 2005
M.S., National University of Singapore, 2012

Submitted in partial fulfillment of the
requirements for the degree of

MASTER OF SCIENCE IN METEOROLOGY AND PHYSICAL OCEANOGRAPHY

from the

NAVAL POSTGRADUATE SCHOOL
December 2012

Author: Thomas J. Mills

Approved by: Wieslaw Maslowski
                 Thesis Co-Advisor

                 Andrew Roberts
                 Thesis Co-Advisor

                 Peter Chu
                 Chair, Department of Oceanography

iii

THIS PAGE INTENTIONALLY LEFT BLANK

ABSTRACT

The Regional Arctic System Model (RASM) is used to investigate the process and frequency of extreme sea ice shear deformation events resulting in pycnocline upwelling due to Ekman pumping as described in McPhee et al. (2005). RASM is a fully coupled land, atmosphere, sea ice, and ocean model with high spatial and temporal resolution. Time series analysis of the upper ocean temperature structure, basal melt rate, total deformation rate, and ice-ocean stress curl yield the identification of individual events. Shear deformation events generate an upper ocean response given a positive ice-ocean stress curl, i.e., induced by counterclockwise rotation in the ice velocity field relative to the underlying ocean. Spatial and temporal characterization of the total deformation rate indicates that fine spatial and temporal resolution, on a statistical scale, is important for the energy budget of the Arctic. Results demonstrate a power law relationship between the mean deformation rate and length scale. This is hypothesized as being due to RASMs fully coupled system allowing for naturally occurring high frequency noise and the cascade of energy among model components. Simulated events are infrequent and their relative impact on large scale energy exchange remains undetermined, which warrants further research of these phenomena.

THIS PAGE INTENTIONALLY LEFT BLANK

TABLE OF CONTENTS

LIST OF FIGURES

LIST OF TABLES

THIS PAGE INTENTIONALLY LEFT BLANK

LIST OF ACRONYMS AND ABBREVIATIONS

AAR	AMAP Assessment Report
AC	Anadyr Current
ACC	Alaskan Coastal Current
AD	Arctic Dipole
AIDJEX	Arctic Ice Dynamics Joint Experiment
AMAP	Arctic Monitoring and Assessment Programme
AMSA	Arctic Marine Shipping Assessment
ANSR	Administration of the Northern Sea Route
ANWR	Arctic National Wildlife Refuge
AO	Arctic Oscillation
AOR	Area of Responsibility
AR4	Fourth Assessment Report
ASC	Alaskan Stream Current
ASF	Alaska SAR Facility
ASL	Arctic Submarine Laboratory
AVHRR	Advanced Very High Resolution Radiometer
AWPPA	Arctic Waters Pollution Prevention Act
BIC	Bear Island Current
BP	British Petroleum
BSC	Bering Slope Current
C4ISR	Command, Control, Communications, Computers, Intelligence, Surveillance, and Reconnaissance
CAA	Canadian Arctic Archipelago
CANSR	Chief Administration of the Northern Sea Route
CBA	Capabilities Based Assessment
CCDR	Combatant Commander
CCSM	Community Climate System Model
CICE	Community Ice CodE
CH_4	Methane
CISM	Community Ice Sheet Model
CMIP	Coupled Model Intercomparison Project
CNMOC	Commander, Naval Meteorology and Oceanography Command
CO_2	Carbon Dioxide
CPC	Climate Prediction Center
CRREL	Cold Regions Research and Engineering Laboratory

CSA	Canadian Space Agency
CTD	Conductivity/Temperature/Depth
DA	Arctic Dipole Anomaly
DEW	Distant Early Warning
DoD	Department of Defense
DR	Disaster Response
DRI	Departmental Research Initiative
EEZ	Exclusive Economic Zones
EGC	East Greenland Current
EOF	Empirical Orthogonal Function
ESC	East Spitsbergen Current
ESRL	Earth System Research Laboratory
EVP	Elastic-Viscous Plastic
FWC	FreshWater Content
FYI	First Year Ice
GCM	Global Climate Model
GESM	Global Earth System Model
GHG	Greenhouse Gas
GIN	Greenland, Iceland and Norway
GIS	Greenland Ice Sheet
GOOS	Global Ocean Observing System
GPS	Global Positioning System
HA	Humanitarian Aid
HF	High-Frequency
HSPD	Homeland Security Presidential Directive
IABP	International Arctic Buoy Programme
ICESat	Ice, Cloud, and land Elevation Satellite
ICEX	Ice Exercises
IBCAO	International Bathymetric Chart of the Arctic Ocean
IMB	Ice Mass Balance Buoy
IPCC	Intergovernmental Panel on Climate Change
ITP	Ice-Tethered Profile
LANL	Los Alamos National Laboratory
LIDAR	Light Detection and Ranging
LIM	Lagrangian Ice Motion
LKF	Linear Kinematic Feature
MEaSURE	Making Earth Science data records for the Use in Research Environments

METOC	Meteorology and Oceanography
MIZ	Marginal Ice Zone
MYI	Multi-Year Ice
N_2O	Nitrous Oxide
NADW	North Atlantic Deep Water
NAO	North Atlantic Oscillation
NAME	NPS Arctic Modeling Effort
NASA	National Aeronautics and Space Administration
NCAR	National Center for Atmospheric Research
NCC	North Cape Current
NCEP	National Center for Environmental Prediction
NEP	Northeast Passage
NIC	Naval Ice Center
NOAA	National Oceanic and Atmospheric Administration
NORAD	North American Aerospace Defense Command
NPS	Naval Postgraduate School
NSIDC	National Snow and Ice Data Center
NSPD	National Security Presidential Directive
NSR	Northern Sea Route
NSTM	Near-Surface Temperature Maximum
NWP	Northwest Passage
NWS	North Warning System
OBL	Ocean Boundary Layer
ON	October-November
ONR	Office of Naval Research
OTSR	Optimum Track Ship-Routing
PC	Principal Component
PIZ	Perennial Ice Zone
PNA	Pacific/North American Index
POP	Parallel Ocean Program
PSW	Pacific Summer Water
PWW	Pacific Winter Water
QDR	Quadrennial Defense Review
RASM	Regional Arctic System Model
RCP	Representative Concentration Pathway
RGPS	RADARSAT Geophysical Processor System
rWML	remnant Winter Mixed Layer

SAM	Science Accommodation Missions
SAR	Synthetic Aperture Radar
SAT	Surface Air Temperature
SCE	Snow Cover Extent
SCICEX	Science Ice Exercise
SHEBA	Surface HEat Budget of the Arctic Ocean
SIZ	Seasonal Ice Zone
SLP	Sea Level Pressure
SMMR	Scanning Multichannel Microwave Radiometer
SOLAS	Safety Of Life At Sea.
SRES	Special Report on Emissions Scenario
SSM/I	Special Sensor Microwave/Imager
TAPS	Trans-Alaska Pipeline System
TDS	Transpolar Drift Stream
TFCC	Task Force Climate Change
UCP	Unified Command Plan
ULS	Upward Looking Sonar
UNCLOS	United Nations Convention on the Law of the Sea
UNEP	United Nations Environment Programme
USCG	United States Coast Guard
USEUCOM	U.S. European Command
USGS	United States Geological Survey
USMC	United States Marine Corps
USN	United States Navy
USNORTHCOM	U.S. Northern Command
VIC	Variable Infiltration Capacity model
VP	Viscous-Plastic
WCRP	World Climate Research Programme
WHOI	Woods Hole Oceanographic Institute
WMO	World Meteorological Organization
WRF	Weather Research and Forecasting model
WSC	West Spitsbergen Current
WWII	World War II

ACKNOWLEDGMENTS

THIS PAGE INTENTIONALLY LEFT BLANK

I.   INTRODUCTION

A.   BACKGROUND

The mean surface temperatures of the Earth's atmosphere and ocean are increasing, mean annual snow and ice mass are decreasing through melt, and mean global sea level is rising (IPCC 2007). An observed increase in global average temperatures in recent decades is likely linked to the observed increase in anthropogenic greenhouse gas (GHG) concentrations (IPCC 2007). Ice cores, spanning many thousands of years, have indicated that global atmospheric concentrations of carbon dioxide (CO_2), methane (CH_4), and nitrous oxide (N_2O) have increased as a result of human activities, since 1750, and now far exceed pre-industrial values (IPCC 2007). Measurements at the Mauna Loa Observatory, Hawaii have documented a steady increase in atmospheric CO_2 concentration from approximately 315 ppm in 1958 to approximately 394 ppm in 2012. CO_2 annual mean growth rates have ranged between 0.28–2.93 ppm/year from 1958–2011 (ESRL 2012).
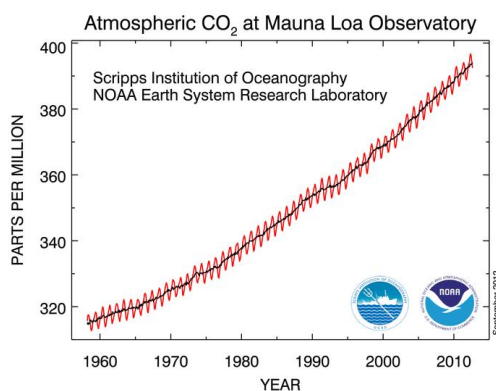
Figure 1.   Monthly mean atmospheric CO_2 at Mauna Loa Observatory, Hawaii (From ESRL 2012)

Enhanced GHG concentrations increase the downward longwave radiation to the Earth's surface. The Stefan-Boltzmann law requires that surface temperatures increase so that the upward longwave radiation can rebalance in response to the increased amount of solar radiation incident at Earth's surface. Global GHG emissions due to human activities

1

have grown since pre-industrial times, with an increase of 70% between 1970 and 2004 (IPCC 2007). Figure 2 shows a noticeable increase in temperature and sea level, while Northern Hemisphere snow cover decreased over the same time span. Large-scale increases in upper-ocean temperatures are evident in observational data and have a consistent positive coherence of an anthropogenic fingerprint (Gleckler et al. 2012).
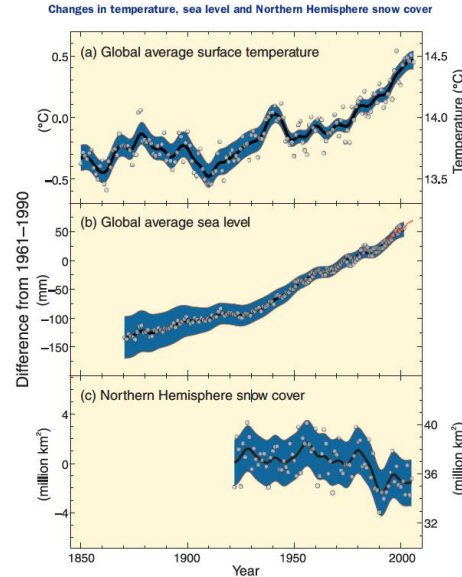
Observed changes in (a) global average surface temperature; (b) global average sea level from tide gauge (blue) and satellite (red) data and (c) Northern Hemisphere snow cover for March-April. All differences are relative to corresponding averages for the period 1961–1990. Smoothed curves represent decadal averaged values while circle show yearly values. The shaded areas are the uncertainty intervals estimated from a comprehensive analysis of known uncertainties (a and b) and from the time series (c).

Figure 2.   Time series of global average surface temperature (top), global average sea level (middle) and Northern Hemisphere snow cover for March-April (bottom) (From IPCC 2007).

While surface temperature increases are widespread across the globe, observations have indicated that this increase is greatest at higher latitudes. Average Arctic temperatures have increased at almost twice the global average rate in the past 100 years (IPCC 2007). This trend has been largely attributed to changes in the last 50 years, where surface air temperature increased significantly more than in previous decades (Overland et al. 2004). This disproportionate surface warming that has occurred in the Arctic relative to the global mean surface temperature is often referred to as polar amplification (e.g., Polyakov et al. 2002; Alexeev et al. 2009), partly resulting from a

2

positive feedback loop unique to ice covered regions (Serreze et al. 2009). This positive snow/ice albedo feedback loop can result from an increase in surface air temperature, leading to a reduction in snow and ice cover through melting. In turn, this reduces surface short wave reflectivity (albedo), hence increasing the absorption of solar radiation at the surface and further reduction of snow and ice cover, hence also albedo, to close the feedback loop. This feedback is most vivid in cryospheric regions poleward of the climatic seasonal or annual 0°C isotherms, since variability of snow, ice and permafrost distribution in these areas is most susceptible to changes in the surface heat budget.

For the Arctic Ocean, this process is known as the positive ice/ocean albedo feedback. As the climate warms, the length and intensity of the melt season is increased, leading to less sea ice surviving through summer's end. The increased area of open water results in summertime absorption of solar radiation and large increases in the amount of sensible heat content in the upper ocean (Serreze et al. 2009). The open ocean surface has a much lower albedo (~0.07) than sea ice or snow-covered ice (0.65 to 0.85) and can absorb larger amounts of solar energy (Perovich et al. 2002). The additional oceanic heat delays the formation of new ice in the fall and winter, promoting enhanced upward heat fluxes into the atmosphere, which are maintained in the lower troposphere by strong low-level stability (Serreze et al. 2009). Larger open ocean surface area and heat content of the upper ocean not only further melt sea ice, but also alter oceanic and atmospheric circulation patterns and release more water vapor into the lower atmosphere via heat removal from the mixed layer before freezing in the fall (Murnane 2012). This amplifies the impact of air temperature increases as water vapor causes a regional greenhouse effect to the lower atmosphere (Langen and Alexeev 2007). The positive ice/ocean feedback helps perpetuate warming in the Arctic region and with persistence, could lead to a new seasonal sea ice regime.

This mechanism, along with potentially many others, has led to the rapid decline of Arctic sea ice. Sea ice can be seen as a keystone indicator of GHG induced climate change. Comparisons of observed variations in Arctic sea ice extent with atmospheric CO_2 levels indicate that in recent decades the rate of sea ice decrease mirrors the increase in CO_2 (Johannessen 2008). Wang and Overland (2009) analyzed the sea ice extent

decline from 1950–2100 using six global climate models (GCMs). Figure 3 depicts their results. The blue and magenta lines indicate sea ice extent from separate ensemble members under anthropogenic forcing while the grey lines represent sea ice extent from the same ensemble members without the anthropogenic forcing. The red line represents observations. The results are evident that without the anthropogenic forcing there is no significant negative trend in sea ice extent thus, the observed changes in Arctic sea ice are most likely a result of warming from increases in the levels of GHGs. It should be noted that most all GCMs demonstrate this result without anthropogenic forcing.
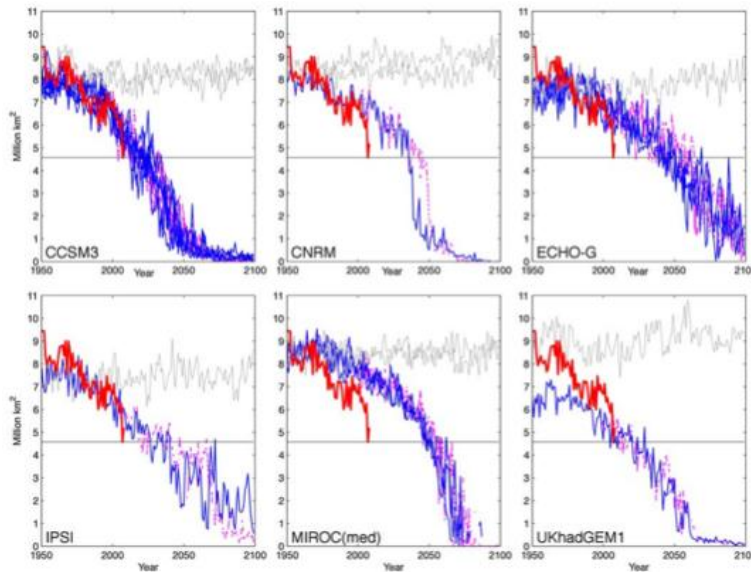
September sea ice extent as projected by the six models that simulated the mean minimum and seasonality with less than 20% error of the observations. The colored thin line represents each ensemble member from the same model under A1B (blue solid) and A2 (magenta dashed) emission scenarios, and the thick red line is based on HadISST analysis. Grey lines in each panel indicate the time series from the control runs (without anthropogenic forcing) of the same model in any given 150 years period. The horizontal black line shows the ice extent at the 4.6 million km^2 value, which is the minimum sea ice extent reached in September 2007 according to HadISST analysis. All six models show rapid decline in the ice extent and reach ice-free summer (<1.0 million km^2) before the end of the 21st century

Figure 3.   September sea ice extent projected by six GCMs. Includes simulation results, observational comparison, and simulation without anthropogenic forcing (From Wang and Overland 2009).

Arctic sea ice extent has long been the benchmark measurement in describing sea ice coverage and is defined as the total area of ocean covered with at least 15% ice concentration. In 2007, the National Snow and Ice Data Center (NSIDC) reported that there had been a notable decrease in Artic sea ice extent since the mid-1990s, culminating

in a record minimum in September 2007 (NSIDC 2007). This record was the lowest extent seen since the beginning of the satellite record in 1979 and was 39% below the long-term average from 1979 to 2000 at approximately 4.28 million km2. Subsequent years of extremely low September sea ice extent minimum levels continued after 2007, but none broke the record until September 16, 2012, when observed sea ice extent shattered the minimum area set in 2007, dipping to approximately 3.41 million square kilometers. Figure 4 shows a comparison of the record low years in September sea ice extent with the long-term mean from 1979–2000, courtesy of NSIDC.
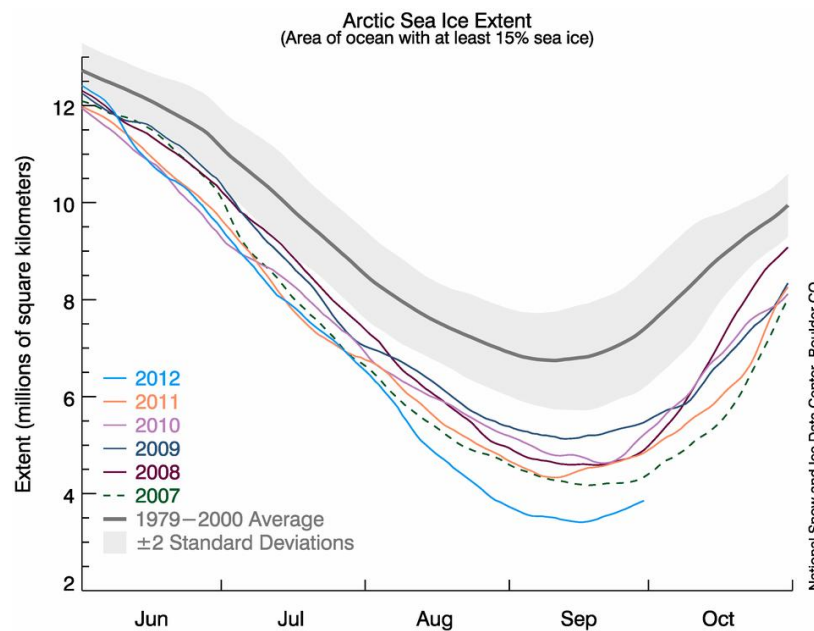
Figure 4.   Arctic sea ice extent through September 2012 (From NSIDC 2012)

The recent increase in the mean temperature of Earth's terrestrial and marine surfaces has affected more than just the Arctic sea ice. System-wide transitions are being observed, including increased precipitation in the high north, changes in arctic storm tracks, and an increased number of extreme weather events. Greenland Ice Sheet melt has also accelerated (GIS) (Shepard et al. 2012). Complete melt of the GIS could cause up to a 6m rise in mean sea level, which is likely to cause human populations to retreat inland and away from low lying coastal areas. Additionally, warming temperatures and decreasing surface albedo is causing a northward march of certain shrubs and tree

species, while decreasing snow cover has led to northern hemisphere permafrost warming (Derksen and Brown 2012). Vast stores of carbon previously frozen into permafrost have the potential to accelerate warming even more (Overpeck et al. 2005), particularly by the release of methane, which is a significantly more potent GHG than carbon dioxide. Additionally, coastal erosion will increase as ice retreats from shore and winds with longer fetch over open water generate more ocean waves and increase energy dissipation on coasts. Considering the reduced snow cover extent (SCE), warming permafrost, reduction in Arctic sea ice extent, as well as an increased mass loss from glaciers and ice sheets (Derksen et al. 2012), there is increasing evidence of an accelerating cryospheric response to climate change (Derksen and Brown 2012).

Sea ice melt has consequences for not only ecosystems, but natural resource development, shipping and defense practices as well. The United States Geological Survey (USGS) estimates that the Arctic holds as much as one quarter of the world's remaining undiscovered oil and gas deposits (Borgerson 2008). The largest deposits are thought to be near Russia, although the Shell Company holds millions of dollars' worth of leases in the Chukchi and Beaufort Seas. Additionally, the Chevron Corporation has won drilling bids in the Beaufort Sea that were set to commence in 2012, but were halted due to late local ice retreat and damages to safety equipment. It is estimated that by 2015 oil production in the Arctic region will account for 40% of the world's total, and it seems ironic that declining sea ice is likely to produce more of the commodities that precipitated its melt in the first place through the consumption of fossil fuels (Borgerson 2008).

Under international law, no country currently owns the North Pole or the region of the Arctic Ocean surrounding it. But, the five countries surrounding the Arctic Ocean (United States, Canada, Russia, Norway, and Denmark (via Greenland)) are limited to an exclusive economic zone (EEZ) of 200 nautical miles adjacent to their coasts. Upon ratification of the United Nations Convention on the Law of the Sea (UNCLOS), any country has a ten-year period to make claims to an extended continental shelf, which, if validated, gives it exclusive rights to resources on or below the seabed of the extended shelf area (UNCLOS 2011). The convention was ratified by Norway in 1996, Russia in 1997, Canada in 2003, and Denmark in 2004. All of which have launched projects to

provide a scientific basis for seabed claims on extended continental shelves beyond their EEZs. Currently, the U.S. has signed, but not yet ratified the UNCLOS treaty.

The 2007 sea ice extent minimum also resulted in increased speculation that the Northwest Passage (NWP), which extends along the northern coast of North America through the Canadian Arctic Archipelago (CAA), could soon be open to shipping and transit. This event precipitated a change in the widespread perception of the Arctic as a non-navigable expanse, helped by Russia signaling an intent to regularly exploit the Northern Sea Route (NSR) (Kramer and Reykin, 2009). These two shipping routes offer nearly 25% and 35–60% savings in distance, respectively, from alternate routes through the Panama or Suez Canal (Titley and St. John 2010). However, these newly opened sea routes present security concerns, including their potential as avenues for smuggling and terrorist activities. Increased shipping traffic in these poorly surveyed waters has also raised questions about safety of life at sea (SOLAS) and environmental issues, such as pollution from oil spills.

B.   INTENT OF STUDY

Sea ice extent has continued to reach extreme summer minimums since 2007, and the observed decrease in extent has been faster than predicted by most GCMs (Stroeve et al. 2007). This coupled with the concern that multiyear ice has been and continues to be exported at an alarming rate from the Arctic Ocean (Kwok 2007), has caused a shift in focus away from areal ice extent and towards modeling and observing three dimensional changes, which includes ice thickness and volume (Haynes 2010). A number of studies suggest that sea ice thickness and volume may be decreasing at an even faster rate than ice extent (e.g., Maslowski et al. 2008; Rothrock et al. 2008; Kwok and Rothrock 2009; Kwok et al. 2009; Maslowski et al. 2012). This would indicate that the atmospheric forcing on the climate system is insufficient to account for the observed loss and is not the only mechanism at play (Francis et al. 2005; Maslowski et al. 2007). Therefore, the contribution of oceanic forcing on sea ice should be more closely analyzed, particularly in wintertime when the ocean holds a large portion of the overall heat budget in the Arctic.

There are two types of oceanic influences that impact the state of sea ice within the Arctic: thermodynamic and dynamic forcing. Thermodynamic processes involve changes in radiative fluxes and oceanic heat transport, while dynamic processes involve changes in sea ice motion and circulation in response to oceanic currents as well as atmospheric forcing (Serreze et al. 2007). Dynamical forcing has been shown to influence the thickness distribution and mechanical characteristics of sea ice through deformation events (Rothrock and Zhang 2005; Kwok et al. 2008; Rampal et al. 2009). The stratification of water column in the western Arctic acts to trap warmer water beneath the surface mixed layer beyond summer, leaving the potential for dynamical processes to break this stratification and result in thermodynamic interaction within the upper ocean. Sea ice deformation and oceanic forcing therefore have to be more closely analyzed to determine their role in the recent decline of sea ice extent and thickness.

Due to a dearth of polar observations, numerical modeling remains a key method for understanding air, ocean, and sea ice interactions. The coarse resolution and limited parameterizations of many GCMs reduces their skill in representing processes critical to the Arctic's changing climate. Fully coupled GCMs are now commonplace, whereby sea ice, ocean, atmosphere and land models exchange heat, momentum and mass fluxes so as to evolve their states concomitantly to model Earth's climate as a whole. However, GCMs are resolution-restricted by available computing power. For that reason, fully coupled, high resolution regional models of the Arctic are being developed to better understand fine-scale processes, and act as a test beds for future high-fidelity global models. These regional models can, arguably, better represent the sea ice thickness distribution in the Arctic and the survivability of sea ice in a given year. More sophisticated models may have the ability to accurately represent these deformation events and thus better represent the observed rate of decline of sea ice (e.g., Kwok et al. 2008).

C. OVERVIEW

An accurate understanding of the atmospheric, oceanic, and sea ice physics involved and contributing to the decline of Arctic sea ice is paramount in the ability to

model and predict a new seasonally ice free regime in the Arctic. Specifically, understanding the relative contribution of dynamic processes to the sea ice state may help to improve the current understanding of the variable rate of sea ice decline. This study provides analyses of available to-date RASM results to advance the understanding of critical processes and feedbacks concerning the oceanic forcing and rate of decline of Arctic sea ice. In particular, the influence of sea ice deformation events on the upper ocean is investigated. Additionally, the spatial and temporal characterization of these events is analyzed to compare with previous observational analysis in order to understand the ability to resolve deformation processes within the model domain and the overall impact of these events on the ice pack.

This thesis is organized into the following chapters: Chapter II provides a literature review of the current research pertaining to Arctic sea ice, including a discussion of influential atmospheric and oceanic processes, sea ice variability, and sea ice modeling; Chapter III discusses the relevance of this research to the U.S. Navy including history, current strategy, international interests, and current capabilities; Chapter IV describes the model and methodology used to conduct this research; Chapter V presents the numerical model results and analysis discussion; Chapter VI contains conclusions and makes recommendations for future research.

THIS PAGE INTENTIONALLY LEFT BLANK

II. LITERATURE REVIEW OF RESEARCH PERTAINING TO ARCTIC SEA ICE

The Arctic system is a complex adaptive environment that is a function of many dynamic constituents including the atmosphere, ocean, terrestrial components, as well as ecosystem, biogeochemistry and cryospheric components within each of these constituents. Each of these has an impact on arctic sea ice state (Roberts et al. 2010).

A. ATMOSPHERIC PROCESSES

Atmospheric forcing has perhaps the largest impact on sea ice formation, drift, deformation and melt (e.g., Wadhams 2000). Much of the research into sea ice variability in the Arctic has concentrated on the atmospheric contribution to ice melt, citing the well-known ice albedo feedback mechanism as the primary driver for sea ice decline (e.g., Francis and Hunter 2006; Francis and Hunter 2007; Perovich et al. 2008). Dramatic changes in the Arctic climate have been observed over the last 30 years. These changes include warming trends in the surface air temperature (SAT) over the Arctic Ocean, during the winter and spring, with values as high as 2ºC per decade in the eastern Arctic spring (Rigor et al. 2000) as well as decreases in sea level pressure (SLP) over the central Arctic Ocean between 1979–85 and 1986–1994 (Walsh et al. 1996).

1. Arctic Oscillation (AO)

Many of these changes have been linked (Rigor et al. 2002) to changes and variability in the Arctic Oscillation (AO), whose index is defined as the leading principal component (PC) or leading empirical orthogonal function (EOF) of the wintertime Northern Hemisphere SLP (Thompson and Wallace 1998). The AO can be characterized as an exchange of atmospheric mass between the Arctic Ocean and the surrounding zonal ring centered at ~45°N (Rigor et al. 2002). The positive phase of the AO is exhibited with a relatively low SLP over the polar region and high pressure at mid-latitudes while the negative phase is when the above pattern is weakened or reversed, with relatively high SLP over the polar region and low pressure at mid-latitudes (Figure 5). In the positive phase, higher pressure at mid-latitudes drives the storm track farther north into the

northern Europe. In the positive phase, frigid winter air does not extend as far into the middle of North America as it does during the negative phase of the oscillation.
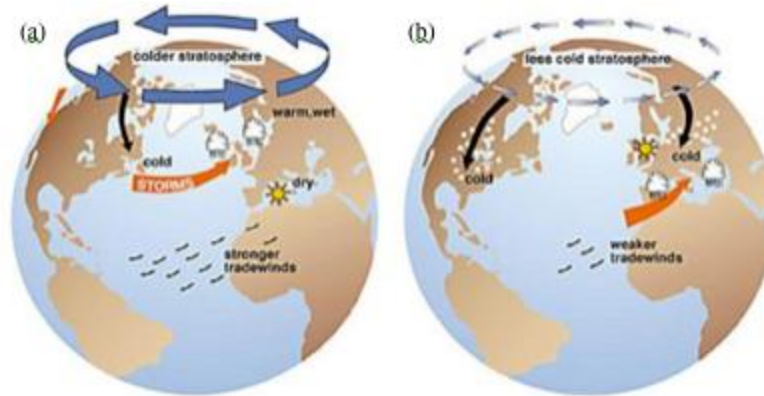
Figure 5.   (a) Positive phase and (b) negative phase of the Arctic Oscillation induced atmospheric patterns (From NSIDC courtesy of J. Wallace, University of Washington 2012).

2.   North Atlantic Oscillation

The North Atlantic Oscillation (NAO) is a similar index to the AO, but it describes the pressure pattern in the North Atlantic only. It is defined as the covariability between the SLP strength of the Icelandic low and Azores high (Hurrell 1995). During a positive NAO phase, a strong Icelandic low and a strong Azores high creates an intense pressure gradient to amplify the westerly jet and direct storm tracks to the north similar to a positive AO event (Maslanik et al. 1996; McPhee et al. 1998). Conversely, during a negative NAO phase the Icelandic low and Azores high are weakened, which in turn weakens the pressure gradient between the systems and results in weaker westerlies directed more into the Mediterranean region. Ultimately, changes in storm tracks can either increase (+NAO) or decrease (-NAO) the energy and atmospheric mass imported to the Arctic, which determines the overall strength of the AO (Hurrell 1995). In addition, the variability of storm track direction has a large influence on the amount of heat that is horizontally advected into the eastern Arctic. Storms bring heat both in the atmosphere and in the ocean as well as increase atmospheric forcing on sea ice, which can result in melting and deformations of the ice.

3.   AO/NAO Regional Influences

Besides the mid-latitude storm track adjustment and the atmospheric mass transfer into and out of the Arctic, the AO/NAO indices also impact the prevailing wind pattern within the Arctic region. During a negative phase of the AO, high pressure builds an anticyclonic (clockwise) zonal flow in the western Arctic known as the Beaufort high. Geostrophic balance dictates that convergence will be prevalent in the system as the Coriolis 'force' is directed inward or to the right of the mean flow in the northern hemisphere. This causes sea ice to converge as well, resulting in ridging and increased thickness. Under these conditions sea ice is thought to remain in the Arctic basin longer and thus there is a buildup of older thicker ice (Proshutinsky and Johnson 1997). During a positive phase of the AO, this atmospheric pattern is weakened or reversed, which decreases the convergence due to geostrophy or even results in divergence from the system directing the mean flow out of the Arctic.

The AO entered a strongly positive phase, enhancing sea ice export through Fram Strait, most notably thick multiyear ice (Rigor and Wallace 2004), from the mid-1980s through the mid-1990s. Since the mid-1990s to early 2000s; however, the AO has shifted back to a largely neutral or negative phase, while a negative sea ice extent trend has persisted and accelerated during the last decade (Maslanik et al. 2007). Many expected that with the shift of the AO back to a negative or neutral phase, the rapid decline in sea ice would either come to a halt or at the very least decrease from the current rate (Maslanik et al. 2007), but that did not happen. Lindsay and Zhang (2005) even questioned if the Arctic had reached a tipping point resulting in a new regime of environmental forcing that was influencing the observed sea ice decline, but the possibility of tipping points in Arctic sea ice cover has been recently discounted (Eisenman and Wettlaufer 2009).

4.   Arctic Dipole Anomaly (DA) or Arctic Dipole (AD)

The positive and negative phases of the AO/NAO help determine the direction and magnitude of the mean wind circulation in the Arctic as the AO accounts for 59–63% of the SLP variance in the Arctic. Still, the second leading mode of the wintertime

Northern Hemisphere SLP has been found to be important as well (Wu et al. 2006). This pattern known as the Arctic Dipole Anomaly (DA), or Arctic Dipole (AD), is determined by the SLP pattern. The center of the SLP system is generally located near the Laptev Sea (near Siberia) or the Greenland Sea (Watanabe et al. 2006; Overland and Wang 2010). The DA also varies between positive and negative phases in a dipole pattern and results in a meridional flow accounting for 14–19% of the SLP variance in the Arctic. A positive phase of the DA is associated with a negative SLP anomaly on the North American side of the Arctic (Overland and Wang 2010). A positive SLP anomaly in the western Arctic with the negative SLP anomaly over the Greenland Sea (negative DA) generates a meridional flow directed across Arctic Ocean and can help explain circulation patterns when they are not entirely in synch with the AO. DA increases ice flow along the Transpolar Drift Stream (TDS) due to the meridional nature of its circulation pattern (Wu et al. 2006).
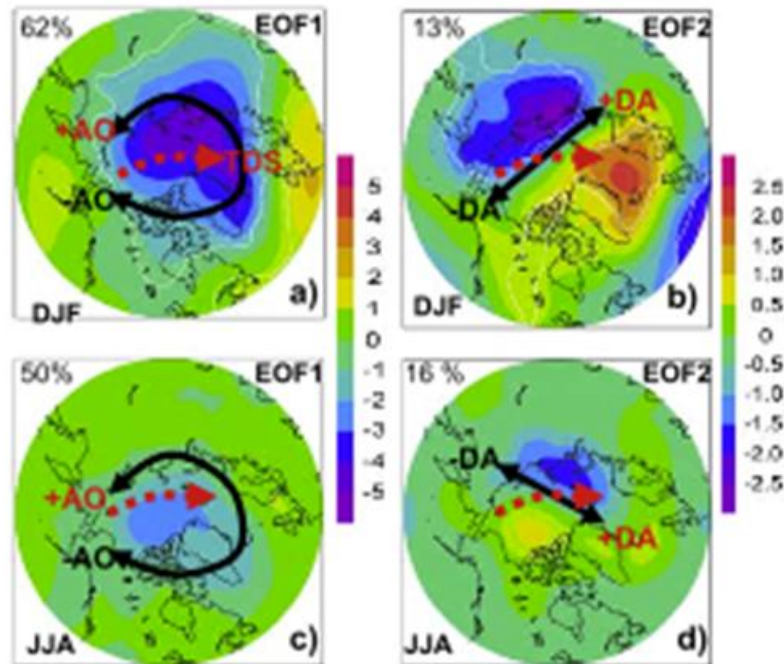
Regression maps of the first two leading modes to the (a and b) winter and (c and d) summer mean Northern Hemisphere SLP field using the NCEP Reanalysis dataset from 1948 to 2008. Contour intervals are 0.5 hPa (see color bars). The black arrows in (a) and (c) indicate the cyclonic (anticyclonic) wind anomaly during the +AO (-AO). In (b) and (d), the black arrows indicate wind anomalies between the western and eastern Arctic during +DA and –DA phases that accelerate or decelerate the TDS (in red-dashed arrows), respectively.

Figure 6.   Comparison of the first leading mode (AO) and the second leading mode (DA) for winter and summer months (From Wang et al. 2009).

Wang et al. (2009) found that regardless of the sign of the AO, sea ice export was greatly increased during years with positive phase of the DA. Conversely, during years of negative DA, sea ice tends to be withheld in the basin as the Beaufort gyre is strengthened and the TDS flow is weakened, resulting in the convergence and accumulation of sea ice and freshwater in the gyre (Wu et al. 2006). A negative DA pattern retains more ice back in the Arctic, leaving more open water in the North Atlantic, which may increase the amount of heat storage in the ocean and eventually impact the atmospheric circulation through the release of this excess heat in fall, preconditioning ice for more retreat in following seasons (Overland and Wang 2010).

B.   OCEANIC PROCESSES

The Arctic Ocean is a complex environment as well (Figure 8) and it is a function of many dynamic constituents, including variable heat, salinity and freshwater fluxes, changing stratification layers and depths, mesoscale eddies and currents, as well as small-scale bathymetric steering (e.g., canyons, troughs, submarine ridges) and shelf-basin interactions. In comparison to the atmosphere, oceanic influences have perhaps been largely undervalued and commonly overlooked in regional studies. Atmospheric events, such as storms, affect sea ice over relatively short timescales of hours to days. Conversely, the ocean has a much longer 'memory' than the atmosphere, and some oceanic events persist for weeks to years, potentially affecting sea ice and atmospheric variability over that time. The heat capacity of the ocean lends itself to this fact. Deser and Teng (2008) used satellite derived sea ice concentration data to determine the role of atmospheric forcing on sea ice and found that the sea ice decline can not be explained by a trend in the overlying atmospheric circulation alone, and suggested that oceanic forcing must play a vital role, especially in winter. Model results from Stroeve and Maslowski (2007) suggest that atmospheric forcing accounts for less than half of the variance in Arctic sea ice cover while Tseng (2010) made similar findings using a partial covariance analysis.

In models with low spatial resolution, Arctic Ocean circulation and ocean dynamics are difficult to resolve, particularly for GCMs with grid cells at ≥100km. This

commonly yields conclusions suggesting that oceanic forcing is fairly negligible on the grand scale, when in fact upon a closer analysis, this could not be further from the truth. Oceanic forcing provides critical dynamics and processes of relevance to large-scale Arctic oceanography and climate, which must be understood in order to accurately assess changing climate conditions and improve future predictions.
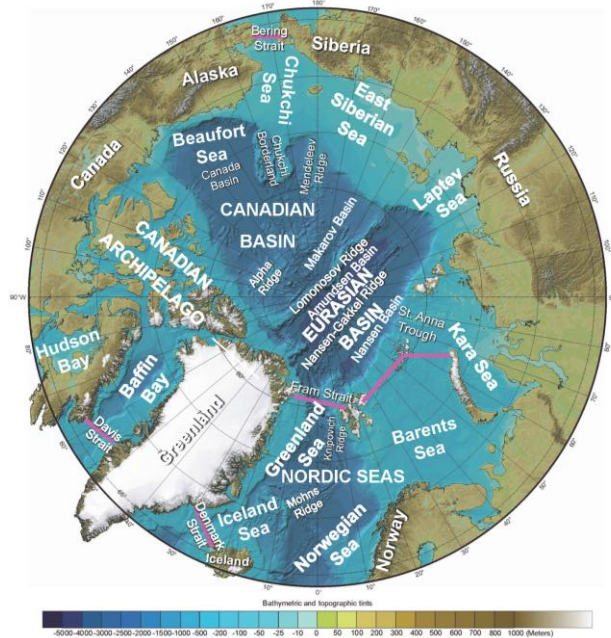
Figure 7.   The International Bathymetric Chart of the Arctic Ocean (IBCAO) with names of major oceanographic regions and surrounding landmasses (After IBCAO 2012)

1.   Mean Circulation

Currents and exchanges, in the Arctic Ocean, are most commonly described by the conservation of potential vorticity (Nøst and Isachsen 2003), which is influenced by bathymetric effects as well as other buoyancy driven processes. This indicates that coastal margins and shelf-basin exchanges are critical to the overall circulation in the Arctic region. However, due to the unique topography and bathymetry in the Arctic region (Figure 7), not all mesoscale exchanges are well known or represented. Figure 7 shows the International Bathymetric Chart of the Arctic Ocean (IBCAO) with labels indicating distinct bathymetric features of importance and dynamical consequence in the

Arctic. Figure 8 shows a mean, large-scale, schematic representation of the upper/surface ocean currents in the Arctic region. It is important to note the red and blue currents indicate warm or cold water being advected into and out of the region while the square boxes represent areas of submerging water.

Figure 8.   Surface currents in the Arctic region. Square boxes indicate that the denser inflowing (Atlantic and Pacific) waters are submerging under the Polar Surface Water (From the Arctic Monitoring and Assessment Programme [AMAP] Assessment Report [AAR] 1998).

2.   Atlantic Water

Due to the relatively limited amount of heat advected into the Arctic Ocean, the transport and distribution of heat within the region becomes critically important. There are two primary oceanic pathways for heat to be advected into the Arctic: the northward flow of Atlantic water through Fram Strait and Barents Sea, and the northward flow of Pacific water through Bering Strait. Looking at the Atlantic side first, the northward flow represents the advection of oceanic heat into the Eastern Arctic. The West Spitsbergen Current (WSC) carries oceanic heat north through the east side of Fram Strait, while the East Greenland Current (EGC) flows south along the west side of the strait. Oceanic heat is also carried to the northeast into Barents Sea via the North Cape Current (NCC), while

the East Spitsbergen Current (ESC) and the Bear Island Current (BIC) flow to the southwest along the southern coast of Spitsbergen. Northward flux estimates through Fram Strait via the WSC from available observations are ~6.8 +/- 0.5 Sv for volume and ~36 +/- 6 TW for heat flux (Beszczynska-Möller et al. 2011). It has also been found that the net volume and heat fluxes across the Barents Sea opening are ~2.0–3.2 Sv and ~29–162 TW (Maslowski et al. 2004; Gammelsrod et al. 2009). Maslowski et al. (2012) estimated that 70–140 TW of heat is lost to the atmosphere over the Barents Sea, which leads to water mass transformation through cooling, mixing and mesoscale eddies as well as to changes in atmospheric circulation.

3.   **Pacific Water**

The inflow of summer Pacific water through Bering Strait is fed upstream by meandering eddies off the Alaskan Stream (AS) and the Bering Slope Current (BSC). On the Bering Sea shelf, the Alaska Coastal Current (ACC) on the east side and the Anadyr Current (AC) on the west side carry water toward Bering Strait. Upon exiting the strait on to the Chukchi Shelf, the flow diverges along their respective coasts. Using model output from the Naval Postgraduate School (NPS) Arctic Modeling Effort (NAME) regional ice-ocean model (at ~9 km horizontal resolution), Clement et al. (2005) found that approximately 0.65 Sv and ~4.17 TW of heat is transported northward through Bering Strait between the ACC and AC. Model runs indicated that the narrow ACC crosses the Chukchi shelf break where a 26 year mean of ~0.68 Sv and ~1.167 TW of heat is transported and potentially trapped below the mixed layer in the Canadian Basin (Maslowski et al., 2012b). The model runs also indicated that while there were occasional years of high heat flux in summer during the first part of the time series (e.g., 1986 and 1989), the summer peaks were all at least 4 TW for the last 7 years (1998–2004).

Maslowski et al. (2008) found that subsurface mesoscale eddies contribute to the communication of water masses on the shelf and in the Canadian Basin, as well as contribute to heat lost to the atmosphere via cooling and mixing. In fact, it is believed that mesoscale anticyclonic eddies, that initiate off the Chukchi Shelf at the Northwind Ridge, may be quite numerous and may help determine the anticyclonic nature of the Beaufort

Gyre circulation more so than previously thought. During wintertime, the heat distribution becomes critically important, thus, accurately understanding where heat comes from and where it is distributed to and stored is essential in understanding the overall heat budget of the Arctic and its effect on sea ice.

Limited observations of the above processes are available due to a lack of observational sampling in the region. Though numerical models help to fill this void by providing valuable insight into the processes, more observations are necessary to compare the actual dynamics and thermodynamics to model simulations. This sort of synthesis is essential to improve models and their future climate projections and forecasts.

4.   The Water Column of the Western Arctic

The western Arctic has seen the most dramatic decline in sea ice throughout the Arctic region. This would indicate that the physics in that region are undergoing the most robust changes in the Arctic and should be more closely examined. Observations indicate warming, in recent years, in the near-surface (upper ~100m) waters of the Canada Basin. The warming is thought to be related to the increased annual absorption of solar radiation, via the positive ice/ocean albedo feedback mechanism, due to the decrease of summer sea ice (Perovich et al. 2007). Summer solar radiation is stored throughout winter due to higher stratification and a shallower winter mixed layer (Toole et al. 2010) associated with the increased accumulation of freshwater (Jackson et al. 2010).

The base of the summertime surface mixed layer is called the summer halocline and is formed when sea ice melt dilutes the surface mixed layer (Jackson et al. 2010). Below the summer halocline is a feature called the near-surface temperature maximum (NSTM), which forms each summer when sufficient solar radiation warms the upper ocean and is trapped by the summer halocline, thereby storing heat from solar radiation (Jackson et al. 2010).   During winter, the NSTM will either disappear if winter mixing erodes the summer halocline or it is trapped year-round below the summer halocline if mixing is constrained (Jackson et al. 2011). The summer halocline is weakened due to storm driven mixing, resulting in heat entrainment from the NSTM upward, thereby

melting the underside of the sea ice in winter (Jackson et al. 2010). The temperature minimum below the NSTM is the remnant of the previous winter's mixed layer (rWML) (Jackson et al. 2010). The second temperature maximum below is maintained by Pacific Summer Water (PSW) and is followed by a second halocline called the winter halocline (Jackson et al. 2011). The temperature minimum below the PSW is Pacific Winter Water (PWW). Finally, the third temperature maximum is Atlantic water that floods the deeper portions of the basin (Jackson et al. 2010). Figure 9 is taken from Jackson et al. (2010) that clearly marks the water masses in temperature and salinity profiles. Also of note is the Brunt-Väisälä frequency profile that indicates the level of stratification at depth.
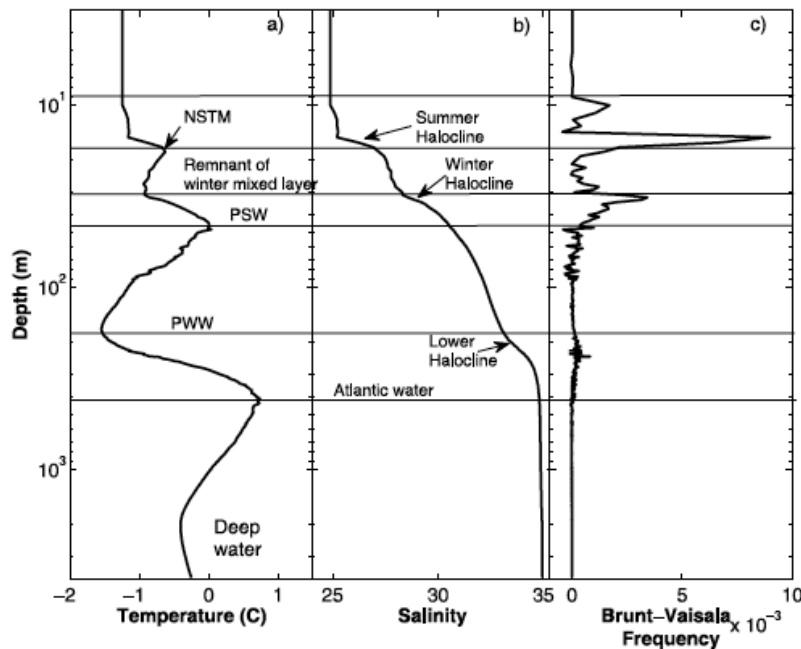
Water mass structure of the Canada Basin as characterized by (a) temperature, (b) salinity, and (c) Brunt-Väisälä frequency profiles. Note the depth axis is log scale. In summer, there are up to three temperature maximums (NSTM, PSW, and Atlantic Water), two temperature minimums (rWML and PWW), and three haloclines (the summer halocline, the winter halocline, and the lower halocline). The strongest stratification is associated with the NSTM. Profiles are from a station located 75°N, 150°W, occupied on 29 August 2006

Figure 9.   Structure of the water column in the Canada Basin (From Jackson et al. 2010)

5.   Oceanic Heat in the Western Arctic

The density gradient between the bottom of the mixed layer and NSTM presents a strong barrier to upward mixing, hence, most of the ocean heat flux in the central basins derives from solar heating through open leads and thin ice during summer, rather than

from turbulent mixing of the heat below (Maykut and McPhee 1995; Perovich and Elder 2002). Shimada et al. (2006) found that atmospheric forcing only partially explains the recent changes in sea ice cover and that an area of anomalous sea ice reduction in the Canada Basin corresponds with an area where warm PSW is observed below the mixed layer. They suggest that the warming of the upper ocean was due to a positive feedback mechanism initiated by delayed sea ice formation in early winter. Additionally, the analysis of surface and bottom melt observations from ice mass balance buoys (IMBs) in the Beaufort Sea show that the transfer of heat from the upper ocean to the bottom of the ice potentially causes a large amount of bottom ablation (Perovich et al. 2008). The record minimum ice extent in 2007 could be attributed to the positive ice-albedo feedback effect causing solar heating of the upper ocean, which is then transferred to the underside of the ice.

Recent observations in the Canada Basin have verified the bottom melting of sea ice associated with warming ocean water (Jackson et al. 2010). Toole et al. (2010) found that Arctic sea ice is most sensitive to changes in ocean mixed layer heat. This potential for heat entrainment would be possible through the winter as the heat from summertime solar radiation is trapped beneath NSTM as well as heat from the PSW is closely beneath that. Access to this "reservoir" of heat could result in delayed ice formation, limited ice growth, and/or even ice melt through the winter, effectively contributing to the sea ice thickness decline. Results from Maslowski et al. (2012) implied that oceanic heat sources may precondition the ice for summer melt and suggest that a large portion of the total variance in sea ice thickness in the region can be attributed to the effects of warm water below ice originating from the Chukchi Shelf and distributed throughout the basin by mesoscale eddies. Haynes et al. (2010) showed that mesoscale eddies may be a significant source of heat via upward entrainment into the mixed layer

Heat exchange between the mixed layer and deeper water will be enhanced due to any physical processes that raise the stratification depth, such as turbulent energy associated with mixing that originates at the ice-ocean interface (McPhee et al. 2005). This study will look at a mechanism that may help entrain heat into the mixed layer

through the shear motion and deformation of sea ice as a result of the observed sea ice thinning, decreasing ice strength and increasing ice drift.

C.   ARCTIC SEA ICE VARIABILITY

The Arctic region is unique from any other region in the world in that it has large shelves and deep basin surrounded by landmasses on almost every side, similar to a large estuary. Additionally, a layer of sea ice acting as a barrier between the ocean and atmosphere has perennially altered the air-ocean interface. With the decline of sea ice in the Arctic, the regional environment has become more and more variable and unstable, with increasingly large uncertainty as to what implications this may bring. Much effort and research has been done to understand why the sea ice melting, how fast it is retreating, and what the ramifications on the short and long-term climate and ecosystems regionally and globally may be.

1.   Sea Ice Extent, Area, and Volume

A common measure of the overall sea ice coverage is known as sea ice extent and can be defined as the total area of ocean covered with at least 15% of ice concentration, where ice concentration is the measure of the fractional amount of ice within a satellite footprint or model grid cell. Another similar measure is ice area, which is the total area of ocean surface actually covered by sea ice. Cryosphere Today (http://arctic.atmos.uiuc.edu/cryosphere/) tracks sea ice by the measurement of area, while the NSIDC (http://nsidc.org/) primarily measures sea ice extent. The preference in reporting can be attributed to the fact that satellites sensors can be prone to errors in summertime when surface melt or melt ponds are commonly accounted for as open water rather than water on top of sea ice. Figure 10 is an example of the measurements of sea ice extent and area in early October 2012.
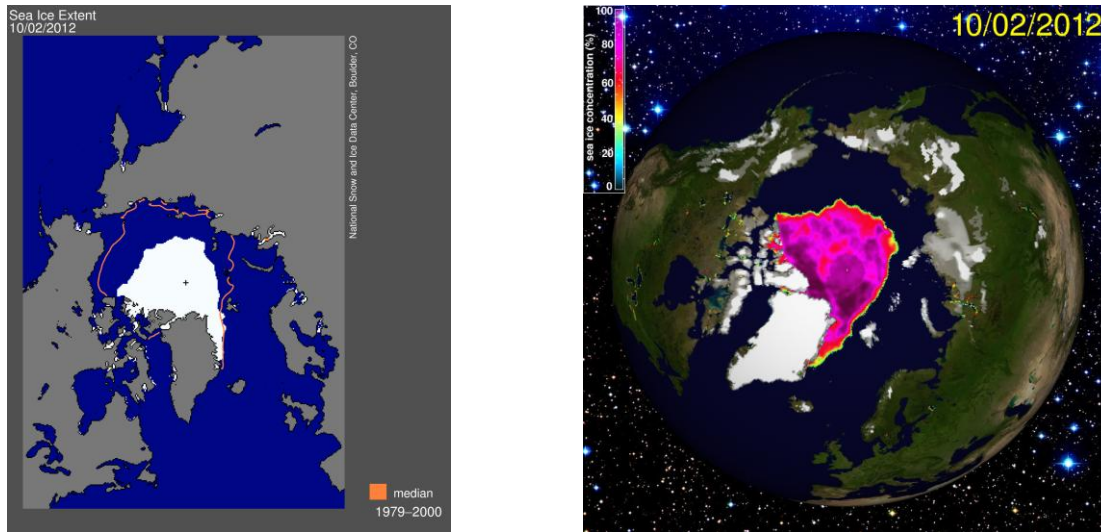
Figure 10.   The image on the left is a map of the sea ice extent on 10/2/2012 from the NSIDC. The image on the right is a map of sea ice area on 10/2/2012 from Cryosphere Today. (From NSIDC 2012, Cyrosphere Today 2012).

The summer Arctic sea ice extent has been in decline over the last three decades. The record September minimum, dating back to the beginning of the satellite climate data record in 1979, was set in 2012 and in 2007 previous to that. The years between 2007 and 2012 were also significantly less than the long term mean, indicating that the rate of decline has been variable and actually increasing as of late. From 1979 to 2001 the rate of decline was -6.5% per decade; from 1979 to 2005 the rate of decline was -8.6% per decade; from 1979 to 2007 the rate of decline was -10.2% per decade; and from 1979 to 2012 the rate of decline was -13.0% per decade (Maslowski et al. 2012; Comiso et al. 2008; NSIDC website). The rate of decline almost doubles with the incremental addition of years from 2001 to 2011.

Figure 11, below, shows the time series of September-mean Arctic sea ice extent. The average Arctic sea ice extent for September 2012 was the lowest in the satellite record, and was 16% lower than the previous low for the month, which occurred in 2007. The six lowest September ice extents over the satellite record have all occurred in the last six years. Compared to the 1979 to 2000 average ice conditions, the September 2012 ice cover represents a 49% reduction in the area of the Arctic Ocean covered by sea ice (NSIDC 2012).

23

Average Monthly Arctic Sea Ice Extent
September 1979 - 2012
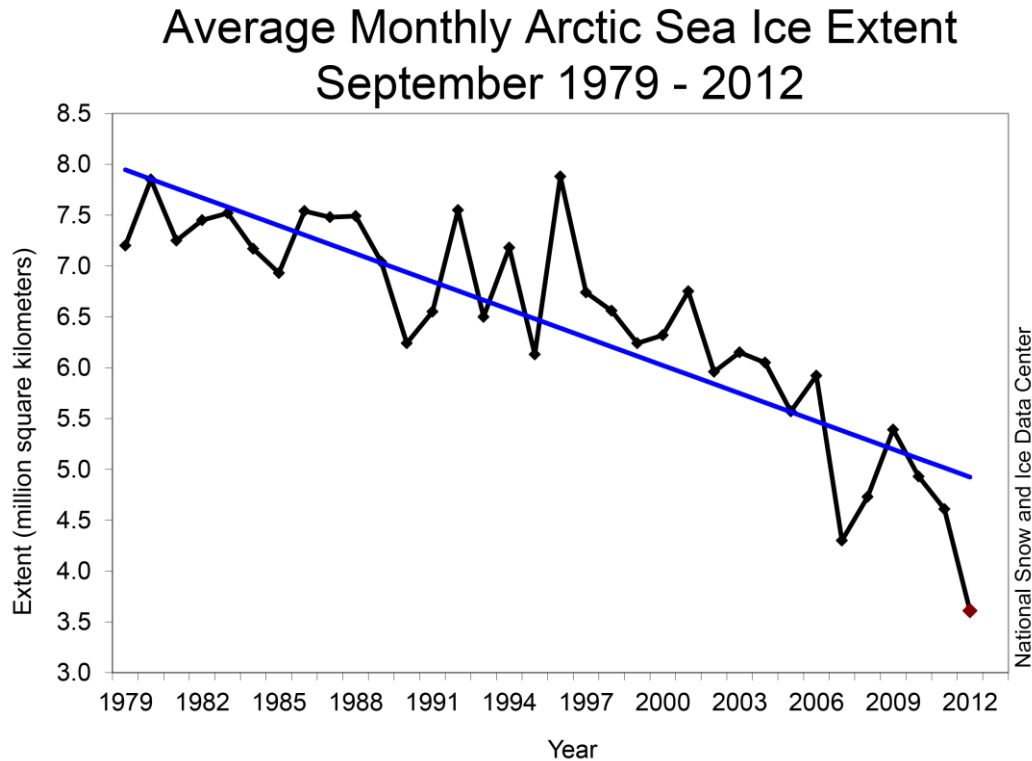
Figure 11. Average monthly Arctic sea ice extent for September (From NSIDC 2012)

Looking at Figure 11, 1997 can be seen as somewhat of a transition point in the rate of decline with the years after 1997 showing an accelerated negative trend. From approximately the mid-1980s through the mid-1990s, the AO index showed good correlation with observations in sea ice extent such that positive phases were associated with years of anomalous sea ice retreat and negative phases were associated with years of sea ice preservation. The AO index time-series shows much less correlation with sea ice extent anomalies beginning in about 1997. A good example of that would be the sea ice response to an extreme negative phase of the Arctic Oscillation during the winter of 2009/2010 (Stroeve et al. 2011). Correlating the DA with the sea ice extent may help explain sea ice behavior in more recent years, but it still begs the question what is driving changes in atmospheric circulation patterns and the rate of sea ice decline?
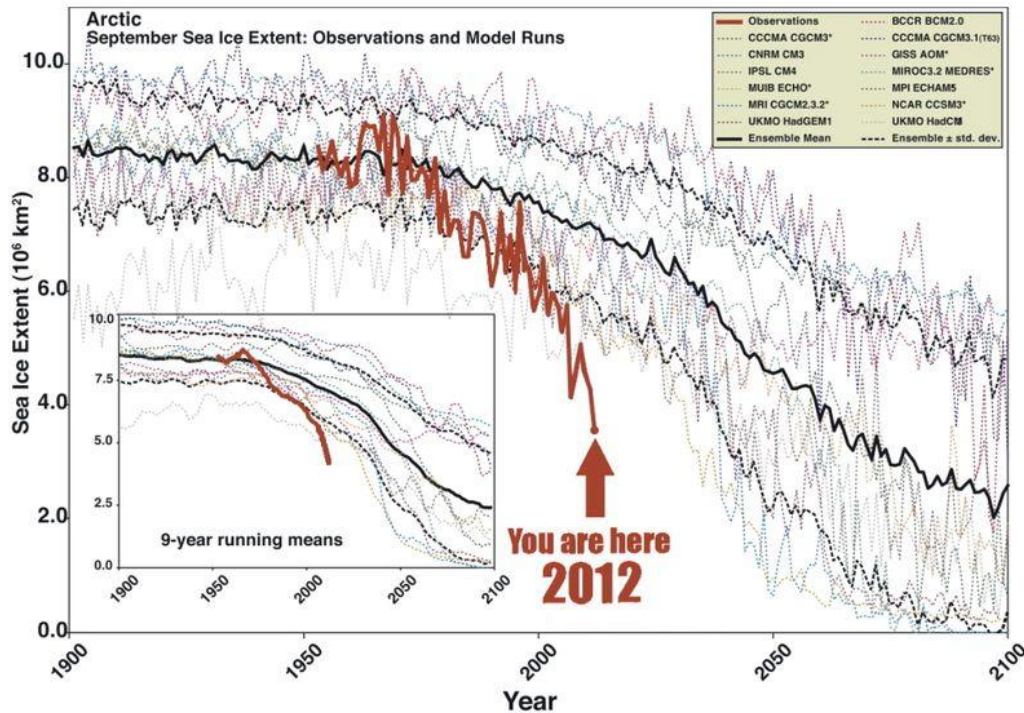
Arctic September sea ice extent (x 106 km^2) from observations (thick red line) and 13 IPCC AR4 climate models, together with the multi-model ensemble mean (solid black line) and standard deviation (dotted black line). Models with more than one ensemble member are indicated with an asterisk. Inset shows 9-year running means.

Figure 12.   Comparison of the September sea ice extent from observations and 13 IPCC AR4 climate models (After Stroeve et al. 2007) Note: the observed values after 2006 were drawn as an addition for the comparison purposes of this thesis and is not exact.

A large amount of research has gone to the development of GCMs to advance simulation of Arctic sea ice behavior and predict its future states. As with many models, some perform better than others, but the rapid decline of sea ice since ~1997 is difficult for most GCMs to accurately simulate. Stroeve et al. (2007) compared observations of September sea ice extent with 13 IPCC AR4 climate models projections (Figure 12). Not one GCM ensemble mean accurately represented the rate of decline when compared to the observations. In fact, the observational rate of decline was much steeper than the multi-model ensemble mean and the latter part of the observations fell well outside of the standard deviation range. Those models indicated that the first seasonally ice-free conditions to begin in ~2075.

25
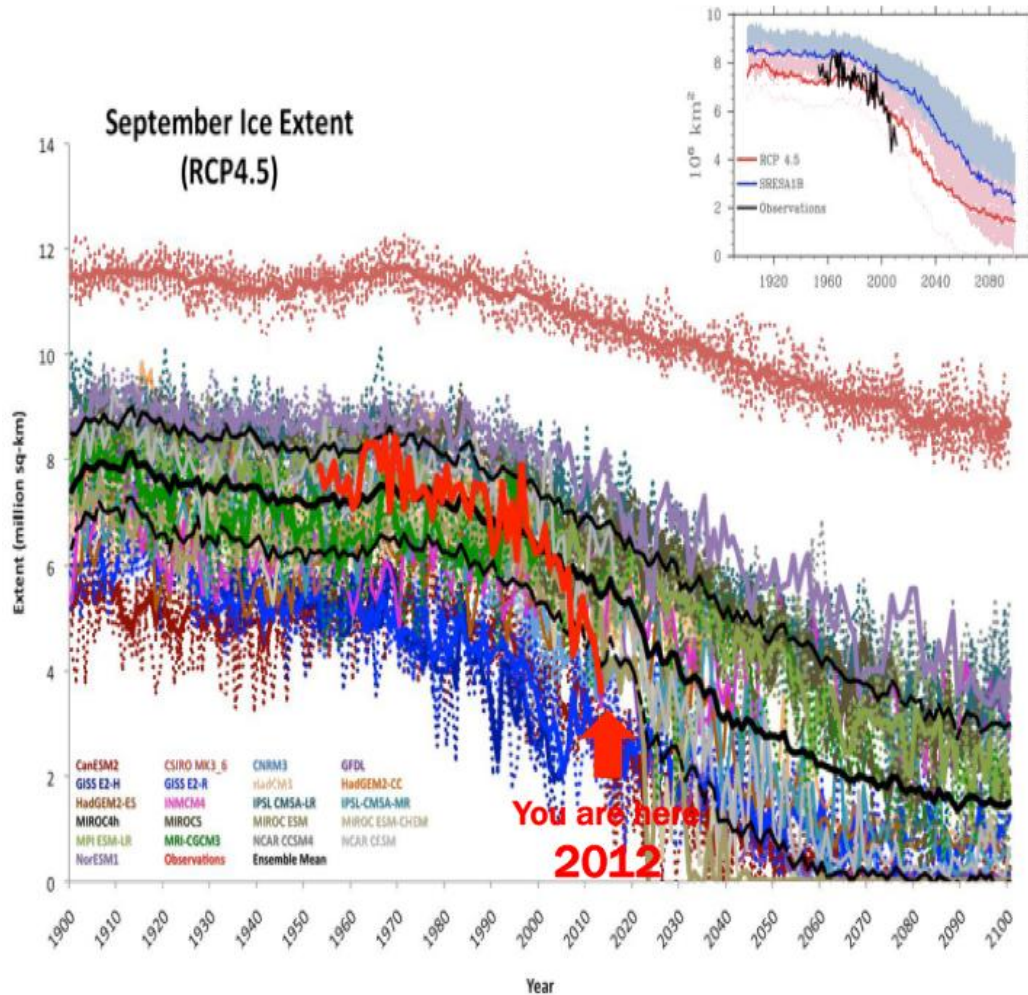
Time series of modeled (colored lines) and observed (solid red line) September sea ice extent from 1900 to 2100. All 56 individual ensemble members from 20 CMIP5 models are included as dotted colored lines, with their individual model ensemble means in solid color lines. The multi-model ensemble mean is based on 38 ensemble members from 17 CMIP5 models (shown in black), with +/- 1 standard deviation shown as dotted black lines.

Figure 13.   Comparison of the September sea ice extent from observations and 20 CMIP5 models (After Stroeve et al. 2012). Note: the observed value for 2012 was drawn as an addition for the comparison purposes of this thesis and is not exact.

Stroeve et al. (2012) made a similar comparison of observations of September sea ice extent, but this time with 20 models from the Coupled Model Intercomparison Project Phase 5 (CMIP5) under the representative concentration pathway (RCP) 4.5 future emission scenario from the World Climate Research Programme (WCRP) (Figure 13). RCP4.5 works to stabilize radiative forcing at 4.5 W/m^2 in the year 2100. This results in approximately 550 ppm of CO_2 by 2100 (Meehl et al. 2012). The previously used Special

Report on Emissions Scenario (SRES) A1B emission scenario attains CO2 levels of 750 ppm by 2100. RCP4.5 is less a less aggressive scenario (Stroeve et al. 2012). Though the agreement between model results and observations were better than before, the models still inadequately represented the observations especially toward the end of the time-series. Moreover, this time some models indicated seasonally ice-free conditions as early as ~2030. The results indicate that the models were adjusted somewhat, but not enough to represent observed variability through 2012.

This indicates that there is still much to understand about sea ice and the mechanisms and feedbacks within the Arctic. Several studies have described the annual decline of sea ice extent based on satellite data, in-situ observations, model predictions, or a combination of these methods (e.g., Comiso et al. 2008; Rigor and Wallace 2004; Stroeve et al. 2007). Perhaps the commonly used measures of sea ice extent and area inadequately represent the 'true' state of sea ice as they only account for two dimensions of three-dimensional property evolving in time. A more complete understanding of the recent Arctic sea ice decline requires an evaluation not only of ice extent, but rather of ice volume, which requires knowledge of the ice thickness.

Maslowski et al. 2012 compared NSIDC observational data with the NAME regional ice-ocean model with 9km resolution from 1979–2004 and found that:

1. There was a relative sea ice extent change of ~16% from 1979–2002.

2. There was a relative thickness change of ~44% from 1979–2002 which is more than twice that of ice extent

This indicates that ice cover is possibly decreasing at a much faster rate and our understanding of the rate of ice loss may be well underestimated. While the September ice extent minimum has long been a benchmark indication of the rate of decline of Arctic sea ice, the rate of change in sea ice volume/thickness has set record numbers almost every year since 1997, with much less notoriety. This is because sea ice thickness measurements cannot be conducted basin-wide with regularity, and total arctic sea ice volume estimates are primarily derived from models, which are subject to uncertainty. Maslowski et al. (2012) have combined NAME October-November sea ice volume

estimates for 1979–2004 with Kwok et al. (2009) observational estimates for October-November for 2004–2007 (Figure 14) and found that the combined rate of change was -1,120 km^3/year. They projected, that at that rate it would take only 9 more years (+/- 3 years when standard deviation is accounted for) to reach a nearly ice-free Arctic Ocean in summer.
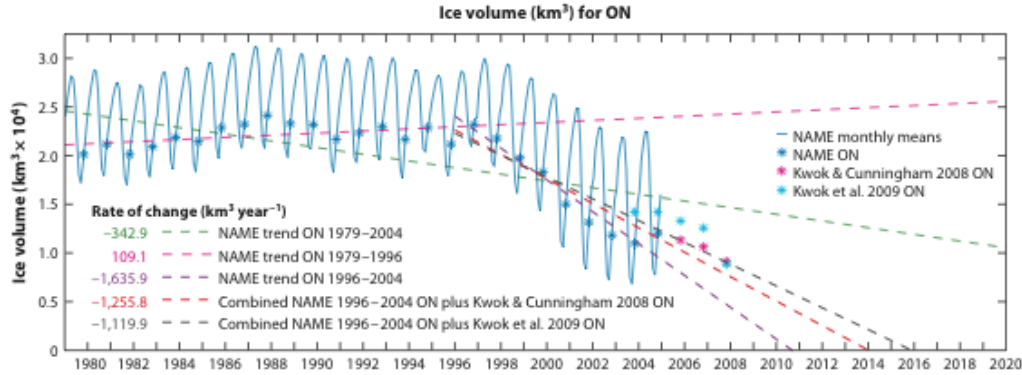
Arctic sea ice-volume estimates from observations and from the NAME model. For the observations, the October-November (ON) means are illustrated for 2003–2007, taken from Kwok & Cunningham (2008) (magenta stars) and Kwok et al. (2009) (light blue stars). For the NAME model, the time-series of monthly means for 1979–2004 (solid blue line) and the ON mean (blue stars) are shown. The dashed green line is the model ON trend for 1979–2004. The dashed magenta line is the model ON trend for 1979–1996, and the dashed purple line is the model ON trend for 1996–2004. The red and dark grey dashed lines show the calculated linear trend for 1996–2004 [combined NAME/ON1996–2004 plus Kwok & Cunningham (2008) and combined NAME/ON 1996–2004 plus Kwok et al. (2009), respectively]. The numbers labeled rate of change are sea ice volume trends per year based on different results shown in the symbol key.

Figure 14.   Sea ice volume estimates from the NAME model and observations taken from Kwok & Cunningham (2008) and Kwok et al. (2009) (From Maslowski et al. 2012).

They argue that regardless of the high uncertainty associated with such an estimate, it provides a lower bound of the time range for projections of seasonal sea ice cover. The fact that GCMs and higher resolution regional models, such as the NAME model, produce estimates that range from ~2075 (Stroeve et al. 2007) to ~2030 (Stroeve et al. 2012) to ~2016 (Maslowski et al. 2012) indicates that there is a need for improved understanding and model representation of physical processes and interactions specific to polar regions.

2.   Sea Ice Thickness and Age

It has long been recognized that many physical properties of sea ice depend upon the thickness (Thorndike et al. 1975). Three characteristic of sea ice that help determine the global distribution of sea ice mass are: seawater freezes at roughly $-1.8^{\circ}C$ and melts between ~-1.8 and $0^{\circ}C$, sea ice is buoyant and supports snow, and sea ice drifts and deforms. The growth and melt, in addition to the thermodynamic control, is affected by salinity and the presence of snow and its movement is affected by winds and currents above and beneath the ice, thus the thickness regional thickness distribution is influenced by thermodynamics and dynamics at a fine scale. The thermodynamic cycle and mechanical forcing greatly influence the thickness and are responsible for ice mass changes at both the atmospheric and oceanic interface.

In general, sea ice thickness observations are difficult to obtain and commonly include errors associated with each method of measurement. Given this difficulty, ice age is commonly used as a proxy for thickness estimations. First year (FYI) and multi-year ice (MYI), which is ice that lasts through at least one melt season, physically differ from one another due to the fact that as sea ice remains in seawater over several seasons, it rejects brines back into the ocean below or sometimes onto the sea ice surface, effectively reducing the salt content and increasing the strength of the remaining sea ice (Tucker III et al. 1992). The differences in salt content result in different surface characteristics and allow for remote sensing techniques to differentiate between ice of different ages. This is important to understanding sea ice dynamics as ice strength increases with thickness and age due to brine rejection from within the ice (Kovacs 1996). Thorndike et al. (1975) showed that the approximation, used in many ice models even today, for the compressive stress based in statics of sea ice is proportional to the ice thickness. This was also discussed in Hibler III (1979) as well as more recently in Maslowski and Lipscomb (2003).

Methods of obtaining ice thickness/age observations include drifting or moored buoys, submarine upward looking sonar (ULS), and remote sensing techniques.

a. Buoy Measurements

The International Arctic Buoy Programme (IABP) maintains a network of drifting buoys in the Arctic Ocean to provide meteorological and oceanographic data for real-time operational requirements and research purposes. In-situ measurements by oceanographic instruments form an integral part of the global ocean observing system (GOOS) and also provide a means of verifying numerical model results. Of particular interest and relevance to sea ice thickness, the IABP maintains two Lagrangian observation systems that move with an ice floe, making high resolution measurements of sea ice and ocean characteristics: the ice-tethered profiler (ITP) (Krishfield et al. 2008) and the ice mass-balance buoy (IMB) (Menge et al. 2006).

b. Submarine Upward Looking Sonar (ULS)

Upward Looking Sonar (ULS) measures ice draft, which accounts for approximately 85–90% of the total ice thickness (Rothrock and Wensnahan 2007). ULS data from submarines is arguably the most accurate source for determining sea ice thickness, though cruise tracks are spatially limited, but repeated they allow determining long-term trends in sea ice variability. It is important to note, however, that measurements of sea ice draft provides no information about relative contribution of sea ice and snow thickness to buoyancy, which is fundamental for narrowing estimates of total arctic ice mass. United States Navy (USN) submarines have been operating and collecting ULS data in the Arctic since the Cold War era. The data is marked as classified, but some has been declassified and made available to the scientific community. Ice draft data from about 40 submarine cruises, between 1958 and 2000, which covered over 120,000km of track, or about 38% of the Arctic Ocean, has been released (Rothrock and Wensnahan 2007). Several studies have analyzed these data sets (e.g., Rothrock et al. 1999; Rothrock et al. 2008).

The Science Ice Exercise (SCICEX) program, formally established in 1994, included civilian scientists joining Navy personnel on a submarine to acquire scientific data including ice thickness measurements via the ULS. In 2000, the USN and National Science Foundation (NSF) signed a memorandum of understanding for SCICEX

Phase II. This memorandum introduced Science Accommodation Missions (SAMs), where time is set aside for the collection of unclassified scientific data during otherwise classified submarine exercises (SCICEX Science Advisory Committee 2010). These missions will continue to occur until they are deemed obsolete or impractical. For a number of years the USN has also conducted biennial Ice Exercises (ICEXs), with the goals of testing submarine capabilities in the Arctic environment and conducting scientific research.

c. Remote Sensing Techniques

Looking at sea ice from the opposite perspective, the snow/ice-atmosphere interface, ice thickness measurements can be derived from the measurement of the ice freeboard, which is the vertical distance between the air-snow interface and the local sea surface and accounts for approximately 10–15% of the total ice thickness (Kwok and Cunningham 2008). These measurements are usually derived via satellite or aircraft platforms utilizing radar and laser altimeters. Advantages include large spatial extent, or satellite footprints, that cover massive regional repeated tracks. Disadvantages include comparison limitations due to the fact that complete regional images are actually mosaics, built from a series of satellite passes that are constructed over multiple days, vice a snapshot in time as would be produced by a model. Additionally, the calculation of ice thickness from ice freeboard can be very complex and somewhat approximate due to variable snow thickness, snow loading, and sea level slope.

The Ice, Cloud, and land Elevation Satellite (ICESat) was part of NASA's Earth Observing System covering 93% of the Arctic (Kwok et al. 2009). Launched in 2003, it utilized a spaced based altimeter or LIDAR by command. It was retired in 2010 after its scientific payload shutdown and was unresponsive. ICESat-II is scheduled to be launched in 2016, as a follow up to ICESat. Several studies (e.g., Kwok and Cunningham 2008; Kwok et al. 2009; Kwok and Rothrock 2009) have made use of the ICESat data sets and found that they were able to distinguish between first year (FYI) and multiyear ice (MYI) due to their different reflectivity; similar ice thickness trends were found when

compared with ULS data; and there has been an overall decrease in MYI with a significant increase of FYI over the last decade.

Utilizing satellite sensors, such as a scanning multichannel microwave radiometer (SMMR), a special sensor microwave/imager (SSM/I), and a series of advanced very high resolution radiometer (AVHRR) sensors, differences in salt content can be detected as they emit differing brightness temperatures, a measure of the emissivity of the surface material which can be used to estimate ice age (Maslanik et al. 2007). Maslanik et al. (2007) found a dramatic change in the age of sea ice in the central Arctic Basin since the mid-1980s (Figure 15). In 1987, 57% of the ice pack was at least 5 years old, and a quarter of that ice was at least 9 years old. By 2007, only 7% of the ice pack was at least 5 years old, and virtually none of the ice was at least 9 years old. Other studies have shown that since the 1980s, MY ice has been diminished from covering ~80% of the Arctic in that decade to only ~30% of the area since the 1990s (Rigor and Wallace 2004; Drobot et al. 2008; Kwok and Cunningham 2010).

This loss of thick MYI may be explained by the positive AO pattern seen during the mid-1980s through the mid-1990s, when the Beaufort Gyre circulation relaxed and sea ice was exported from the Arctic via the TDS. Given the thickness distribution at that time, much of the thick MYI that was normally retained for several years was exported and replaced by thin first year ice the following winter. Areas, such as the central Arctic and the Canadian Archipelago, were relatively stable in the past, but lost vast amounts of old and thick ice (Maslanik et al. 2011). The younger and thinner ice that replaced MYI is more likely to experience even more abrupt changes in ice export under the same atmospheric and oceanic forcing (Maslanik et al. 2007). Along with sea ice export and melt, redistribution of MYI has shifted the ice-covered area in the Arctic toward younger and thinner ice, which is more prone to drift, deform, and melt during summer. As a revealing example, the drifting speed underwent in 2006–2007 by the polar schooner Tara was twice as large as the mean drifting speed of the Fram ship 115 years ago (Gascard et al. 2008). Tara drifted along the TDS beginning in 2007 and reached the open ocean through Fram Strait in late January 2008, i.e., 1 year earlier than expected by scientists (Gascard et al. 2008).

As the thickness of sea ice changes so does the drift speed. Using buoy data from the IABP, Rampal et al. (2009) found that the sea ice mean speed and mean strain rate had substantially increased over the last 29 years. They also found that sea ice kinematics play a fundamental role in the albedo feedback loop and sea ice decline, as increasing deformation means more fracturing and more lead opening, therefore decreasing the albedo. "This accelerates sea ice thinning in summer and delays freezing in early winter, therefore decreasing the mechanical strength of the cover and allowing even more fracturing, larger drifting speed and deformation, and possible faster export of sea ice through Fram Strait" (Rampal et al. 2009). Additionally, Maykut and McPhee (1995) showed that turbulent oceanic heat fluxes are proportional to ice drift through ice-ocean stress, thus an increased speed increases the ice-ocean stress and increases turbulent oceanic heat fluxes.

3.   Sea Ice Deformations

Sea ice mechanics has a great impact on the momentum and heat exchange with atmosphere and ocean, and greatly affects the mass balance of sea ice in the Arctic (Rampal et al. 2009, Kwok and Sulsky 2010). The mean arctic sea ice thickness decrease of past decades has reduced internal compressive strength of the pack, so that wind and ocean current stresses often results in localized increases in drift and deformation. "Exposed open water, associated with mechanical failure of the ice cover, controls the abundance of thin ice and the many surface processes dependent on thin ice, such as turbulent heat flux to the atmosphere" (Kwok et al. 2008). Moreover, it is the prevalence of thin ice categories amongst thick floes that largely determines the overall compressive strength of the pack (Rothrock, 1975).

A small-scale dynamic response of the winter sea ice cover to gradients in large-scale surface wind stress is localized along quasi-linear fractures where openings and closings are found. Nearly all deformations on the ice cover are localized along these kinematically active linear features known as linear kinematic features (LKFs) (Kwok 2001). LKFs are long, narrow features that may contain open water, new ice, nilas, young-ice, FYI, rafted ice, or ridged ice and can have widths of kilometers and lengths up

to hundreds of kilometers (Kwok 2001; Kwok 2006). Schulson (2004) examined these fracture features, or LKFs, using Landsat-7 and RADARSAT imagery, by an aerial survey, and through observations in the laboratory of specimens loaded to brittle failure and found that regardless of scale, which spans the range from kilometers to millimeters, the LKFs looked alike. This would indicate a fractal property of both sea ice morphology and deformation.

RADARSAT-1 is an Earth observation satellite launched in 1995 and includes a synthetic aperture radar (SAR) with multiple polarization modes and resolutions as high as 100m (Kwok et al. 2008). High-resolution radar imagery of the Arctic Ocean is transformed into estimates of ice motion, deformation, age, and thickness by the RADARSAT Geophysical Processor System (RGPS) as part of NASA's making Earth science data records for the use in research environments (MEaSURE) program (Kwok et al. 2008). RGPS provides basin-scale views of the above parameters over entire seasons based on continuous sampling of Lagrangian elements on the ice cover (Kwok et al. 2008). RGPS data is obtained by tracking sea ice motion from satellite images on a high-resolution grid, which is developed into data sets of small-scale kinematic and deformation fields. The initial grid then moves and deforms throughout the selected time frame to produce displacement and trajectory fields of the ice pack. This allows for tracking of ice floes to produce velocity fields from which deformation products such as divergence, vorticity, and shear can be derived. These RGPS data sets provide the best basin wide observational coverage of fine scale deformation events and are used as a benchmark for comparison for many sea ice deformation studies.

D.   ARCTIC SEA ICE MODELING

Numerical models, by far, provide the best spatial and temporal resolution of any technique available. Coupled with the ability to make future predictions, numerical modeling can put an amazing amount of information at ones fingertip. Numerical modeling has dramatically evolved over the last 30 years to include powerful supercomputers capable of trillions of operations per second and terabytes of output data, high resolution regional models, GCMs, hybrid grids and fully coupled Earth system

models. The capabilities of this form of analysis seems endless, but still, models struggle in some areas including the correct representation of physical processes and mechanisms within the Arctic system.

1.   The Sea Ice Model

The dynamic thermodynamic sea ice model couples the dynamics to ice thickness characteristics. As ice becomes thicker, the coupling in the dynamics becomes stronger (Hibler III 1979). Dynamic forcing within sea ice results in regions of sea ice divergence and convergence. Divergence results in high oceanic heat losses and while convergence of sea ice results in reduced heat losses (Hibler III 1979). Modeling of sea ice is based on the principles of conservation of mass, momentum and energy by representing the thermodynamic and dynamic forcings acting on the ice as well as maintaining continuity through a thickness distribution. The momentum balance in sea ice is described as:

$$m\frac{\partial \tilde{u}}{\partial t} = \tilde{\tau}_w + \tilde{\tau}_a - mfK \times \tilde{u} - mg\nabla\eta - m(\tilde{u} \cdot \nabla)\tilde{u} + \frac{\partial \sigma_{mn}}{\partial x_n}$$

(1)

Notation			
constant			
k	unit normal vector upward from the sea surface		
g	acceleration due to gravity	9.80	ms^{-2}
variables			
t	time		
m	ice mass per unit area including freeboard snow		
$\tilde{u} = (u,v)$	horizontal ice velocity		
$\tilde{\tau}_w$	surface stress at the ocean-ice interface		
$\tilde{\tau}_a$	surface stress at the ice-atmosphere interface		
f	Coriolis parameter		
η	sea surface height		
σ_{mn}	internal two dimensional stress tensor	$m,n = 1,2$	
x_n	two dimensional axes for internal stress		

(Wadhams, 2000)

The Coriolis force, water drag, air drag, gradients due to the tilt of the sea surface, and the internal ice stresses resulting from floe-to-floe interaction are all represented. Ekman turning is represented by $mfK \times \tilde{u}$, while the surface gradient is represented by $mg\nabla h$. The advective acceleration or nonlinear terms are represented by $m(\tilde{u} \cdot \nabla)\tilde{u}$.

35

Lastly, the internal force on sea ice or the internal ice force vector is based on changes in the internal two dimensional stress tensors represented by $\frac{\partial \sigma_{mn}}{\partial x_n}$, where:

$$\frac{\partial \sigma_{mn}}{\partial x_n} = \frac{\partial \sigma_{11}}{\partial x_1} + \frac{\partial \sigma_{22}}{\partial x_2} + \frac{\partial \sigma_{21}}{\partial x_1} + \frac{\partial \sigma_{12}}{\partial x_2} = \vec{F}_{INT}$$

(2)

A nonlinear viscous-plastic (VP) rheology proposed by Hibler III (1979) became the standard sea ice dynamics model. In the VP sea ice model, the change in the internal stress tensor within the momentum equation of sea ice (Wadhams 2000) is highly nonlinear and represents the internal force on sea ice. The internal stress tensor is a function of the bulk viscosity, shear viscosity, strain rate, compressive strength of sea ice (P), and some elliptical yield curve operator most commonly represented by a VP response in principal stress space (eigenvalues) (Hibler III 1979).

$$\sigma_{mn} = \zeta \dot{e}_{kk} \delta_{mn} + \mu \left(2\dot{e}_{mn} - \dot{e}_{kk} \delta_{mn} \right) - \frac{P \delta_{mn}}{2}$$

(3)

Variables

$\zeta = \min(P/2\Delta, 2.5P \times 10^8)$	bulk viscosity
$\mu = \zeta/4$	shear viscosity
$\Delta = f(\dot{e}_{mn})$	elliptic yield curve operator
$\dot{e}_{mn}$	strain rate
P	compressive strength

(Hibler III, 1979)

The majority of the time the stress state of sea ice is plastic, which is on the elliptical curve, as described in Figure 15, below. A common problem in models is that the VP principal stress state is under an isotropic assumption, while sea ice is an anisotropic material, but work is being done to approximate an anisotropic deformation with a modified Coulombic yield curve where the shear strength is proportional to the compressive strength (Hutchings et al. 2005).

36
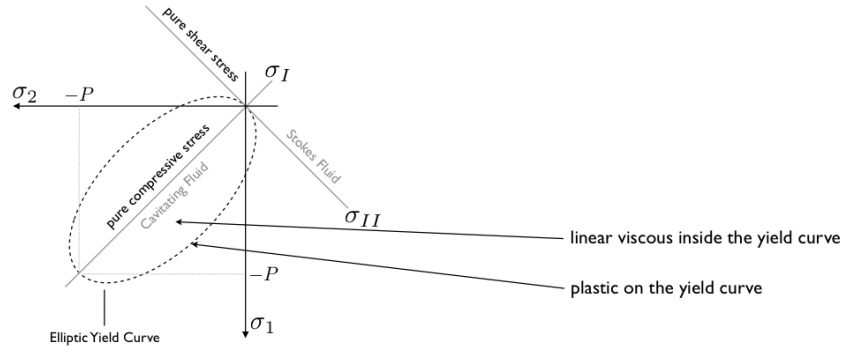
Figure 15.   Sea ice deformation in principal stress space under an isotropic assumption
(After Ip, et al. 1991; From Roberts, 2012)

Numerical difficulties, within the VP model, are associated with the large range of effective viscosities within the model. When the model is coupled to an ocean or atmosphere model, the computational resources required for become very cumbersome on the system (Hunke and Dukowicz 1997). Work has been done on the behavior of an elastic-viscous-plastic (EVP) model for sea ice dynamics, with particular attention to a necessary numerical linearization of the internal ice stress term in the momentum equation (Hunke and Dukowicz 1997; Hunke 2000). The EVP model was found to be desirable because of its computational characteristics with regard to parallelization issues, the expedient handling of the nonlinear internal ice stress term, and its explicit numerical formulation that efficiently updates all rates of strain that determine the ice stress. Overall, the EVP model provides more accurate results for shorter timescales, reproduces VP model behavior on longer timescales, and is computationally more efficient (Hunke and Dukowicz 1997).

The VP (Hibler III 1979) and EVP (Hunke and Dukowicz 1997) rheology implies that for stress states inside the plastic yield curve, sea ice behaves as a viscous fluid while ice flows as a perfect plastic when the stress states reaches the envelope, see Figure 15. This viscous flow is considered to result from the average effect of many "plastic" events (Hibler III 1977). This relies on a hypothesis that the stress and strain are locally homogeneous (Rampal et al. 2008). The EVP framework is suited for numerical coupling

with other fluid layers (ocean, atmosphere) and the development of efficient methods to solve the momentum equation employing this rheology have made it widely used (Zhang et al. 2001; Rampal et al. 2008).

2.   Current Modeling Limitations

The coarse resolutions and sometimes crude parameterizations of critical physical processes used by some GCMs, end up affecting ice thickness and ocean conditions (Maslowski et al. 2007). This can limit the ability of many GCMs to accurately represent past variability as well predict future conditions (Maslowski et al. 2012). As previously discussed, Stroeve et al. (2007) and Stroeve et al. (2012) showed that many GCMs inadequately represented the rate of sea ice extent decline, compared to observations, indicating that there is still much to understand about sea ice and the mechanisms and feedbacks within the Arctic before our models can predict future conditions. Rampal et al. (2011) showed that IPCC climate models underestimate the observed thinning trend by a factor of almost 4 on average and fail to capture the associated accelerated motion. It was found that the coupling between the ice state (thickness and concentration) and ice velocity was unexpectedly weak in most models. Weak coupling is known to suggest underestimated positive feedback mechanisms. This could result in underestimations in sea ice velocity, are and thickness (Rampal et al. 2011).

Maslowski et al. (2012) analyzed the sea ice volume decline utilizing the 9km NAME model to project a much earlier time frame for seasonally ice-free conditions, 2016, vice ~2030 (Stroeve et al. 2012) or ~2075 (Stroeve et al. 2007). It is known that there are considerable uncertainties within all models, but it is interesting that the lower bound of these projections came from sea ice volume analysis vice sea ice extent as well as came from a much higher resolution regional model vice a coarse resolution GCM. Maslowski and Lipscomb (2003) showed that higher resolution model results improved the representation of ice thickness, concentration, deformation and drift by comparing 9-km and 18-km ice-ocean models. Maslowski et al. (2004) also showed the importance of resolving an accurate fine scale mean circulation through Fram Strait and Barents Sea for transport of heat, salt, and mass via narrow coastal currents and their effect on sea ice

variability in the eastern Arctic Ocean. Similarly, Stroeve and Maslowski (2008) followed this with a comparison of observations and high-resolution model results suggesting that sea ice thickness may be declining at a faster rate than sea ice extent.

The Rossby radius of deformation for the Arctic Ocean is approximately 10 km, thus even a model at 9km resolution is not be able to fully resolve many of the fine scale features and processes that have been proven vital to understanding the full Arctic system. The processes related to small scale features such as narrow coastal currents, freshwater exchanges, double diffusive processes, eddies and topographic steering play an important role in sea ice variability and have driven further advancements in high resolution ice-ocean models, but has yet to be fully embraced by the GCM community (Maslowski et al. 2008). The resolution, numerical treatment, and flux-exchange mechanisms associated with coupling interaction dictate the degree to which sea ice variability can be realistically modeled (Maslowski et al. 2012). Improvement of the representation of processes through increased model resolution and improved parameterizations as well as increasing the number of Arctic processes included in models is a first step toward a better solution (Maslowski et al. 2012).

3.   Spatial Characterization of Sea Ice Deformation

Sea ice responds to forcings over a broad range of spatial and temporal length scales. Large-scale circulation of sea ice determines the advective part of the ice balance. Shorter length scales are particularly important because the response of sea ice to gradients in forcings and boundary conditions is concentrated in LKFs. (Kwok et al. 2008). Sea ice dynamics models must accurately represent large and small scale processes as well as ice velocities and deformation rates in order have a good representation of the ice thickness distribution and open water fraction (Kwok et al. 2008; Girard et al. 2009).

In order to investigate the temporal and spatial scaling factors, the dispersion of buoys in trajectories and grid patterns is commonly used (e.g., Rampal et al. 2008; Girard et al. 2009; Rampal et al. 2009; Hutchings et al. 2010). Recent analysis of drifting buoy trajectories and fine scale sea ice kinematics produced by RGPS revealed that sea ice

deformation is a fractal process in space and time (Marsan et al. 2004; Rampal et al. 2008; Girard et al. 2009). Leads and floe sizes follow a fractal distribution, suggesting that the mechanism controlling sea ice failure is scale invariant (Hutchings et al. 2010). Investigation of internal sea ice stresses and RGPS-derived strain rates also revealed the elasto-brittle behavior of ice cover (Weiss et al. 2007).

Through the dispersion of pairs of drifting buoys, using IABP buoy data sets, Rampal et al. (2008) found that:

1. The deformation of sea ice is the result of a highly intermittent and heterogeneous dispersion process.

2. The deformation depends on both space and timescales. It follows a power law model that is scale invariant over several orders of magnitude in time and space.

3. The values of the exponents of the power functions depend on both time and space scales. This indicates that time and space are coupled.

4. Even for large timescales, i.e., several months, and for the Arctic basin scale, i.e., 1000km, Arctic sea ice deformation does not mimic viscous flow, a contradiction to the classical sea ice modeling assumption.

Most of sea ice deformation is accommodated by active fractures and faults at various scales (Girard et al. 2009). This can explain the intermittency and spatial heterogeneity of sea ice deformation (Weiss et al. 2009), but the broad temporal and spatial spectra of sea ice motion presents a particular challenge to observational systems and model simulations (Kwok et al. 2008) begging the question: to what extent can current sea ice models simulate such a multiscale fracturing process (Girard et al. 2009)?

Marsan et al. (2004) showed that a power law decrease of the average strain rate with increasing scale L was observed in the RGPS observations. The exponent H was found to be equal to -0.2. Girard et al. (2009) made a similar finding while Hutchings et al. (2010) found the exponent H equal to -0.19. Long-range spatial correlations within the strain rate field are present. This random spatial reshuffling of the strain rate values suppresses power law scaling (Marsan et al. 2004).

Previous studies (e.g., Lindsay et al. 2003; Kwok et al. 2008; Girard et al. 2009) have shown that numerical models are capable of reproducing the large-scale drift patterns, but the simulated deformation rates show rather poor correlation with RGPS observations, especially at small scales. Girard et al. (2009) found that model results from the Louvain-la-Neuve Ice Model (LIM) and Los Alamos Sea Ice Model (CICE) exhibited incorrect strain rates when compared to RGPS and the statistical properties of sea ice deformation were not well simulated by the models as they were unable to reproduce the spatial and temporal correlations of the deformations fields. Girard et al. (2009) suggested that the mechanical framework currently used by the models may be inappropriate and a different framework based on the elastic interactions could improve the representation of the statistical and scaling properties of ice deformation.

Spreen (2010) also described the difference in spatial scaling of the sea ice deformation rate between observed RGPS data and the ECCO2 coupled sea ice-ocean model results as 'different', especially for small-scale deformations and LKFs. It was found that, in the model, the power law scaling factor, strongly depends on the ice concentration range used. Spreen (2010) also noted that model physics seem to be inadequate for correct reproduction of some aspects of sea ice kinematics, but increases in model resolution produced more and stronger confined ice deformations. The observed power scaling law of sea ice deformation was found in the ECCO2 model; however, the scaling exponent almost exclusively depends on the considered sea ice concentration range. By changing the model sea ice strength formulation away from the linear dependence on ice thickness the modeled and observed deformation fields become more consistent.

THIS PAGE INTENTIONALLY LEFT BLANK

III. U.S. NAVY RELEVANCE

A. A BRIEF HISTORY OF ARCTIC EXPLORATION AND REGIONAL DEVELOPMENT

1. Exploring the Arctic

All information, unless otherwise referenced, for this section (III.A.1) is from AMSA, 2009. The first and original Arctic explorers were the indigenous people of the region. In order to find a more direct route to India, Southeast Asia and China, to support the lucrative trade exchange between regions, Europeans began investigating the possibility of a Northwest Passage (NWP) in ~1490. In fact, Christopher Columbus was in search of this direct route when he stumbled upon the North American continent in 1492. In Russia, the idea of a possible seaway connecting the Atlantic and the Pacific referred to as the Northeast Passage (NEP) or the Northern Sea Route (NSR) (Figure 16), was first put forward in 1525.
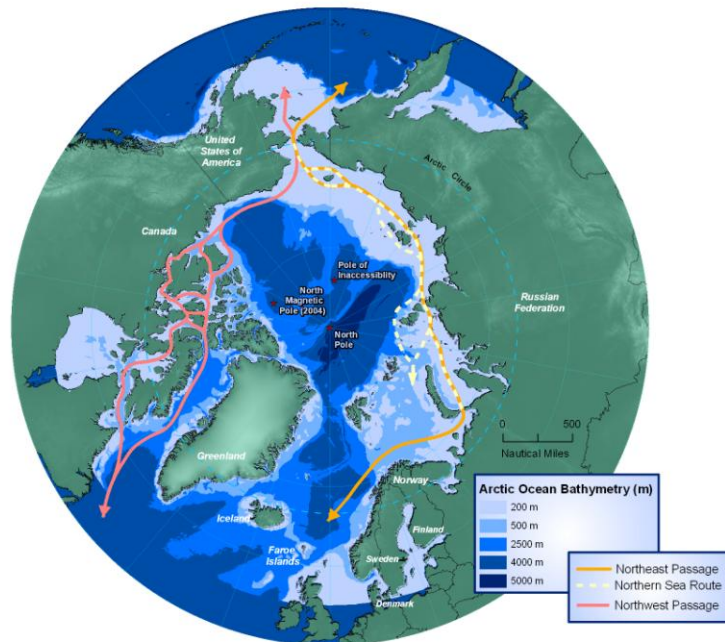
Figure 16.   Northwest Passage (NWP) and Northeast Passage (NEP) aka Northern Sea Route (NSR) (From Arctic Marine Shipping Assessment (AMSA), 2009)

Upon the settlement of the New World, many attempts followed to find the NWP, with most via Hudson Bay, including Martin Frobisher, John Davis, Henry Hudson, and Luke Foxe. In the 1800s the British Royal Navy explored the labyrinth of islands and channels that is now the CAA partially due to a massive search operation performed for Sir John Franklin's ships, Erebus and Terror, that sailed north into Baffin Bay and disappeared in 1845 with 129 men. It was not until 1906 that the Norwegian explorer Roald Amundsen in his 47-ton sloop, Gjoa, emerged in the Pacific to become the first vessel to complete the NWP transit. The voyage took Amundsen all of three winters to complete and it is believed that credit for his survival can be attributed to the Inuit. The first complete transit from west to east of NWP was completed in 1942 by the Canadian ship St. Roch. Captain Henry Larsen made the return trip from east to west in only 86 days and became the first vessel to transit the NWP in one season.

As far as the NEP, in 1726, the first northern expedition, led by Vitus Bering, discovered the Bering Strait while seeking the NEP. Baron Adolf Erik Nordenskjöld of Sweden first traversed the NEP in 1878 aboard the Vega. Two expeditions achieved transits of a substantial part of the NEP, including Fridjof Nansen's Fram (1893–1896) and the Baron Eduard Toll expedition on board the Zarya (1900–1903). Maud, also commanded by Amundsen (1918–1920), was the fourth ship to complete a transit of the NEP and, as a result, Amundsen achieved the distinction of being the first person to circumnavigate the Arctic Ocean, since he had now linked up the track of his voyage in the Gjoa. Since the early 1900s, transits of the NWP and NSR remained fairly sporadic until the 1970s when development in the Arctic region began and the export of natural resources became big business.

2.   The Northwest Passage (NWP), Alaska, and the Canadian Arctic

Until recently, the harsh climate and year round widespread sea ice cover has long left the Arctic region sparsely populated, relatively lightly traveled/explored (successfully), fairly undisputed and of little concern or value to most nation states. In fact, in relevance to U.S. involvement, oil was only first discovered in 1841 in what is now Prudhoe Bay, Alaska; coal mining began in 1857 on what is now Coal Island,

Alaska; and gold was first discovered in 1872 near what is now Sitka, Alaska. Even still, the U.S. only paid 7.2 million dollars in gold, roughly two cents per acre, to Russia for the territory that is now known as Alaska, but at the time was widely referred to as "Seward's Folly" after the U.S. statesman William Henry Seward who negotiated the unpopular purchase. By 1897, the Klondike Gold Rush began and more 100,000 people began the trek north to seek their fortune.

The Canadian and American military relationship drew close with the establishment of the Permanent Joint Board on Defense on August 18, 1940, also known as the Ogdensburg agreement, which was devised to provide a framework for closer continental defense cooperation in the face of World War II (WWII). The war brought a surge in joint Arctic activities, such as the establishment of the Alaska Highway, the Northwest and -east Staging Routes, the Mackenzie River air route, the Canol Pipeline (Canada Oil), and Canada-U.S. military operations in the Aleutian Islands (Woitkowitz 2012). Canadian apprehensions began during the Canol Pipeline project as Ottawa learned about the establishment of the oil pipeline only after the United States had commissioned a contractor for its construction (Woitkowitz 2012).

Starting in 1945 national security became a primary driver for navigation in the NWP. Largely as a result of American interest in the North, Canada was driven to acquire icebreakers and cultivate a greater navigational ability in Arctic waters. Increases to Canada's Arctic vessel capacity, in the early-to-mid 1950s, took the form of the CGS d'Iberville (1952) and the HMCS Labrador (1954) (AMSA 2009). The Canadian icebreaker HMCS Labrador became the first ship after the St. Roch, as well as the first armed Canadian ship to successfully complete transit of the passage. In 1957, the Labrador escorted three U.S. Coast Guard icebreakers–Storis, Spar and Bramble–on part of the journey from west to east through the NWP, in a successful attempt to gauge whether ships could escape to the east when iced-in on the west (AMSA 2009).

The 1950s saw an intimate defense cooperation continue between Canada and the United States due to growing Soviet Cold War tensions. This tension resulted in the fear of potential nuclear attacks via the Arctic and in response the United States pushed for the construction of radar stations to monitor the skies across the Canadian Arctic

(Woitkowitz 2012). With a linked chain of 63 communication and radar systems spanning 3,000 miles, the resultant Distant Early Warning (DEW) Line (Figure 20) was designed to monitor the Arctic airspace as well as deter and provide advance notice of potential attacks. This not only consisted of cooperation between Canada and the United States, but Denmark as well as several stations were constructed in Greenland in order to be fully monitoring. Negotiations between Washington and Ottawa over the construction and the operation of the DEW Line increasingly produced resentments and concerns on the part of Canadians. This was probably due to the substantial U.S. presence Canadian Arctic (Woitkowitz 2012), which raised questions about Ottawa's ability to exercise sovereignty and protect Canadian jurisdiction in its northern territory. Ironically, the DEW Line quickly became ineffective and out of date as the Cold War arms race fueled rapid technological advancements. The DEW line was eventually updated to the long-range radar systems of the North American Aerospace Defense Command (NORAD) North Warning System (NWS), circa 1985 (Figure 17).
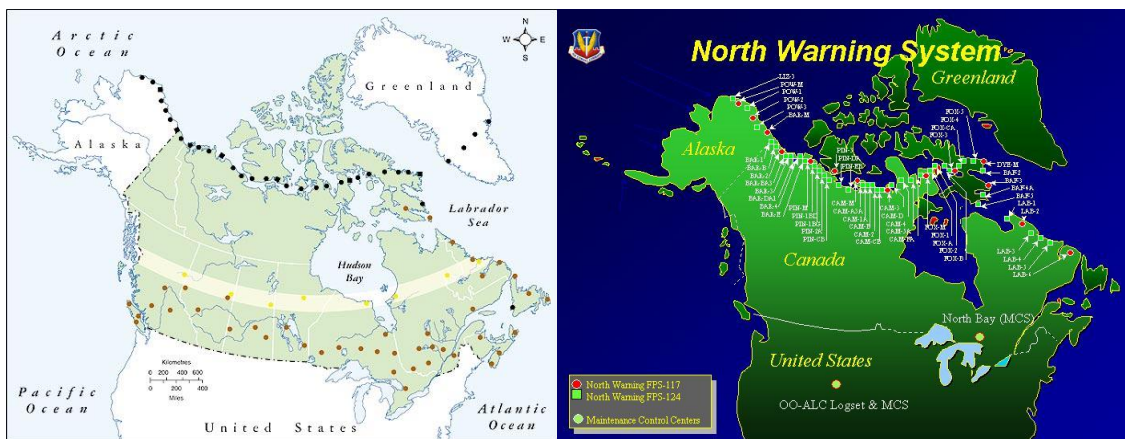
Figure 17.   The map on the left is the of early warning radar station lines built through collaboration between the U.S., Canada, and Denmark in response to Soviet Cold War tensions. The black dots represent the DEW Line radar stations, the yellow dots represent the Mid Canada Line radar stations and the brown dots represent the Pinetree Line radar stations (From C. Johnson 2012, http://www.journal.forces.gc.ca/vo8/no2/lajeunes-eng.asp). The map on the left is the North American Aerospace Defense Command (NORAD) North Warning System (NWS) site map (From The U.S. Air Force Tactical Air Command 2012).

In 1960, President Dwight D. Eisenhower established the Arctic National Wildlife Range in northeastern Alaska as a means to preserve the area's wildlife, native peoples, and outdoor recreation. In 1980, this area was renamed the Arctic National Wildlife Refuge (ANWR) and doubled in acreage from 9 to 18 million acres. Under terms set by the Alaska National Interest Lands Conservation Act, the range was declared off-limits for the production of oil and gas. However, Prudhoe Bay, located west of the ANWR, was not included in the act. Upon discovery of oil in Prudhoe Bay in 1968, the U.S. government began plans to build an oil pipeline from Prudhoe Bay to the Northern Slope. The Prudhoe Bay region, in northwest Alaska, is now known as the largest oil field in North America. At its peak production in the 1980s, the oil field supplied up to 20% of the nation's total oil production.

In 1973 the U.S. oil crisis, and in 1974, construction began on the Trans-Alaska Pipeline System (TAPS). TAPS spans several hundred miles of feeder pipelines along Alaska's North Slope toward the U.S. mainland and includes 11 pump stations and the Valdez Marine Terminal. In 1989, the Exxon Valdez oil tanker ran into a reef in the Prince William Sound, spilling 11 million gallons of crude oil in what is now the second largest oil spill in U.S. history. In 2006, British Petroleum (BP) had a 267,000-gallon oil spill in Prudhoe Bay, originating from a pipeline in the wildlife-rich North Slope region of Alaska. With the rise in surface temperatures, gradual decline in sea ice, and opening of larger or new shipping lanes, an increase in tanker and shipping traffic in and out of the Arctic has been documented. The Deep Water Horizon oil spill in 2010, which is deemed the largest oil spill in the history of the petroleum industry as 4.9 million barrels of oil was released into the Gulf of Mexico, has caused great concern that a spill of this magnitude, associated with the increased shipping traffic, would become an even bigger disaster and wreak havoc in the Arctic region.

Through the 1980s, more than 30 complete transits of the NWP were undertaken by a variety of vessels, as the focus shifted from national security to economic development. In the summer of 2007, interest soared as the sea ice throughout the NWP melted and broke up enough to ignite considerable speculation that the passage could soon be open for shipping and transit. NWP could potentially run through different routes

in the CAA and has potential for cost savings for shipping between northeast North America and northeast Asia as well as routing between northern Europe and northwest North America when compared to canal routes (Suez or Panama) or cape routes (Good Hope or Horn) (Murnane 2012). This path, while more modest in its potential cost savings (~20%) for the shipping community, has been contested by the Canadians as an inland waterway in which their government would maintain sovereignty and control (Borgerson 2008).

B.   ARCTIC NATIONS AND POLITICS

The Arctic Ocean is unique to any other ocean in the world because it is surrounded by continental landmasses, which create a semi-enclosed basin representative of a large-scale estuary. The five nations with coasts surrounding the Arctic Ocean include: the U.S., Canada, Russia, Norway, and Denmark via Greenland. Figure 18 is political map of the Arctic region.

Figure 18.   Map of the Arctic Region showing the Arctic Ocean, adjacent seas and political boundaries. Red line shows 10°C isotherm for July (From U.S. Central Intelligence Agency 2010).

These countries along with Finland, Iceland, Sweden, and indigenous representatives are member states of the Arctic Council, which was formally established through the Ottawa Declaration of 1996. The Arctic Council is a high level intergovernmental forum to provide a means for promoting cooperation, coordination and interaction among the Arctic States, with the involvement of the Arctic Indigenous communities and other Arctic inhabitants on common Arctic issues, in particular issues of sustainable development and environmental protection in the Arctic (Arctic Council 1996). This body is limited, however, in its authority to oversee legitimate international agreements or impose legally binding restrictions on nations for abusing natural resources or disregarding sovereignty claims due to the U.S. refusal to accept security concerns as part of the Council's charter (Borgerson 2008).

The leading international treaty concerning maritime affairs including the rights and responsibilities of nations for their use of the ocean, as well as guidelines for economic and environmental resources within the world's oceans is the United Nations Convention on the Law of the Sea (UNCLOS). This treaty, which was internationally recognized in 1994, defines the rights of navigation through national and international waters and sets up key provisions for long-disputed territorial claims including continental shelf extent and exclusive economic zones (EEZs).
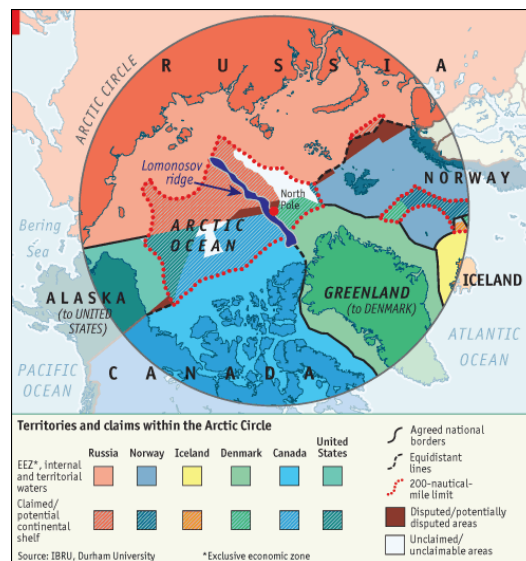
Figure 19.   Map of current and potential territorial claims (From *The Economist* 2009)

The five countries with coasts surrounding the Arctic Ocean are limited to EEZs of 200 nautical miles adjacent to their coasts. Upon ratification of the UNCLOS treaty, countries can make claims to extend their continental shelf, based on bathymetric features, and give themselves exclusive rights to the resources on or below the seabed of the extended shelf area. Canada (2003), Denmark (2004), Norway (1996) and Russia (1997) have all ratified this document and have ten years from the date of ratification to make claims to an extended continental shelf (2013, 2014, 2006, and 2007, respectively). Figure 19 is a map of current and potential territorial claims for each of the five coastal countries.

Norway made an official submission into the UN Commission on November 27, 2006 to extend the Norwegian seabed claim beyond the 200 nmi EEZ in three areas of the northeastern Atlantic and the Arctic: the "Loop Hole" in the Barents Sea, the Western Nansen Basin in the Arctic Ocean, and the "Banana Hole" in the Norwegian Sea.

On December 20, 2001, Russia made an official submission to the UN Commission to extend as far as the North Pole based on the Lomonosov Ridge extension. Moscow believes the eastern Lomonosov Ridge is an extension of the Siberian continental shelf (O'Rourke 2011). The annex of this undersea area would grant Russia over 50% of the Arctic Ocean basin. This is estimated by the U.S. Geological Survey (USGS) to hold as much as one-quarter of the world's remaining undiscovered oil and gas deposits (Borgerson 2008). The UN initially rejected the claim, in 2001. In 2002, the UN Commission requested additional research to evaluate the claim. In 2007, Russia dispatched a nuclear powered icebreaker and two MIR submersibles to take water and soil samples. The submersibles also planted the Russian flag on the sea floor at the North Pole (Vasilyeva 2010). Russia maintains this was not an act of territorial claim, but this highlights the rising tension with respect to territorial claims within the region. In April 2010, Russia and Norway reached an agreement over their respective borders in the Barents Sea that is thought to contain vast petroleum deposits under the sea floor (O'Rourke 2011; Isachenkov 2010). This dispute had been ongoing for over 40 years. Additionally, Some agreement has been achieved between the U.S. and Russia over a contested area of the Bering Sea. Though the nations remain friendly, some discourse

continues as diminishing natural resources from within the coastal margins become increasingly more accessible to each country (Isachenkov 2010).

Canada has not yet made an official submission to the UN Commission, but it has been recently reported that a submission to shelf extension is very near. Canada has also laid claims to its sovereignty in the Arctic Ocean. In 2006, Canada claimed the NWP as part of their internal waters. Most nations consider these straits to be international passages in which foreign vessels have the right of free passage for the purposes of transit. Canada has since developed eight new Arctic capable patrol ships to secure the passage. In the 2008 "Canada First Defence Strategy," Prime Minister Stephen Harper announced Canada's plans to establish a deep-water port and an Arctic Training Centre, to expand its military presence, and to increase satellite and aerial surveillance of the Arctic region. The U.S. and Canada continue to dispute their boundary in the Beaufort Sea, while Denmark and Canada disagree over the territorial rights to Hans Island (O'Rourke 2011).

Like Canada, Denmark has not yet made an official submission to the UN Commission, but declared that the Danish straits including the Great Belt, the Little Belt, and the Danish part of the Sound, formed on the foundation of the Copenhagen Treaty of 1857 are a legal part of the Danish regime. Additionally, Denmark is cooperating with Canada and maintains that the Lomonosov Ridge is in fact an extension of Greenland and the CAA, thus shelf extensions to the North Pole should be granted based on evidence.

Although the United States helped shape the Convention and its subsequent revisions, and though it signed the 1994 Agreement on Implementation, it has not ratified the UNCLOS treaty. On July 16, 2012, the U.S. Senate had 34 Republican Senators who have indicated their intention to vote against ratification of the treaty if it comes to a vote. Based on this discrepancy, the U.S. is not a signatory nation of UNCLOS and therefore is not currently part of the UN commission, which would have jurisdiction over debated rights to resources in regions such as the Arctic (Borgerson 2008).

Overall, warming temperatures, the decline in sea ice and the changing environmental landscape during the last decade has seen a new scramble for territory by

several coastal Arctic nations who are eager to exploit new shipping routes and potential resources. While diplomacy and cordial relationships have been sufficient to this point, increased access to natural resources as well as potential shipping and transit through territorially claimed waters will require the UN to adjudicate future disputes as tensions rise. There is also a general increase in activity and interest in the area by several non-Arctic nations including China, South Korea, Japan and countries of the European Union. The primary driver for many of the non-Arctic nations interest seems to be the potential for shorter and faster sea-lanes as well as possibility to lay claim to any of the untapped natural resources the retreat of Arctic sea ice may help expose.

C. U.S. STRATEGIC GUIDANCE

International interest concerning Arctic climate change and accessibility has grown in recent years as observations of warming temperatures, sea ice retreat and increasingly open ocean area in summertime have validated what had been studied and reported for decades by many scientists to include the Intergovernmental Panel on Climate Change (IPCC). The IPCC is an open consortium of scientists that periodically compiles a scientific report with the intent of building consensus on drivers of observed climate change in a peer-reviewed research environment. The IPCC is an international scientific body established by the United Nations Environment Programme (UNEP) and the World Meteorological Organization (WMO) in 1988 to report on the current state of knowledge on climate change and its potential environmental and socioeconomic impacts (IPCC 2012). The projected effects of climate change on Arctic sea ice outlined in the IPCC's 2007 AR4, in addition to many other studies, coupled with increased tensions between the Arctic nations, have seen the U.S. Government take affirmative action to ensure that they remain a key player in the region.

Since the Cold War concluded in the early 1990s, the U.S. interest in the Arctic, from a military perspective, has been on the decline as the former Soviet Union collapsed and the emerging Russian Federation has developed more cordial relations with the U.S. government. The U.S. has territorial claims to resources extending from its coast and has operated in the Arctic for scientific and military purposes in the past, but the U.S. has

lacked clearly defined guidance for the management of its interests in the region until beginning in 2007 with the release of A Cooperative Strategy for 21st Century Seapower. This joint publication, with contributions from the USN, United States Marine Corps (USMC) and United States Coast Guard (USCG), focuses on the importance of seapower as a unifying force and specifically identifies the Arctic as a potential source of competition and conflict for access to newly opening shipping lanes and undiscovered natural resources. This publication was the first in a series of strategic guidance documents that began to define the national security interests and objectives for U.S. diplomacy and potential operational capabilities in the Arctic.

Specific guidance establishing the policy of the U.S. with respect to the Arctic was set forth in 2009, when President George W. Bush signed the National Security Presidential Directive 66 (NSPD-66)/Homeland Security Presidential Directive 25 (HSPD-25). Along with its support to ratify UNCLOS, this presidential mandate established requirements for the U.S. to develop and maintain a greater capacity to protect sovereign interests extending from our boarders to the extent of the continental shelf, and to increase maritime domain awareness and global mobility through an enhanced ability to operate within the Arctic (Task Force Climate Change / Oceanographer of the Navy 2011). In May 2009, Task Force Climate Change (TFCC) was established, by the then Chief of Naval Operations (CNO), Admiral Gary Roughead, in an effort to address the impact of the environmental concerns outlined in the Presidential Directives on naval operations. TFCC is under the direction of the Oceanographer of the Navy and has been tasked with the initial goal to develop and implement strategic policy initiatives for the Arctic as well as a roadmap, for the Department of Defense (DoD), to navigate through global climate change responses (TFCC / Oceanographer of the Navy 2009). More specifically, TFCC is charged with making recommendations to Navy leadership regarding policy, strategy, force structure and investments relating to a changing Arctic (TFCC / Oceanographer of the Navy 2009).

The first actionable document produced by TFCC was the Navy Arctic Roadmap, in November 2009, which delineated a list of action items to address both the strategic and policy implications of changes in the Arctic, as well as provided a vehicle for the

Navy to assess and predict future environmental changes in the region. This roadmap outlined a strategic approach to determining the potential impact of rising sea levels, increased shipping activity, interest in natural resource exploration, research initiatives, migrations of fisheries, and eco-tourism into a more environmentally approachable Arctic. The opening of the NWP and NEP in 2008 as well as the overall increased shipping traffic in Arctic, alarmed the USN to the fact that the increased interest and operations in the region goes hand-in-hand with the potential for environmental disasters such as oil spills and increased search and rescue operations as unprepared ships encounter the fast-moving ice in the marginal ice zone (MIZ).

In addition to the presidential mandate, the 2010 Quadrennial Defense Review (QDR) identified climate change as one of several key geopolitical trends that may influence future conflict and again articulated strategic guidance on the Arctic, changing climate, and energy security. The QDR defined how climate change would affect the DoD in two broad ways:

1. Climate change will shape the operating environment, roles, and missions the U.S. undertakes.

2. The DoD will need to adjust to the impacts of climate change on facilities and military capabilities.

The impact of these changes has forced the Navy to assess its capabilities and identify shortcomings as a means of adapting to new battlefields and areas of interest in a new climate regime. Admiral Roughead defined the USNs desired end state as a safe, stable, and secure region where U.S. national and maritime interests are safeguarded and the homeland is protected through the Navy Strategic Objectives for the Arctic. This was in May 2010. This was the first deliverable from the Navy Arctic Roadmap, and specified the objectives required to achieve this end as:

1. Contribute to safety, stability, and security in the region.

2. Safeguard U.S. maritime interests in the region.

3. Protect the American people, our critical infrastructure, and key resources.

4. Strengthen existing and foster new cooperative relationships in the region.

5. Ensure Navy forces are capable and ready

Other guidance produced from TFCC include: the Navy Climate Change Roadmap in April 2010, which outlines the USNs approach to observing, predicting, and adapting to climate change; and the Arctic Environmental Assessment and Outlook Report in August 2011, which was the first biennial report providing a comprehensive assessment of the state of the Arctic environment including oceanography, hydrography, meteorology, fisheries, and ice-extent to include the projection that based on current scientific consensus, the Arctic may experience nearly ice free summers sometime in the 2030s.

D.   CURRENT U.S. CAPABILITIES

In 2011, the USN asked the War Gaming Department of the U.S. Naval War College to find out what the Navy needs to sustain operations in the Arctic. The 2011 Fleet Arctic Operations Game ensued and the results indicated that as a force, the USN lacks everything from bases and Arctic-capable ships to reliable communications and cold-weather clothing (Klauss, 2012). The findings were that the USN is not adequately prepared to conduct long-term maritime Arctic operations; Arctic weather conditions increase the risk of failure; and, most critically, to operate in the Arctic, the USN will need to lean on the USCG, countries like Russia or Canada, or tribal and industrial partners (Klauss, 2012).

A report to Congress in May 2011, entitled Arctic Operations and the Northwest Passage, described Arctic operations addressing strategic national security objectives, needed mission capabilities, an assessment of changing the Unified Command Plan (UCP), needed basing infrastructure, and the status of and need for icebreakers. Key challenges that were identified include: shortfalls in ice and weather reporting and forecasting; limitations in command, control, communications, computers, intelligence, surveillance, and reconnaissance (C4ISR) due to the lack of assets and harsh environmental conditions; limited inventory of ice capable vessels; and limited shore-based infrastructure.

Though the USN Commander, Naval Meteorology and Oceanography Command (CNMOC) has access to a collection of meteorological and oceanographic (METOC)

numerical models with domains covering the Arctic region, the dearth of METOC observations in the region are insufficient to support regular and accurate forecasting above or below the ocean surface. The USNs ability to report and forecast ice conditions in the Arctic region falls on the National/Naval Ice Center (NIC) in Suitland, Maryland which provides sea ice analysis and forecasting products primarily for the submarine fleet when they operate in the region, but has the ability to support any mission with operational analysis as well (DoD 2011). Shortcomings exist in the development of these products, partially due to the communication issues to this remote region, but also due to a lack of observational data coverage and fine-scale model physics, which are important for predicting sea ice growth, drift and melt. While the U.S. has begun to make investments into the collection of observational data in the Arctic, the dynamical processes of sea ice are more difficult to observe (O'Rourke 2011) than the ice extent or ice edge.

Communications are extremely limited due to magnetic and solar phenomena that degrade High-Frequency (HF) radio signals. Surface-based relays outside of Alaska are limited. High-data-rate satellite communications are sparse, but commercial low-rate service is available which is adequate for single ships, but the communications architecture is insufficient to support normal operational practices of a surface action group or any large-scale Joint Force operations (DoD 2011). Global Positioning System (GPS) performance is degraded at latitudes above 70°N due ionospheric effects, multipath interference, and orbital limitations of satellites (DoD 2011). The GPS performance may be adequate for surface navigation, but the degradations could affect missions that require precision navigation, such as weapons targeting or search and rescue (DoD 2011). Additionally, navigation charts are not up to modern standards as reported depths can be particularly unreliable in areas subject to shoaling and ice scour, increasing the risk for all littoral operations (DoD 2011). Although accurate ice coverage charts are available for surface navigation, reliable real-time ice characterization (e.g., depth or thickness) is not (DoD 2011).

Aircraft are capable of operating in the region, but are limited in range and duration due to a lack of airfields (Titley and St. John 2010). Naval air operations are

susceptible to equipment failure due to icing and heavy fog as ice and weather conditions limit ship maneuverability and increase the difficulty of the launch and recovery of aircraft on icy deck surfaces. In the submarine environment, aside from the avoidance of deep draft sea ice in regions of rafting ice and challenges surfacing in ice covered regions, the acoustic signature can change rapidly as surface water temperature and salinity profiles are altered through the freeze and melt cycle. This process makes acoustic forecast models difficult to predict and warming surface waters can greatly reduce the range of detection capabilities (TFCC 2011). The Arctic Submarine Laboratory (ASL) is the Navy's center of excellence for Arctic matters and is responsible for developing and maintaining expertise in the Arctic to include maneuverability and sound speed variability as well as supporting ICEX campaigns (DoD 2011).

Assured Arctic access to support national interests can be provided by a variety of proven capabilities, but only U.S.-flagged ice-capable ships provide visible U.S. sovereign maritime presence throughout the Arctic region (DoD 2011). "This need could potentially be met by either icebreakers or ice-strengthened surface vessels. U.S. Navy surface ships are not ice-strengthened and, therefore, are not available for employment in first year ice, or even in the marginal ice zone" (DoD 2011). The USN does participate in the joint Northern Edge exercise in the Gulf of Alaska during odd-numbered years and in 2009 brought the aircraft carrier John C. Stennis (CVN-74) as well as the USS Lake Erie (CG-70) and the destroyer USS Decatur (DDG-73), in 2011 (Klauss 2012).

The USCG possess three ships with icebreaking capabilities:

1.   The USCG Cutter (USCGC) HEALY (WAGB-20), which was commissioned in June 1999/ It is 420ft in length, and is in active condition as a medium polar icebreaker.

2.   The USCGC POLAR STAR (WAGB-10) and POLAR SEA (WAGB-11), which were commissioned in 1976 and 1978, respectively. Both of which are 399ft in length, and are both heavy icebreakers technically in active condition though both have had major overhauls and repairs as they are over 30 years old and may quickly be decommissioned.

This limited inventory spreads the USN and USCG very thin in terms of its ability to respond quickly to Search and Rescue and Humanitarian Assistance/Disaster Response

(HA/DR) missions that are likely to increase in the Arctic in the coming years. While requests have been made to Congress to augment this fleet by adding up to six heavy and four medium icebreakers to maintain the continuous presence requirements of the Naval Operations Concept, approval has so far been denied which places any augmentation out at least ten years (O'Rourke 2011).

Land-based support facilities are limited to various service bases in Alaska and Greenland (Figure 20), which leads to dependence on support from our partnership with Canada for use of their bases. The existing DoD infrastructure was described as, "adequate to meet near- to mid-term U.S. defense needs," and the need for the construction of a deep-draft port in Alaska between now and 2020 is not anticipated (DoD 2011). The closest deep-water ports are near Baffin Bay at the Air Force base in Thule, Greenland, and in the Aleutian Islands at Dutch Harbor, Alaska (Figure 20).
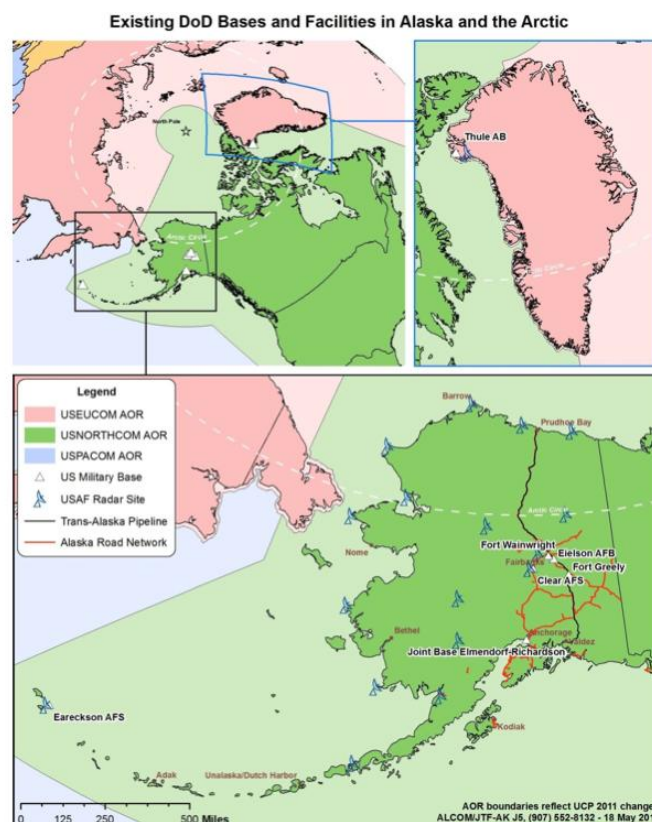
Figure 20.   Existing DoD Bases and Facilities in Alaska and the Arctic (From DoD, 2011)

The Navy Arctic Capabilities Based Assessment was published in September 2011, and identified capability gaps/shortfalls that may result should the USN need to conduct a set of mission areas in the Arctic between 2030 and 2040. The gaps identified consist of an inability in the Arctic to fully:

1. Provide environmental information
2. Maneuver safely on sea surface
3. Conduct training, exercise, education
4. Maneuver Safely in air
5. Sustain the force
6. Establish lines of communication
7. Provide reliable high data rate communication
8. Provide accurate navigation information
9. Maneuver safely or quickly on ground (including ice-covered ground)
10. Operate kinetic weapons
11. Collect required intelligence
12. Disrupt enemy weapon systems

Specifically addressing the first gap listed, to provide environmental information, the USNs desired effect would be "to provide METOC information within the same standards as those applied to traditional areas of responsibility (AORs), plus provide ice reports detailing position, thickness, movement, and expected short-term and long-term change" (Task Force Climate Change / Oceanographer of the Navy 2011b). The insufficient ability to provide METOC information, to include timely ice reports and accurate navigational charts, is not unique to the USN, but common to civilian and foreign militaries as well, due to underlying gaps in the collect, analyze, forecast, and exploit chain of events. Collection is hindered, as previously mentioned, due to a lack of observational posts in the region. Seasonal survivability of observational sensors contributes to this gap in collection as well as challenges in communications and data transfer from higher latitudes.

The NIC estimates future operational requirements as:

1. Forecasting ice location/movement expansion to 72 hours with 5 NM resolution supporting Optimum Track Ship-Routing (OTSR) and weather forecast operational support (Task Force Climate Change / Oceanographer of the Navy 2011b).

2. Forecasting ice location/movement expansion to 7 days for operational planning, 1–3 months, 1 year, and 5–10 years for longer range planning (Task Force Climate Change / Oceanographer of the Navy 2011b).

The harsh climate will necessitate information updates at the same frequency as other AORs. This typically requires 12-hours updates of OTSR information as well as warnings for both USN and non-USN players (Task Force Climate Change / Oceanographer of the Navy 2011b). Low activity in the Arctic has resulted in a lack of METOC personnel educated in the regime-specific knowledge required for collection, processing, analysis, and forecasting in the region (Task Force Climate Change / Oceanographer of the Navy 2011b). The gap of not being able to provide the necessary environmental information has major impacts particularly on the USN missions of the maintaining freedom of the seas, force protection, and maritime security.

The Navy Arctic Environmental Capabilities Based Assessment was published December 2011 (but not yet signed), specifically described gaps and shortfalls in environmental support to USN operations in the Arctic, to include observing, mapping and prediction capabilities. This document goes in to much greater detail of the first gap discussed in Task Force Climate Change / Oceanographer of the Navy (2011b) by breaking it into multiple inabilities, most specifically the inability to sense and forecast environmental parameters. Conclusions and recommendations of the document are based around development of interagency agreements, Arctic METOC concept of operations (CONOPS), interaction with indigenous people, increase visits and training for METOC support personnel, and increases in development and access to observational data, forecast models, and Arctic regional air/sea/ice dynamics education. This thesis hopes to address a small piece of the aforementioned capability gaps by providing research to better understand ice-ocean coupling that affects sea ice state and its variability. This

research is a small by necessary step toward an adequate arctic naval support infrastructure during a period of rapid environmental change in the region.

Overall, the USN arctic capability is extremely limited, but the capability gaps have been identified. Recommendations have been put forth addressing how the USN will overcome or cope with these gaps, but action is slow and constrained due to limited budgets and operational projections, which do not indicate a need for a USN presence until the middle part of the century. Maintaining the current timelines and budgetary restrictions will result in an increased reliance on the USCG and other interagency cooperation, as well as cooperation with our allies such as Canada, in any situation requiring a maritime presence in the Arctic. At present, the USN lacks the infrastructure, assets, manpower, and training to effectively operate in the Arctic.

THIS PAGE INTENTIONALLY LEFT BLANK

IV. THESIS MOTIVATION, DESCRIPTION OF THE NUMERICAL MODEL, AND RESEARCH METHODOLOGY

A. THESIS MOTIVATION

McPhee et al. (2005) is a study of a particular shearing event that occurred during the Surface Heat Budget of the Arctic (SHEBA) field campaign on March 19, 1998 (day 1998:78). The 1997–1998 SHEBA experiment was coordinated to address the interaction of the atmosphere, clouds, ice cover and the upper ocean in determining the energy balance in the Arctic including the ice albedo and cloud-radiation feedback mechanism. The centerpiece of the project was a scientific research station supported by icebreaker that drifted through an annual cycle in perennial sea ice in the Pacific sector of the Arctic Ocean north of Alaska (Uttal et al. 2002). The primary objective of SHEBA was to measure the energy components that determine the cycle of sea ice growth and decay and investigate the processes contributing sea ice variability. This was motivated by numerical climate simulations that show amplified response to climate warming in the Arctic (e.g., Rind et al. 1995).

During the shearing event discussed by McPhee et al. (2005), researchers had been measuring the response of the upper ocean to surface stress from wind forced ice motion in order to gauge the energy exchange between the ice cover and underlying ocean. This included measurements of velocity, temperature, salinity and turbulent fluxes at fixed levels in the ocean boundary layer (OBL), beneath the 2m thick pack ice, plus a profiling conductivity/temperature/depth (CTD) instrument. Basal heat flux from the ocean boundary layer to the ice undersurface was small, typically less than 5 W/m2, with the exception a few weeks in summer (Perovich and Elder 2002; McPhee et al. 2003). Bursts to as high as 30 W/m^2 were observed during storms. This was due to heat that was mixed upward by turbulence from below the well-mixed layer and pycnocline (McPhee et al. 2005).

On the afternoon of March 18, 1998, a significant ice shear event occurred near the camp causing the ice floe on the ship's starboard side to shift several hundred meters forward over the span of a few hours (McPhee et al. 2005). On March 19 "an intense

zone of pycnocline upwelling occurred on the order of ~14m (McPhee et al. 2005). Upward turbulent heat flux measurements in the OBL reached nearly 400 W/m^2 (McPhee et al. 2005). This was almost an order of magnitude greater than at any other time during SHEBA (McPhee et al. 2005). Figure 21 shows the turbulence measurements made at various depths during the event. A clear spike in the temperature, salinity and turbulent heat flux measurements is coincident with the time just after the intense shearing event.
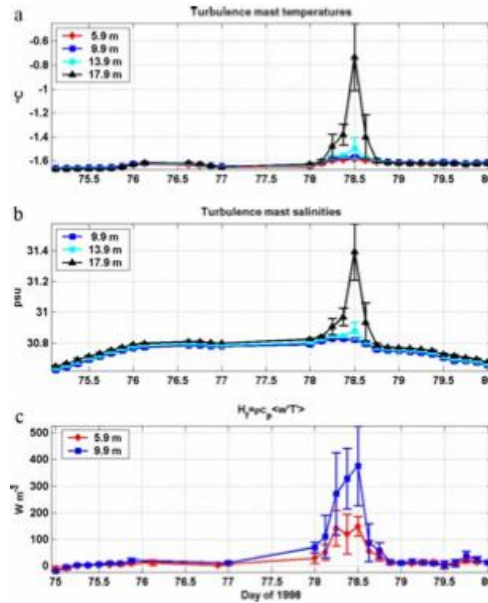
(a) Temperature (3-h averages) at fixed levels on the SHEBA turbulence mast. Error bars are twice the sample standard deviation.   (b) Salinity. Conductivity measurements at 5.9m were made with an open electrode microstructure instrument. (c) Turbulent heat flux from the covariance of temperature deviations and vertical velocity. Error bars are twice the standard deviation of the 15-min turbulence realizations in each 3-h average. On day 78, clusters at 13.9 and 17.9m were in the pycnocline where turbulence statistics were contaminated by internal waves

Figure 21.   Time series of turbulence mast temperature (top), salinity (middle), and heat flux (bottom) measurements at various depths through the day of the extreme shear deformation event (From McPhee et al. 2005)

Figure 22 shows the time series of T and S at fixed levels compared with CTD profiles at times bracketing the cycling profiler data gap and indicates an upwelling of relatively warm and saline pycnocline water on day 78. The temperature and salinity profiles indicated a larger displacement in the turbulence mast salinities than in the turbulence mast temperatures. This indicated a preferential upward mixing of heat relative to salt during the event (McPhee et al. 2005).
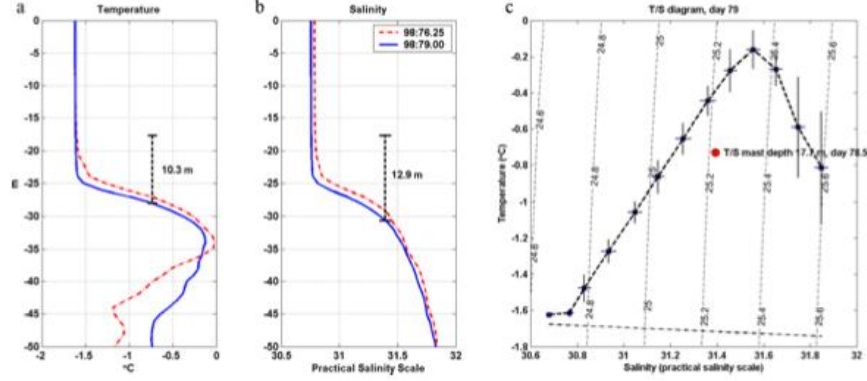
(a) Three-hour average temperature and (b) salinity profiles bracketing the period when the SHEBA profiling CTD was down for lack of ship power. Dashed vertical lines represent displacements of the isotherm and isohaline levels to the values observed at 17.9m at time 78.5 (from previous figure) (c) Average temperature/salinity characteristics from all CTD profiles on day 79. Dashed curves are potential density minus 1000 in kg/m^3. The solid circle shows T/S properties at 17.9m at time day 78.5

Figure 22. Temperature (left) and salinity (middle) profiles indicating displacement due to the shear event. Average temperature and salinity measurements (right) from all CTD profiles on the day of the event. (From McPhee et al. 2005).

A mechanism known as Ekman pumping induces vertical motion at the ocean surface layer due to the horizontal shear in sea ice velocity (McPhee et al. 2005). An approximation of the vertical velocity at the base of the boundary layer obtained by integrating the steady-state momentum equation from there to the ice/water cover (Gill, 1982):

$$w_p - w_0 \approx \frac{1}{f}\nabla \times \tau_0 \qquad (4)$$

Where $w_p - w_0$ is the velocity relative to the surface of an isopycnal surface just below the turbulent boundary layer; f is the Coriolis parameter; and the $\nabla \times \tau_0$ is the curl of the kinematic stress at the ice/ocean interface (McPhee et al. 2005). The p represents the vertical velocity at the base of the boundary layer while the 0 represents the top. This results from satisfying continuity when there is a gradient in Ekman transport in the turbulent boundary layer, where the transport is typically almost perpendicular to the interfacial stress (McPhee and Smith 1976). Upwelling of the pycnocline follows if the stress curl is positive (McPhee et al. 2005). The upwelling is induced by a counterclockwise rotation in the ice velocity field relative to the underlying ocean (McPhee et al. 2005).

65

RGPS was used to analyze a comprehensive view of the ice motion field in region surrounding the ship. Figure 23a shows the velocity field derived from tracking two RGPS scenes spanning the period 1998:77.75 to 78.73. During the an event on day 78, there was significant horizontal shear in the north-south direction and backing in ice drift direction going from west to east. Figure 23b shows the kinematic ice/ocean stress, ($\tau_0 = |u_{*0}|u_{*0}$ where u_{*0} is frictional velocity at the interface) was calculated as a function of ice velocity relative to underlying geostrophic ocean current by considering planetary boundary layer similarity and data relating ice velocity to various measures of ice/ocean stress (McPhee 1990, McPhee et al. 2003). The stress curl analysis (Figure 23b) shows that of the zone of moderate to intense shear extended for at least 200km in a clearly identifiable arc from southeast to northwest (McPhee et al. 2005). The RGPS image in Figure 23c shows consistency in the observations indicating that the shear deformation event did take place (McPhee et al. 2005). This mechanism for concentrating gradients in Ekman transport across very small horizontal scales seems unique to ice-covered oceans.
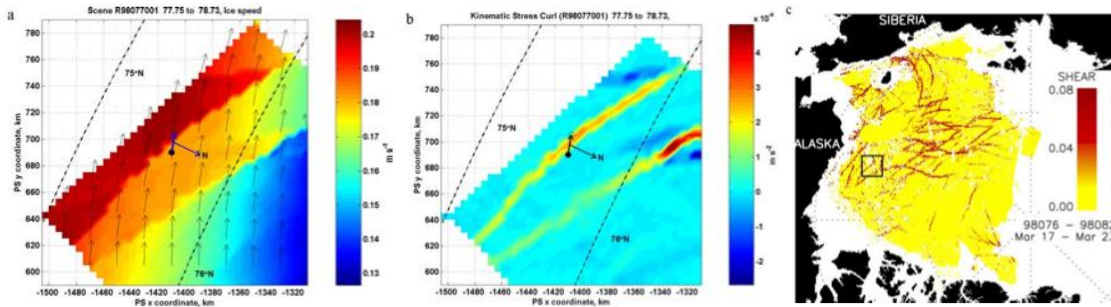
(a) Average velocity field from RGPS features tracking in scenes separated by about one day. Circles show the beginning (solid) and ending (open) positions of the SHEBA drift station. Shading indicates ice speed; vectors show velocity at every 4th grid point. (b) Finite approximation of the kinematic ice/ocean stress curl derived from the velocity field with a grid space of 5km. (c) Basin wide depiction of the ice velocity shear from sequential SAR images for the week of Mar 17–23, 1998. Outlines box indicates the domain of previous analysis

Figure 23.   Average velocity field from RGPS (left), kinematic ice/ocean stress curl from velocity field (middle), and basin wide RGPS image (right) (From McPhee et al. 2005).

It was suggested that changes in surface velocity and surface stress over the open ocean reflect the scale of the forcing atmospheric pressure fields, whereas the mechanical properties of sea ice apparently localize these differences into relatively intense zones of

66

surface vorticity (closely related to stress curl) (McPhee et al. 2005). This means that the ice cover concentrates gradients in the forcing wind field into narrow bands of intense shear, which can induce major shifts in the elevation of the pycnocline, or equivalently the thickness of the well-mixed surface layer. Measurements from the turbulence mast and ice thickness indicated that these intense shear deformation events could enhance heat transfer from below the mixed layer and contribute to significant basal melt during the winter months when ice column is approaching its lowest temperatures and actually growing. (McPhee et al. 2005). Locally, these LKFs may induce longer-lived pycnocline circulations, and contribute to basal melt throughout the winter. As indicated by the RGPS data, LKFs can be relatively long and commonly occurring, thus a grand summation over an entire winter could contribute to considerable melt/lack of growth for a larger region. While other studies have found that the ice-ocean albedo feedback, lateral advection and mesoscale eddies contribute to basal melt (e.g., Shimada et al. 2006; Timmermans et al. 2007; Perovich et al. 2008; Maslowski and Clement Kinney 2010; Haynes 2012), this may be yet another mechanism not heretofore considered.

Only a single strong shear deformation event, such as what was described in McPhee et al. (2005), has been observed so far to our knowledge. A numerical model is best suited to evaluate how common and how important these events are to Arctic sea ice variability. The research questions posed are as follows:

1. Is a numerical model capable of representing the proposed dynamics and ice/ocean-coupling relationship for deformation induced upwelling?

2. What is the statistical prevalence of these events and their overall effect on the ice pack?

B. REGIONAL ARCTIC SYSTEM MODEL (RASM) DESCRIPTION

Various scientific reports (e.g., Arctic Observing Network 2010; Roberts et al. 2010) have called for the establishment of a community based Arctic regional climate model, adopting a similar development approach a the global NCAR Community Climate System Model (CCSM) or Weather Research and Forecasting (WRF) model. These models have been developed by involving a broad spectrum of the international scientific community, with centralized scientific governance. Roberts et al. (2010) explained that

the physical, chemical, biological, and social components of the Arctic System are interrelated, and therefore a holistic perspective is needed to understand and quantify their connections and predict future changes. Regional atmospheric and ice-ocean models have been developed, however, they have limits in addressing the operation of the fully coupled Arctic Climate System. Feedbacks between the air, ocean, and ice are sometimes not accounted for due to lower boundary conditions prescribed by atmospheric forcing (Rinke et al. 2006; Maslowski et al. 2004; Roberts et al. 2010). Additionally, some GCMs that are configured at coarse resolutions and/or utilize crude parameterizations to represent physical processes may not adequately describe past sea ice variability or be able to project future sea ice conditions (Maslowski et al. 2007; Roberts et al. 2010). Thus, a high-resolution regional Arctic system model including state-of-the-art land, atmosphere, sea ice, and ocean components is needed to address the described deficiencies (Roberts et al. 2010).

The evaluation of previously mentioned high-resolution NPS models, such as NAME, has shown improvements in the seasonal cycle of sea ice edge, thickness, and volume fluctuations (Maslowski et al. 2007; Clement et al. 2005; McGeehan and Maslowski 2011). Melt rates from these model results (Maslowski et al. 2007) compare well with recent observational data (Kwok and Cunningham, 2008; Kwok et al., 2009), which suggest that near ice-free summers in the Artic may occur in the near future (Maslowski et al. 2012). These results provide further motivation to utilize the advanced coupling mechanism of a high-resolution regional Arctic climate model to more accurately represent entire Arctic climate system, from a holistic approach, that may influence future climate predictions.

The Regional Arctic System Model (RASM) is a fully-coupled land/ice sheet, atmosphere, sea ice, and ocean model developed to address deficiencies in and provide guidance to GCMs in representing climate change in the Arctic (Maslowski et al. 2012). RASM was initiated with the support from the Department of Energy Climate Change Prediction Program with additional funding from the National Science Foundation Office of Polar Programs and the Office of Naval Research. The focus of the RASM modeling effort has been to improve the realism in representing critical small-scale processes and

pan-Arctic climate dynamics, and to test new physical parameterizations, which will help guide future observational requirements.

RASM contains updated regional versions of the Los Alamos National Laboratory Parallel Ocean Program (POP) and sea ice (CICE) models described in Smith et al. 2010 and Hunke and Lipscomb (2010), respectively. RASM incorporates a version of the NCAR WRF atmospheric model (Skamarock et al. 2008) that has been optimized for polar regions (Higgins et al. 2012). The Variable Infiltration Capacity (VIC) model (Cherkauer et al. 2003; Andreadis et al. 2009; Bowling and Lettanmaier 2010) represents land hydrology in RASM. Each of these models communicates mass, momentum and energy fluxes through a coupler, CPL7, which is used in the NCAR CCSM model (Craig 2012). All climate system components within this model are fully coupled so that changes made in one field impact and are responded to by every other field through feedback mechanisms. In future versions, the Community Ice Sheet Model (CISM; http://oceans11.lanl.gov/trac/CISM) will represent ice sheet components.
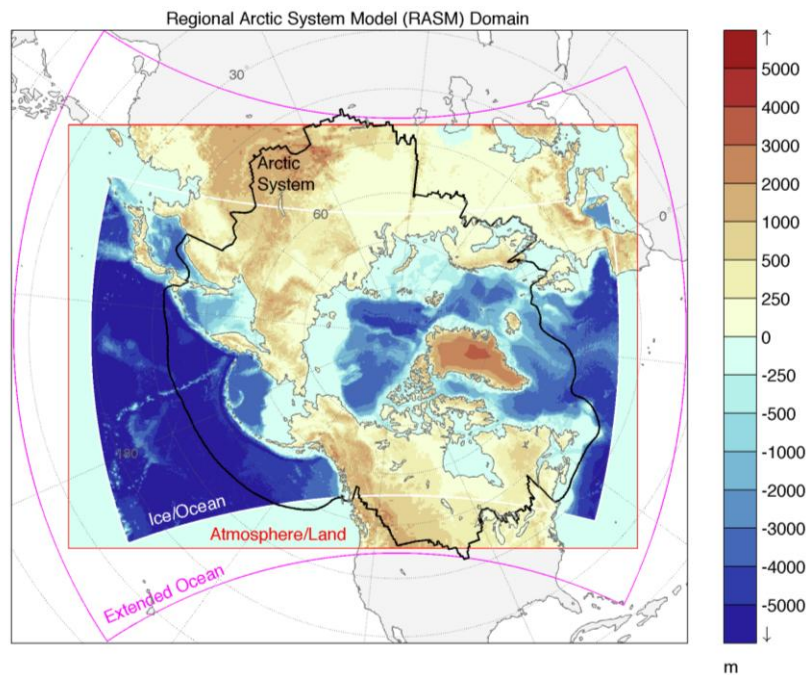
Figure 24.   Regional Arctic System Model (RASM) pan-Arctic model domain. WRF and VIC model domains include the entire colored region. POP and CICE domains are bound by the inner red rectangle. Arctic System domain is bound by the black line. (Courtesy A. Roberts 2012).

The RASM model domain encompasses the entire pan-Arctic region (Figure 24). The active ocean and ice domains incorporate the Seas of Japan and Okhotsk in the west, the sub-Arctic North Pacific and North Atlantic Oceans, the CAA, and the Nordic Seas in the east. This domain includes all major oceanic inflow and outflow regions of the Arctic Ocean, and all of the seasonally ice-covered seas in the Northern Hemisphere. The atmosphere and land models are extended to include all terrestrial drainage basins that bring freshwater to the Arctic (Maslowski et al. 2012). The ocean and sea ice models use a horizontal grid spacing of $1/12^{o}$ (~9km) while the 35-level atmosphere model and surface hydrology use a horizontal grid spacing of 50km. The ocean model has 45 depth layers (detailed in Appendix C) while the sea ice model has five ice thickness categories with thickness boundaries: 0–0.64m-1.39m-2.47m-4.56m-9.33m. Sea ice may vary in thickness within the bounds of each category following the method of Lipscomb (2001). The ocean and sea ice models are coupled with the atmosphere and land every 20 minutes, although the time steps within each model differ: WRF uses a 2.5 minute time step and VIC uses a 20 minute step. Most important to this thesis is that for the model runs analyzed, POP used two 8-minute leapfrog steps and 4-minute one forward step within each interval CICE uses a 20-minute thermodynamic step with 4 5-minute dynamic sub-cycles to solve equation (1). It is important to note that the ocean time stepping procedure, while necessary for RASM coupling, can result in a diffusive solution, but that the higher number of dynamic sea ice time steps better converge the pack to plasticity (Hunke and Dukowicz, 1997). For the purposes of this study a base model output with temporal resolution of one hour is used. Additional details about the RASM model are provided in Maslowski et al. (2012).

C. RESEARCH METHODOLOGY

The RASM output time sets selected for analysis were chosen based on an initial evaluation of sea ice deformation occurrences over the Beaufort Sea in the western Arctic north of the Alaskan coast. This region of the Arctic was selected because, first, LKFs are frequently observed in this area, as previously mentioned in Chapter II. Second, this portion of the Arctic Ocean includes U.S. sovereign territory and is of security and operational interest to the USN. Sea ice deformations averaged over one month, through

the 1990s, were first evaluated to narrow down months of interests. The winter months of December, January, February, and March were specifically selected in order to evaluate the effect of sea ice deformations on the upper ocean throughout the winter when the only source of heat is trapped beneath the mixed layer stratification depth. The sea ice deformations for the selected months were then analyzed over a temporal scale of one day to confirm the frequency of deformation events. The following model cases were selected for analyses with model output at a one-hour time resolution:

Table 1.   Model Cases

MODEL CASE NAME	TIME SPAN
r30TOM1	January - February 1990
r30TOM2	December 1990
r30TOM3	January 1991
r30TOM4	March 1992
r30TOM6	December 1995 - March 1996

The output summary, restarted with the r30RB1g configuration, per model was as follows:

POP (Ocean model)

Depth Layers: 1:20 (down to 528m in depth)

Longitudinal Grid Cells: 460:820

Latitudinal Grid Cells: 160:580

Ocean Variables: u-component ocean velocity, v-component ocean velocity, temperature, salinity, sea surface height, and sensible heat flux

CICE (Ice Model)

Longitudinal Grid Cells: 460:820

Latitudinal Grid Cells: 160:580

Ice Variables: u-component ice velocity, v-component ice velocity, bottom melt, thickness, and concentration

CPL7 (Coupler)

Across the entire atmospheric domain

Note: The POP/CICE output is for a subdomain and CPL7 is a global domain because the atmosphere and land-component models use a horizontal grid spacing of 50 km in order to allow for global scale circulation patterns to most accurately influence the Arctic subdomain.

Coupler Variables: sea level pressure, latent heat flux, sensible heat flux, u-component atmospheric velocity, and v-component atmospheric velocity,

In order to answer the first research question, the RASM u- and v-components of the sea ice velocity field were used to calculate the three invariants from the velocity gradients formed by moving ice fields. The first was divergence, which is a measure of the rate of area change of the ice (i.e., opening / closing of sea ice cover per unit area). The second was vorticity, which is a measure of the rotation rate. The third was shear, which is a scalar measure of the relative deformation of adjacent surfaces (Kwok 2006). These invariants were calculated by the following equations (Kwok 2001; Lindsay and Stern 2003; Kwok et al. 2008):

$$Divergence = \dot{\varepsilon}_{div} = \frac{\partial u}{\partial x} + \frac{\partial v}{\partial y} \tag{5}$$

$$Vorticity = \dot{\varepsilon}_{vor} = \frac{\partial v}{\partial x} - \frac{\partial u}{\partial y} \tag{6}$$

$$Max \cdot Shear = \dot{\varepsilon}_{shear} = \left[\left(\frac{\partial u}{\partial x} - \frac{\partial v}{\partial y} \right)^2 + \left(\frac{\partial u}{\partial y} + \frac{\partial v}{\partial x} \right)^2 \right]^{1/2} \tag{7}$$

The deformations (vorticity, divergence, and shear) were calculated and four quadrant plots of the SLP, vorticity, shear and divergence were generated and overlaid with the ice drift direction to systematically analyze events in a plane view projection.

Utilizing the one-hour temporal resolution, animations were made for each output set, in order to identify specific events and exploit the extremely fine scale nature of sea ice deformations. RASM output was converted into time series for each grid point within the Beaufort Sea region, north of the Alaskan Coast, in order to simultaneously compare the time evolution of multiple variables to variations in the total deformation rate. Time series could only be generated for individual grid points, thus the Beaufort Sea was divided into three square-boxes (Figure 25) in order to cover as much of the ocean surface as possible while not including areas close to the coastline and the MIZ. Grid points with sea ice concentration of 85% or higher were only considered. Time series comparisons were generated for each of these grid cells within the three boxes for the ocean temperatures down to 10 layers of depth (2.5m - 73.1m), the basal melt rate, sea ice shear, sea ice divergence the total deformation rate, as well as the ice-ocean stress curl. Identification of a disturbance in the upper ocean temperature structure coincident with a noticeable shear deformation event and the correct sign of the ice ocean stress curl would be considered a positive identification of an upper ocean response due to deformation within the sea ice. Events with a positive identification were then furthered analyzed to look at the timing of the disturbances and events in order to directly attributed causality and response.

Though many case studies were identified throughout the analysis of several RASM output sets this thesis focuses on primarily three case studies from the r30TOM6 output set which spans from December 1, 2005 through March 31, 2006. These three case studies and the approximate location of the grid points analyzed for each investigation color coded red for Case Study A, blue for Case Study B, and green for Case Study C as seen in Figure 25. The deformation events identified in the Case Studies spanned several grid points within each respective grid box as indicated in Figure 25. Due to the similarity of results, the time series of only one grid point for each case study is presented here,

73
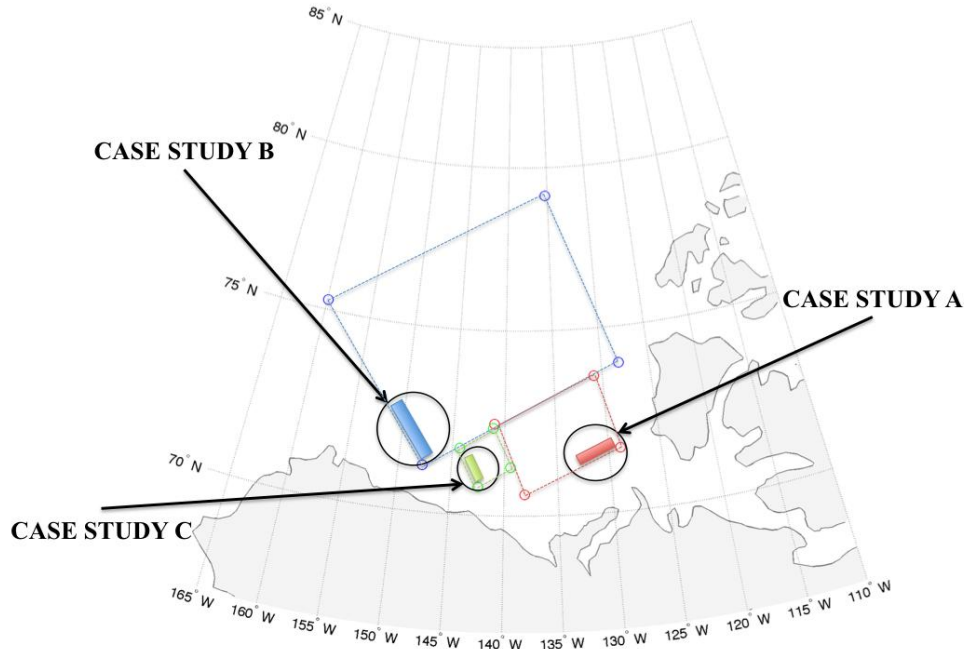
Figure 25. Beaufort Sea grid box division and approximate location of the grid points used in the individual case studies that are labeled.

To answer the second research question a broad statistical analysis was performed. The spatial characterization of the total sea ice deformation rate was first investigated as an independent verification of Marsan et al. (2004), Girard et al. (2009), Stern and Lindsay (2009), and Hutchings et al. (2010). This involved calculating the sea ice deformation rate at various spatial scales to analyze the rate of change of the total sea ice deformation. The total deformation rate within sea ice is derived from strain rates caused by spatial variability in the ice motion fields (Lindsay and Stern 2003). The total strain rate or total deformation rate is defined by the following equation:

$$Deformation \cdot Rate = \dot{\varepsilon}_{tot} = \sqrt{\dot{\varepsilon}_{div}^2 + \dot{\varepsilon}_{shear}^2}$$

(8)

It should be noted that this scalar quantity contains information about the intensity of the strain rate, whereas the information about the principal directions is lost (Girard et al. 2009).

74

This calculation was done for all grid points in the Beaufort Sea region with an ice concentration greater than 85% at scale bins starting at 9km and increasing by 9km in each bin up to 99km (9, 18, 27, 36, 45, 54, 63, 72, 81, 90, and 99km). Going from the default RASM output of $(9km)^2$ to $(18km)^2$ required averaging four grid points together for an $(18km)^2$ grid value. Nine grid points were required for the $(27km)^2$ metric and so on up to $(99km)^2$. Figure 21 describes examples of the $(18km)^2$, $(45km)^2$, and $(90km)^2$ sampling metrics used in the spatial characterization analysis. These calculations were then used to develop scatter plots, in log space, comparing the total deformation rate across scale lengths.
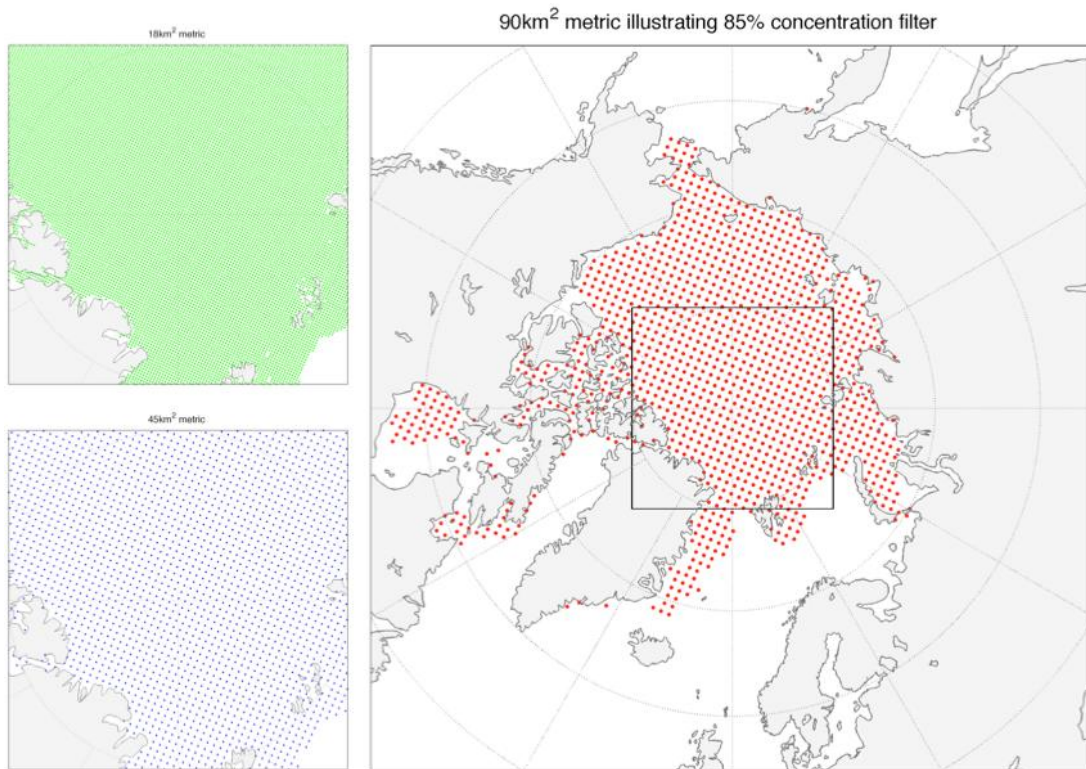
Figure 26.   Examples of the $(18km)^2$, $(45km)^2$, and $(90km)^2$ sampling metrics used in the spatial characterization analysis (Courtesy of Dr. Andrew Roberts)

In addition to the model verification of the total sea ice deformation rate, the analysis was taken a step further and the total deformation rate was calculated by averaging across different time scales from one hour, 3 days, 6 days, and 30 days,

respectively. This allowed for a temporal characterization as well. This same process of spatial and temporal characterization was done for the basal melt rate as well.

Finally, the power spectra and coherence were calculated for a final analysis of the relationship between sea ice deformation events and basal melt. Commonalities in spectral energy at a particular frequency band and the strength of association between several time series variables where the possible dependence between two series may not be limited to simultaneous values, but may include leading, lagged and smoothed relationships was investigated.

D.   MATLAB ICEPACK TOOLBOX

Model analysis was conducted with the aid of a purpose-built MATLAB toolbox for RASM being developed within the Naval Postgraduate School Polar Oceanography and Climate Laboratory. This software allowed easy graphical analysis of RASM netCDF output, and statistical analysis of RASM time series. Research conducted as part of this thesis helped to improve this software, and in some case, create new utilities where the existing capability was lacking. While most of the techniques employed to analyze the model have been described above, I detail here the method used to construct power spectra densities within this toolbox.

Where Power Spectral Densities (PSDs) were calculated in Chapter V, all time series with hourly samples from different model components were synchronized by linearly interpolating to the precise hour, since some output from CICE, for example, is output at 20 minutes past the hour for internal RASM timekeeping reasons. Once synchronized, PSDs were constructed for individual time series using Welch's method. To do this, we divided each real-valued time series into short non-overlapping hamming-weighted windows, applied a Fourier transform, multiplied by its conjugate, and averaged across these windows and along the line of PSD symmetry arrive at a one-sided PSD. For the PSDs provided in Chapter V, we used window sizes of 95 hourly samples, meaning that each PSD had degrees of freedom for a one-sided PSD of $V = 2 \times 2.5164 \times N / 95$ where N is the total number of samples in each time series, following Priestley (1981).

This allows easy calculation of the 95% confidence interval shown in subsequent figures following Emery and Thomson (2004).

Cross coherence squared between two synchronized and equal length time series, designated a and b, can be estimated as the ratio $PSD^2_{a,b} / (PSD_{a,a} * PSD_{b,b})$ where double subscripts indicate a PSD calculated for a single time series as described in the previous paragraph, and mixed subscripts indicate that the conjugate of Fourier transform b is multiplied by the transform of a, which is a cross spectra. This method follows the procedure outlined in Emery and Thomson (2004), which allows the confidence interval to determine the coherence value beneath which any coherence between two time series may be random for V degrees of freedom. Cross coherence squared is, in effect, a way of determining the degree of correlation between different time series in any given frequency band, and this method is employed for this purpose in Chapter V.

THIS PAGE INTENTIONALLY LEFT BLANK

V. RESULTS AND DISCUSSION

In this chapter, primary results of the evaluation of sea ice deformation and its spatial characterization from the Regional Arctic System Model (RASM) are analyzed and compared with other observational studies. Discussion of these results is also presented in this chapter. Additional results from preliminary investigations can be found in Appendix A: Model Domain, Sea Ice Deformation Analysis Calculations and Examples and Appendix B: Initial Sea Ice Deformation and Upper Ocean Response Case Study Results.

A. QUESTION #1: IS RASM CAPABLE OF REPRESENTING THE PROPOSED DYNAMICS AND ICE/OCEAN COUPLING RELATIONSHIP FOR DEFORMATION INDUCED UPWELLING?

Four still frames from December 30, 2005, through January 2, 2006, resulting from analysis of the ice drift field overlaid with the atmospheric SLP, calculated sea ice vorticity, shear, and divergence are shown in Figure 27. The red dot indicates the approximate location of grid point (205,40) in Case Study A. The blue dot indicates the approximate location of grid point (140,68) in Case Study B. The green dot indicates the approximate location of grid point (155,50) in Case Study C. During that time, a well-developed pressure systems moves through the region and generates a strong sea ice deformation response. The still frames do not show the more classic clearly defined LKFs as a result of the deformation but, more a larger widespread disturbance across the pack indicating intense large scale atmospheric forcing. The SLP pressure gradient remains closely packed through the time frame and dissipate toward the end January 2. The following case studies all positively identified extreme shear deformation events, which resulted in an upper ocean response during this time period.
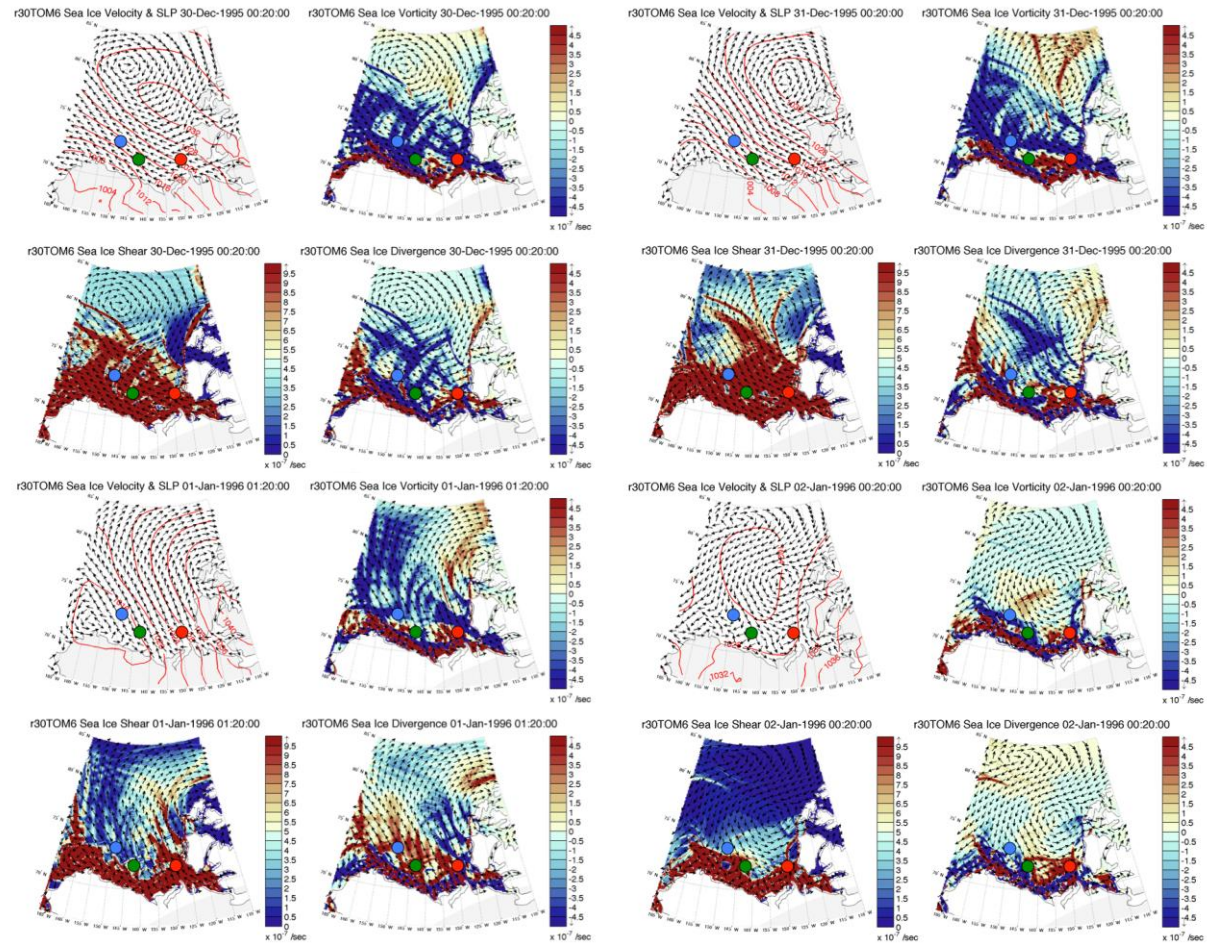
Figure 27. Four still frames from December 30, 2005 through January 2, 2006 (from top left to bottom right) of the map projection analysis of the ice drift field, only direction not magnitude, overlaid with the atmospheric SLP (upper left), calculated vorticity (upper right), shear (lower left), and divergence (lower right). The red dot indicates the approximate location of grid point (205,40) in Case Study A. The blue dot indicates the approximate location of grid point (140,68) in Case Study B. The green dot indicates the approximate location of grid point (155,50) in Case Study C.

1. **Case Study A: Grid Point (205,40)**

Figure 28 depicts a comparison of the time series spanning from DEC95–MAR96. The top time series represents the ocean temperature structure from 2.5m to 73.1m depth. The top-middle time series represents the basal melt rate. The bottom-middle time series represents the sea ice shear, divergence and total deformation rate of sea ice. The bottom time series represents the ice-ocean stress curl. All of the figures indicate little activity or change throughout the winter months with exception of a disturbance beginning in the middle of December and lasting through the middle of January. At first glance there appears to be a disturbance in the ocean potential temperature profile along with dominant peaks in basal melt rate as well as the sea ice deformation and ice-ocean stress curl.

Figure 29 depicts a zoomed in or cropped version of Figure 28 in order to focus in on this aforementioned disturbance in the time series. The black oval indicates the event of interest. By taking a closer look this event is even more pronounced. The ocean temperature structure shows the temperatures at 2.5, 7.5, 12.5, 17.5, 23, and 30m depths converging at a "median" temperature. The water temperature rises at depths of 2.5, 7.5, 12.5, 17.5, and 23m while it drops at 30m. This structure indicates the water column has become well mixed while the temperature indicates that warmer water has been introduced into the column from below the stratification depth. This explains the convergence of the temperature at the various depths. The spike in the basal melt rate further supports the argument that the temperature in the water column of the upper ocean has increased. The basal melt rate reaches ~5 cm/day, which is fairly substantial especially when compared with the values of the full the time series. Additionally, the positive ice-ocean stress curl coincident with the strong shear deformation spike indicates upwelling of the pycnocline will follow as induced by the counterclockwise rotation in the ice velocity field relative to the underlying ocean in the northern hemisphere (right hand rule). Overall, these model results indicate that a shear deformation event, with a positive ice-ocean stress curl, has induced a response in the upper ocean such that warmer water was upwelled into the mixed layer from below resulting in its overall warming and subsequent increases in the basal melt rate of sea ice.

In order to more directly compare the timing of these events and the resulting disturbances through causality and response, the cropped time series were overlaid on one another in the same plot. Figure 30 depicts an overlay of the basal melt rate and the ice-ocean stress curl. The black oval again indicates the event of interest. There is a clearly defined spike coincident with both variables where the basal melt rate increases to ~5 cm/day. This supports the conclusion of a tight ice/ocean coupling relationship. Figure 31 depicts an overlay of the total deformation rate and the basal melt rate. Again a similar coincident spike is clearly defined. This again shows the tight coupling at the ice/ocean interface. Figure 32 depicts an overlay of the ocean potential temperature structure and the total deformation rate. Again, there is a spike in the total deformation rate coincident with warming of the ocean structure. This warming is on the order of the ~0.5^{o} as the temperature is raised from -1.8^{o} (which is approximately at freezing) to -1.3^{o} which is below freezing and thus causing melt. The evidence that there was a strong shear deformation event with a positive ice-ocean stress curl coincident with the warming and mixing of the upper ocean resulting in an increase in the basal melt rate supports the conclusion that there is a tight coupling relationship between the ice and ocean and that the hypothesized dynamics and events do occur in the model.

CASE STUDY A: GRID POINT (205,40)
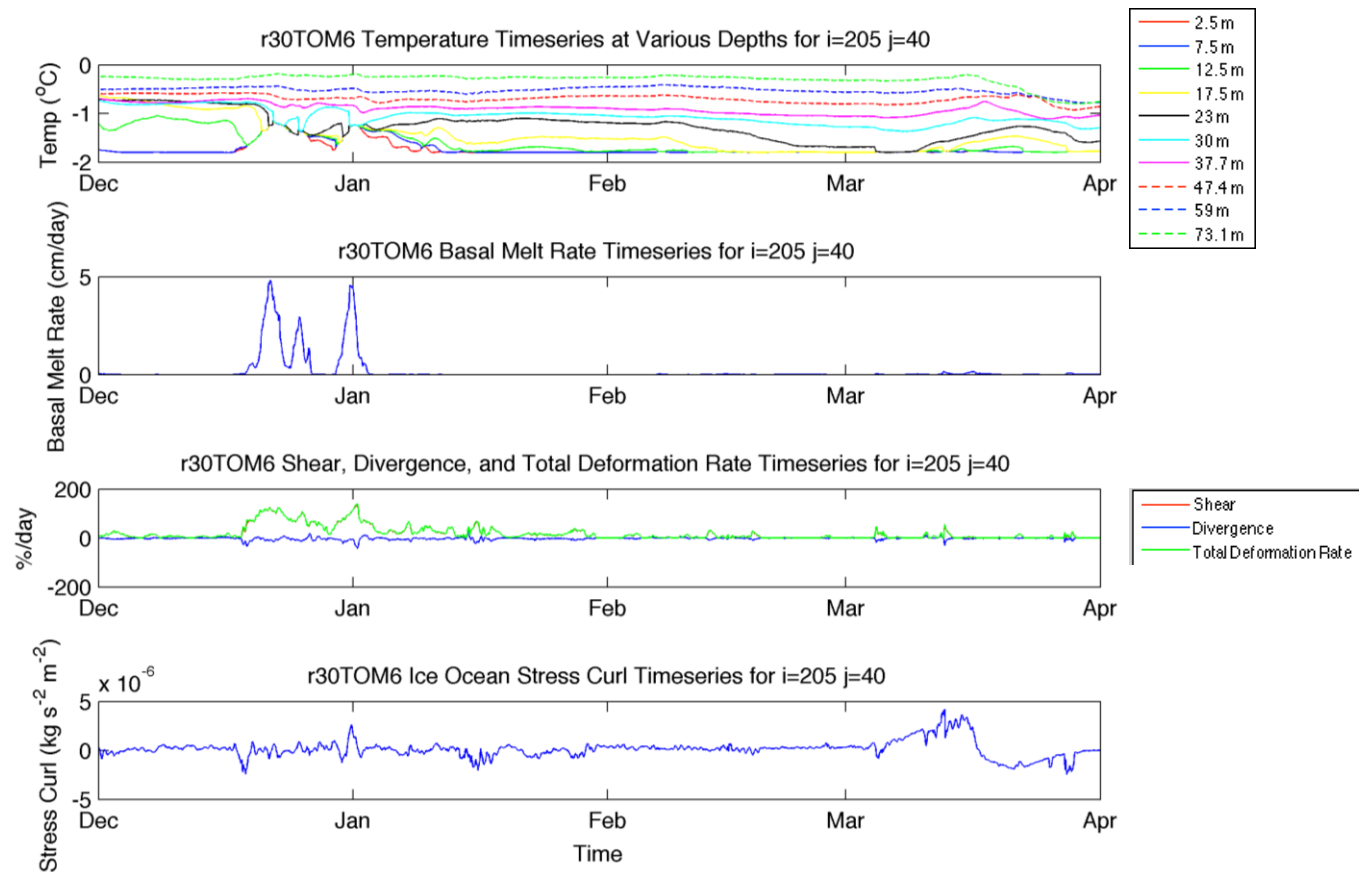
Figure 28.   Time series (DEC95-MAR96) comparison for grid point (205,40). (Top) Shows the time series for the top 10 layers of the ocean (2.5m–73.1m). (Top Middle) Shows the time series of the basal melt rate. (Bottom Middle) Shows the time series of the shear, divergence and total deformation rate. (Bottom) Shows the time series for the Ice-Ocean stress curl.

CASE STUDY A: GRID POINT (205,40)
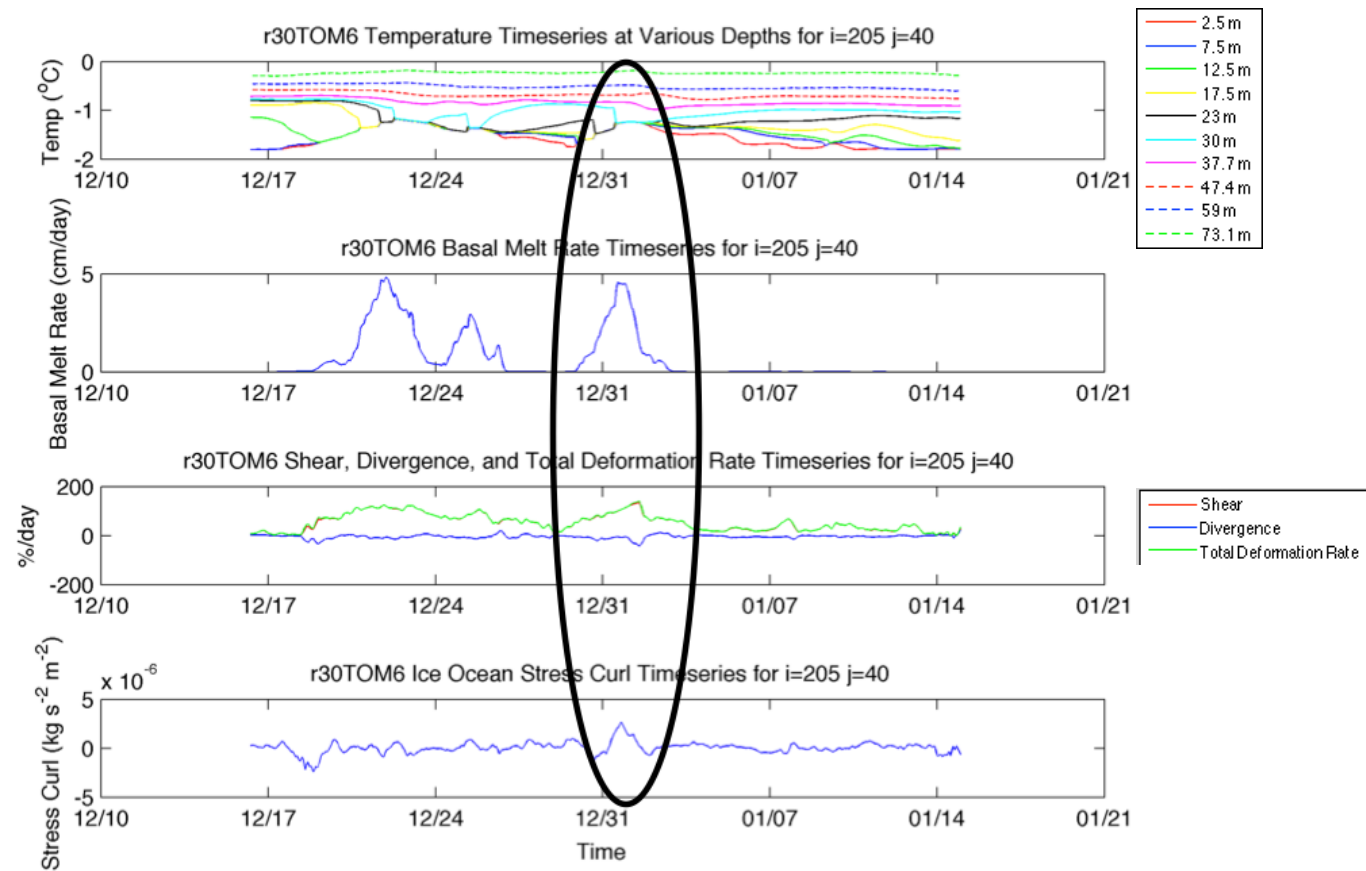
Figure 29. Zoomed in time series (15DEC95 -15JAN96) comparison for grid point (205,40). (Top) Shows the time series for the top 10 layers of the ocean (2.5m–73.1m). (Top Middle) Shows the time series of the basal melt rate. (Bottom Middle) Shows the time series of the shear, divergence and total deformation rate. (Bottom) Shows the time series for the Ice-Ocean stress curl. Black oval indicates the event of interest.

Figure 30. Zoomed in basal melt rate and ice-ocean stress curl time series overlay (15DEC95–15JAN96). Black oval indicates the event of interest.

Figure 31.   Zoomed in total deformation rate and basal melt rate time series overlay (15DEC95–15JAN96). Black oval indicates the event of interest.

CASE STUDY A: GRID POINT (205,40)
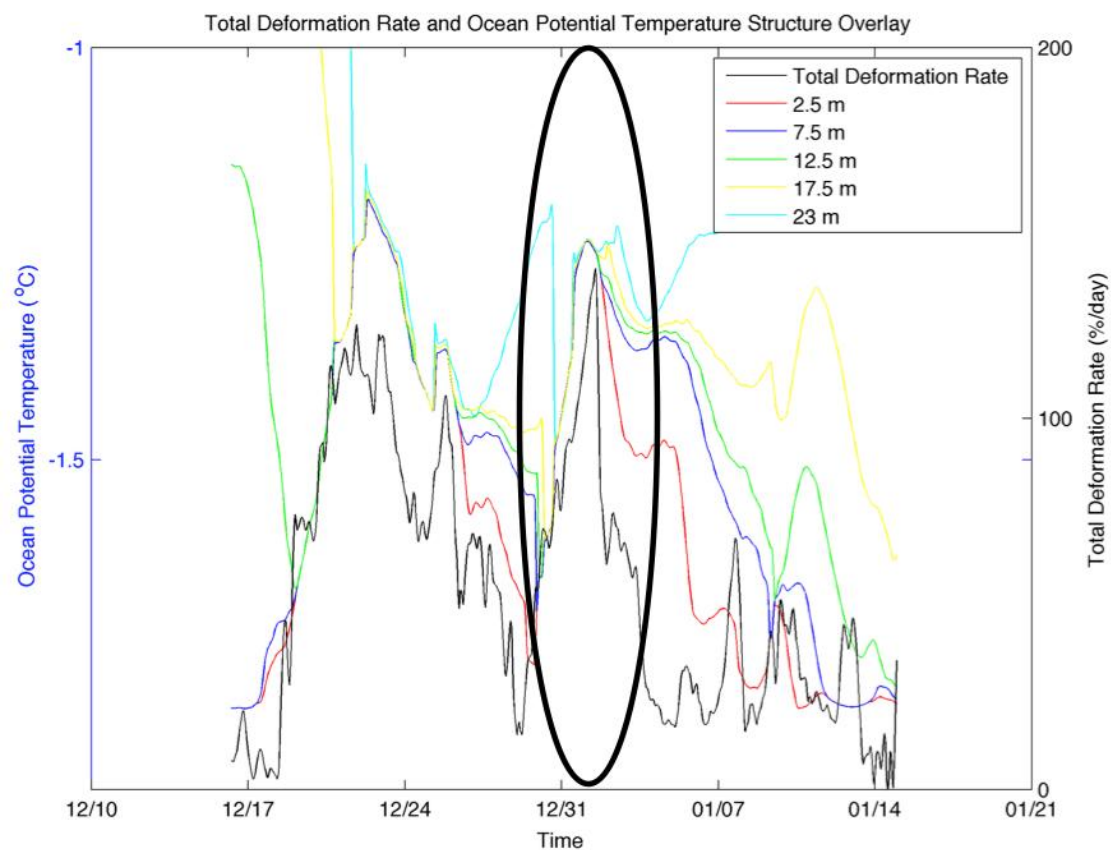
Figure 32.   Zoomed in total deformation rate and ocean potential temperature time series overlay (15DEC95–15JAN96). Black oval indicates the event of interest.

2.   Case Study B: Grid Point (140,68)

Figure 33 depicts a comparison of the time series spanning from DEC95–MAR96. The top time series represents the ocean temperature structure from 2.5m to 73.1m depth. The top-middle time series represents the basal melt rate. The bottom-middle time series represents the sea ice shear, divergence and total deformation rate of sea ice. The bottom time series represents the ice-ocean stress curl. All of the figures indicate little activity or change throughout the winter months with exception of a disturbance beginning in the middle of December and last through the middle January. At first glance there appears a couple disturbances in the ocean potential temperature profile along with dominant peaks in basal melt rate as well as the sea ice deformation and ice-ocean stress curl.

Figure 34 depicts a zoomed in or cropped version of Figure 33 in order to focus in on these aforementioned disturbances in the time series. The black oval indicates the two events of interest on ~20DEC and 31DEC. A closer look these events suggests that they are even more pronounced. The ocean temperature structure shows the temperatures at 2.5, 7.5, 12.5, 17.5, 23, 30, 47.4, and 59m depths converging at a "median" temperature for each of the two respective events. For the first event (20DEC), the water temperature rises at depths of 2.5, 7.5, and 12.5m while it drops at depths of 17.5, 23, 30, and 47.4m. For the second event (31DEC), the water temperature rises at depths of 2.5, 7.5, 12.5, 17.5, and 23m while it drops at depths of 30, 47.4, and 59m. For both events, this structure indicates the water column has become well mixed while the temperature indicates that warmer water has been introduced into the column from below the stratification depth. This explains the convergence of the temperature at the various depths. Both of the spikes in the basal melt rate further support the argument that the temperature in the water column of the upper ocean has increased. The basal melt rate reaches ~3 and 2 cm/day, respectively, which is fairly substantial especially when compared with the values of the full the time series. Additionally, both events exhibit positive ice-ocean stress curls coincident with the strong shear deformation spikes indicating upwelling of the pycnocline will follow as induced by the counterclockwise rotation in the ice velocity field relative to the underlying ocean in the northern hemisphere (right hand rule). Overall, these results indicate that two shear deformation

88

events, with a positive ice-ocean stress curl, may have induced a response in the upper ocean such that warmer water was upwelled from below the stratification depth and into the mixed layer resulting in the overall warming of the upper ocean water column and subsequent increases in the basal melt rate of sea ice.

In order to more directly compare the timing of these events and the resulting disturbances through causality and response, the cropped time series were overlaid on one another in the same plot. Figure 35 depicts an overlay of the basal melt rate and the ice-ocean stress curl. The black oval again indicates the events of interest. There are clearly defined spikes coincident with both variables where the basal melt rate increases to ~3 cm/day and later ~2 cm/day. This supports the conclusion of a tight ice/ocean coupling relationship. Figure 36 depicts an overlay of the total deformation rate and the basal melt rate. Again similar coincident spikes are clearly defined. This again shows the tight coupling at the ice/ocean interface. Figure 37 depicts an overlay of the ocean potential temperature structure and the total deformation rate. Again, there are spikes in the total deformation rate coincident with warming of the ocean structure for both events. Both of these events indicate warming on the order of the $\sim0.3^{o}$ as the temperature is raised from -1.8^{o} (which is approximately freezing) to -1.5^{o}, which is below freezing and thus causing melt. The evidence that there were two strong shear deformation events both with a positive ice-ocean stress curls coincident with the warming and mixing of the upper ocean resulting in an increase in the basal melt rate supports the conclusion that there is a tight coupling relationship between the ice and ocean and that the hypothesized dynamics and events do occur within the model.

CASE STUDY B: GRID POINT (140,68)
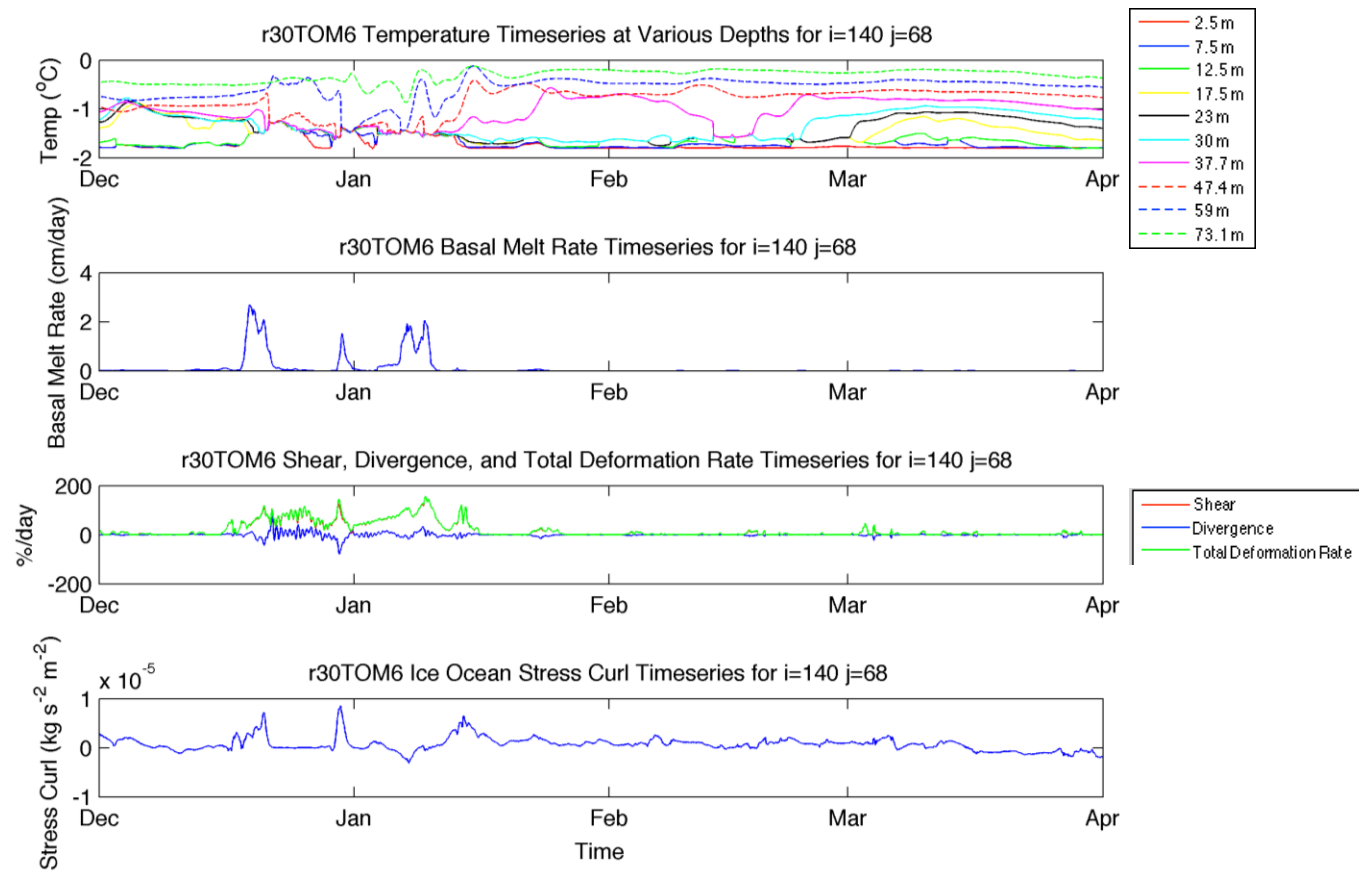
Figure 33.   Time series (DEC95-MAR96) comparison for grid point (140,68). (Top) Shows the time series for the top 10 layers of the ocean (2.5m–73.1m). (Top Middle) Shows the time series of the basal melt rate. (Bottom Middle) Shows the time series of the shear, divergence and total deformation rate. (Bottom) Shows the time series for the Ice-Ocean stress curl.

CASE STUDY B: GRID POINT (140,68)
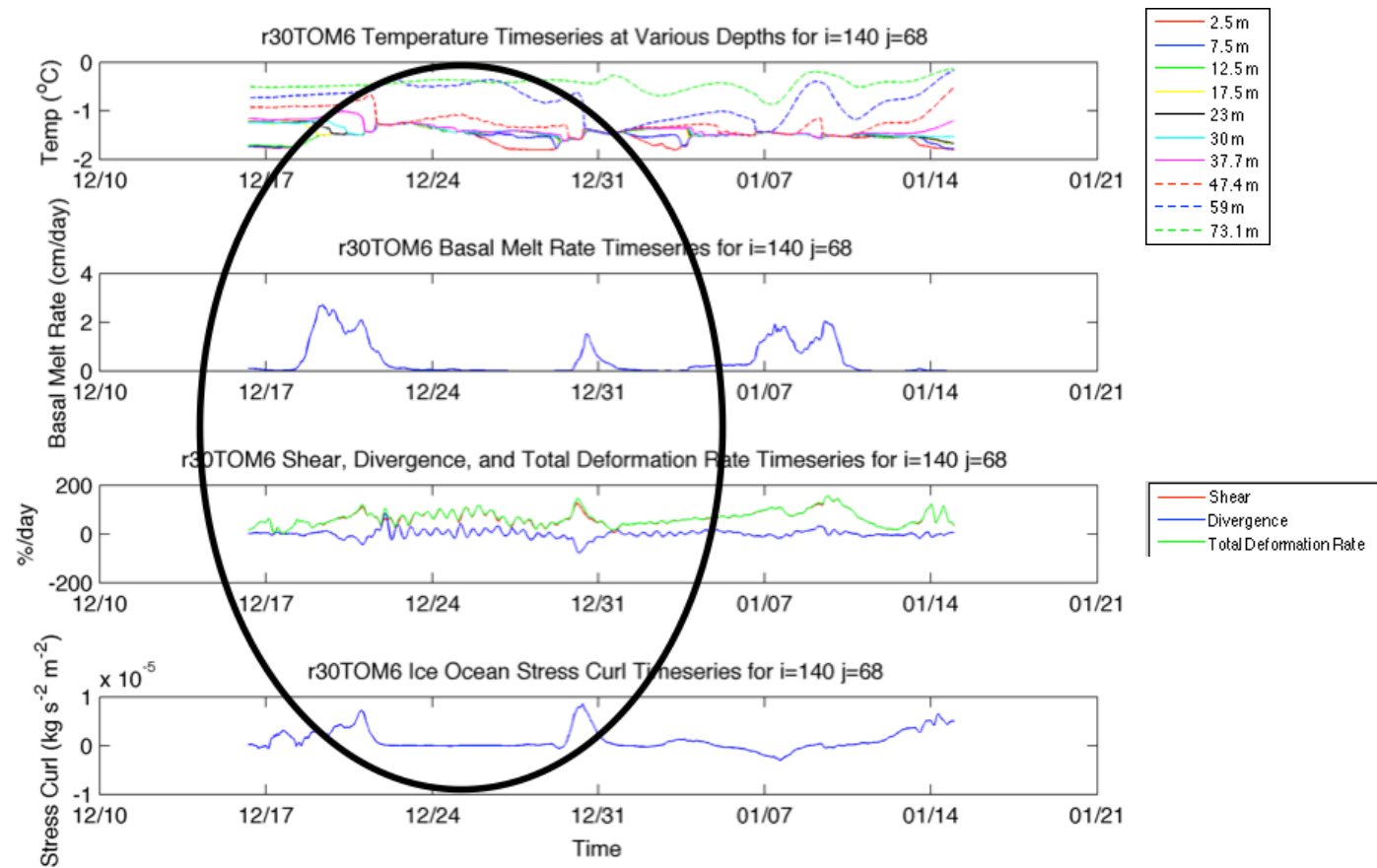
Figure 34.   Zoomed in time series (15DEC95 -15JAN96) comparison for grid point (140,68). (Top) Shows the time series for the top 10 layers of the ocean (2.5m–73.1m). (Top Middle) Shows the time series of the basal melt rate. (Bottom Middle) Shows the time series of the shear, divergence and total deformation rate. (Bottom) Shows the time series for the Ice-Ocean stress curl. Black oval indicates the event of interest.

CASE STUDY B: GRID POINT (140,68)
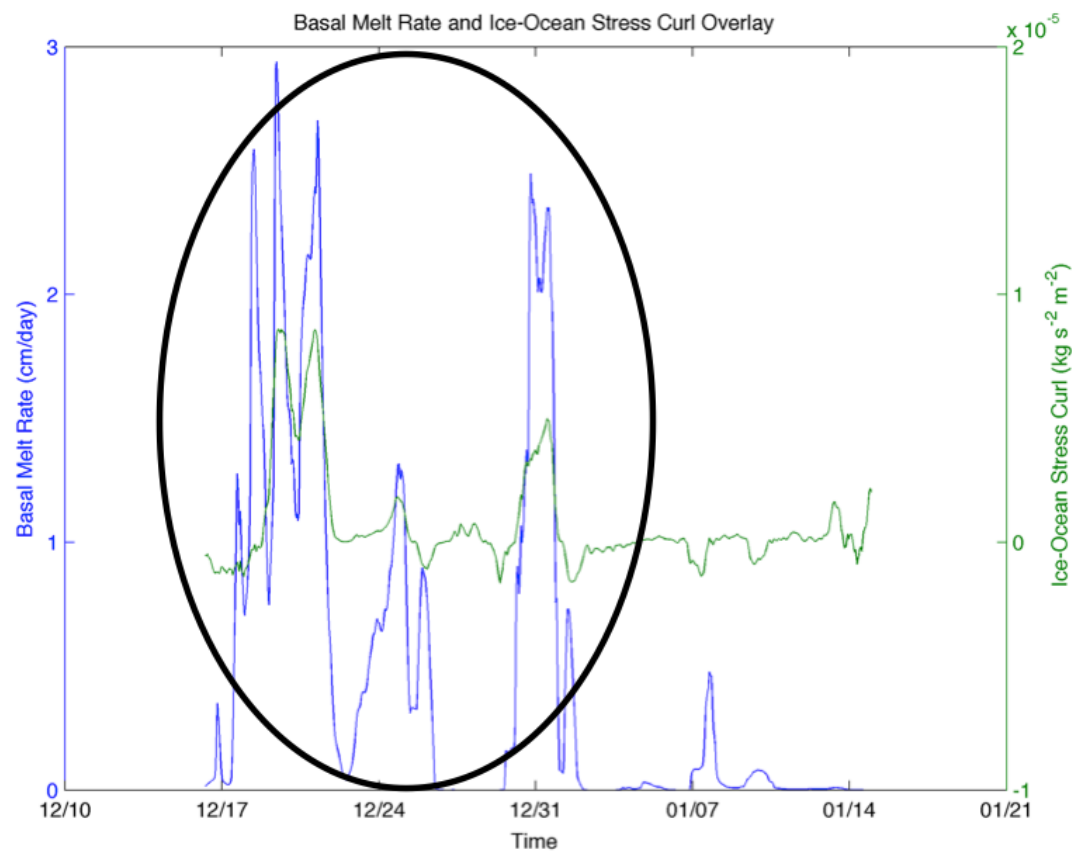
Figure 35.   Zoomed in basal melt rate and ice-ocean stress curl time series overlay (15DEC95–15JAN96). Black oval indicates the event of interest.

CASE STUDY B: GRID POINT (140,68)
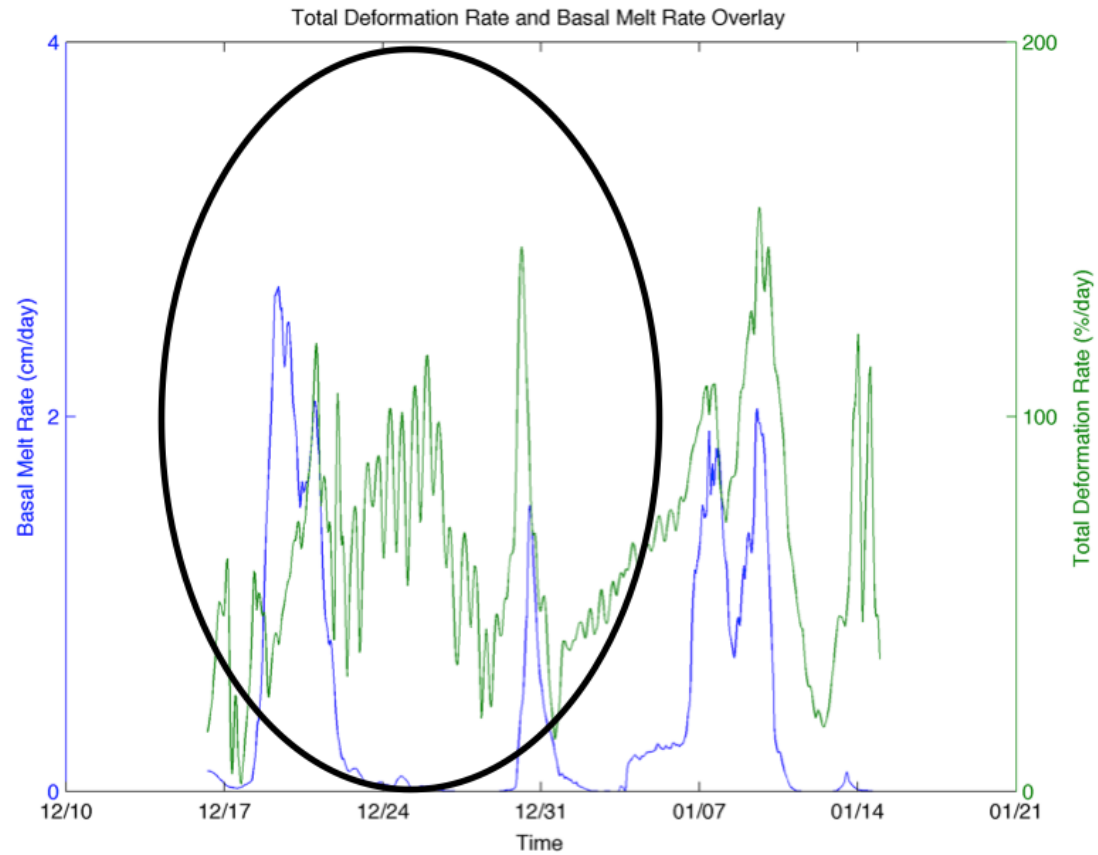
Figure 36.   Zoomed in total deformation rate and basal melt rate time series overlay (15DEC95–15JAN96). Black oval indicates the event of interest.

93
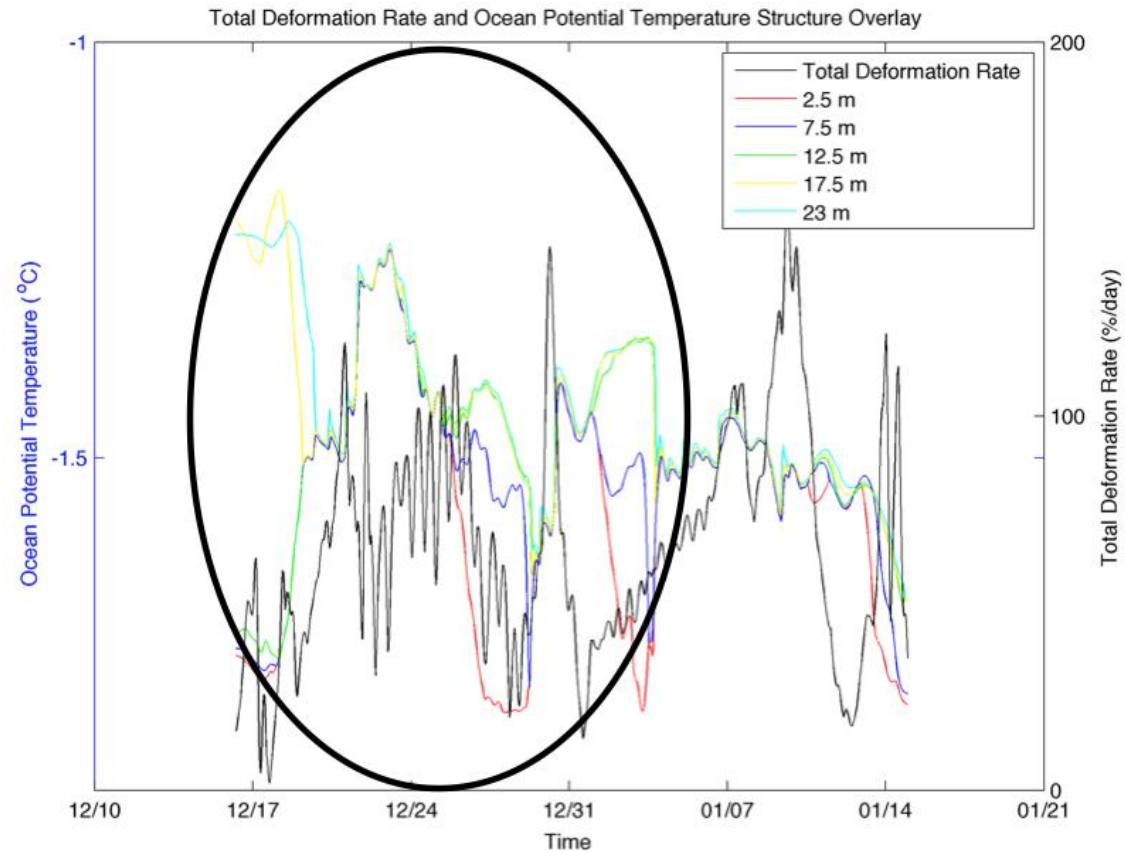
Figure 37.   Zoomed in total deformation rate and ocean potential temperature time series overlay (15DEC95–15JAN96). Black oval indicates the event of interest.

3.   Case Study C: Grid Point (155,50)

Figure 38 depicts a comparison of the time series spanning from DEC95–MAR96. The top time series represents the ocean temperature structure from 2.5m to 73.1m depth. The top-middle time series represents the basal melt rate. The bottom-middle time series represents the sea ice shear, divergence and total deformation rate of sea ice. The bottom time series represents the ice-ocean stress curl. All of the figures indicate li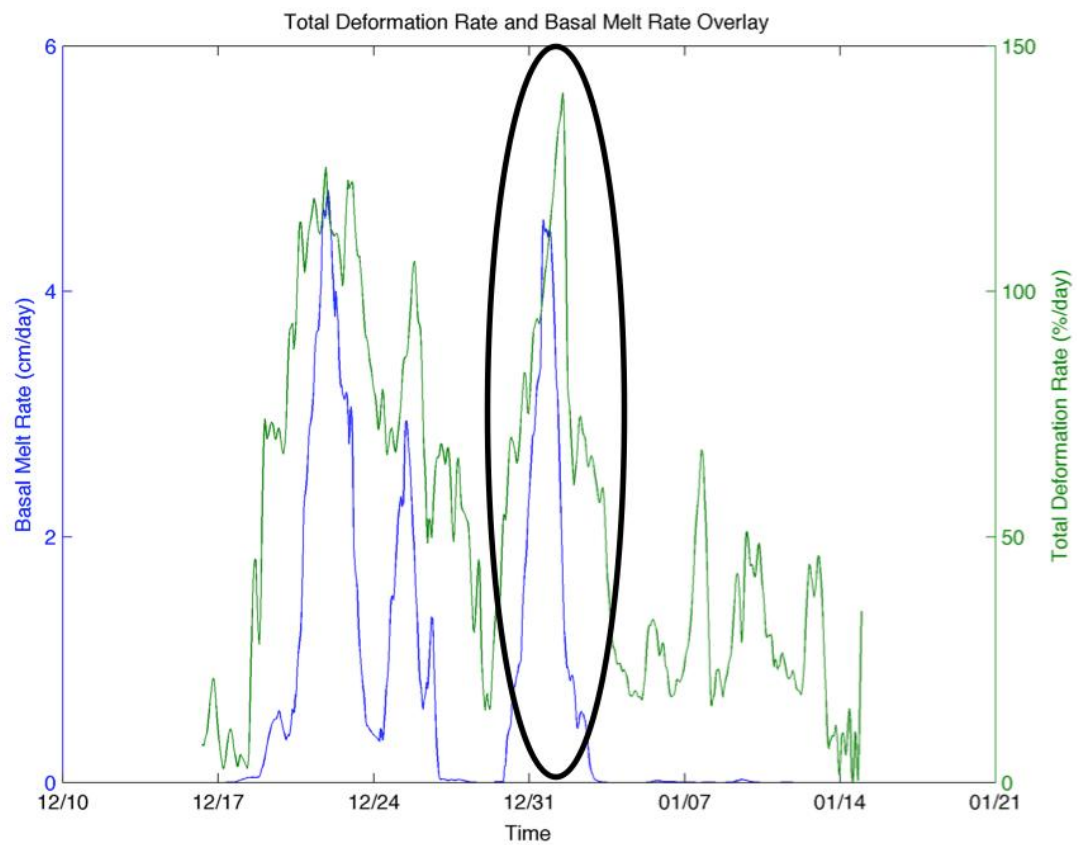ttle activity or change throughout the winter months with exception of a disturbance beginning in the middle of December and last through the middle January. At first glance there appears a few disturbances in the ocean potential temperature profile along with dominant peaks in basal melt rate as well as the sea ice deformation and ice-ocean stress curl.

Figure 39 depicts a zoomed in or cropped version of Figure 38 in order to focus in on these aforementioned disturbances in the time series. The black oval indicates the two events of interest on ~20DEC and 31DEC. A closer look these events suggests that they are even more pronounced. The ocean temperature structure shows the temperatures at 2.5, 7.5, 12.5, 17.5, 23, 30, 47.4, and 59m depths converging at a "median" temperature for each of the two respective events. Of particular note, for the first event (20DEC), there seems to be a staircase structure, in which temperatures, at increasingly deeper depths, mix with the upper ocean as time evolves. For the first event (20DEC), the water temperature rises at depths of 2.5m while it drops at depths of 7.5, 12.5, 17.5, 23, 30, 47.4, and 59m. For the second event (31DEC), the water temperature rises at depths of 2.5, 7.5, 12.5, and 17.5m while it drops at depths of 23, and 30m. For both events, this structure indicates the water column has become well mixed while the temperature indicates that warmer water has been introduced into the column from below the stratification depth. This explains the convergence of the temperature at the various depths. Both of the spikes in the basal melt rate further support the argument that the temperature in the water column of the upper ocean has increased. The basal melt rate reaches ~3 and 2 cm/day, respectively, which is fairly substantial especially when compared with the values of the full the time series. Additionally, both events exhibit positive ice-ocean stress curls coincident with the strong shear deformation spikes

indicating upwelling of the pycnocline will follow as induced by the counterclockwise rotation in the ice velocity field relative to the underlying ocean in the northern hemisphere (right hand rule). Overall, these results indicate that two shear deformation events, with a positive ice-ocean stress curl, may have induced a response in the upper ocean such that warmer water was upwelled from below the stratification depth and into the mixed layer resulting in the overall warming of the upper ocean water column and subsequent increases in the basal melt rate of sea ice.

In order to more directly compare the timing of these events and the resulting disturbances through causality and response, the cropped time series were overlaid on one another in the same plot. Figure 40 depicts an overlay of the basal melt rate and the ice-ocean stress curl. The black oval again indicates the events of interest. There are clearly defined spikes coincident with both variables where the basal melt rate increases to ~3 cm/day and later ~2 cm/day. This supports the conclusion of a tight ice/ocean coupling relationship. Figure 41 depicts an overlay of the total deformation rate and the basal melt rate. Again similar coincident spikes are clearly defined. This again shows the tight coupling at the ice/ocean interface. Figure 42 depicts an overlay of the ocean potential temperature structure and the total deformation rate. Again, there are spikes in the total deformation rate coincident with warming of the ocean structure for both events. Both of these events indicate warming on the order of the ~0.5^o as the temperature is raised from -1.8^o (which is approximately freezing) to -1.3^o, which is below freezing and thus causing melt. The evidence that there were two strong shear deformation events both with a positive ice-ocean stress curls coincident with the warming and mixing of the upper ocean resulting in an increase in the basal melt rate supports the conclusion that there is a tight coupling relationship between the ice and ocean and that the hypothesized dynamics and events do occur within the model.

CASE STUDY C: GRID POINT (155,50)
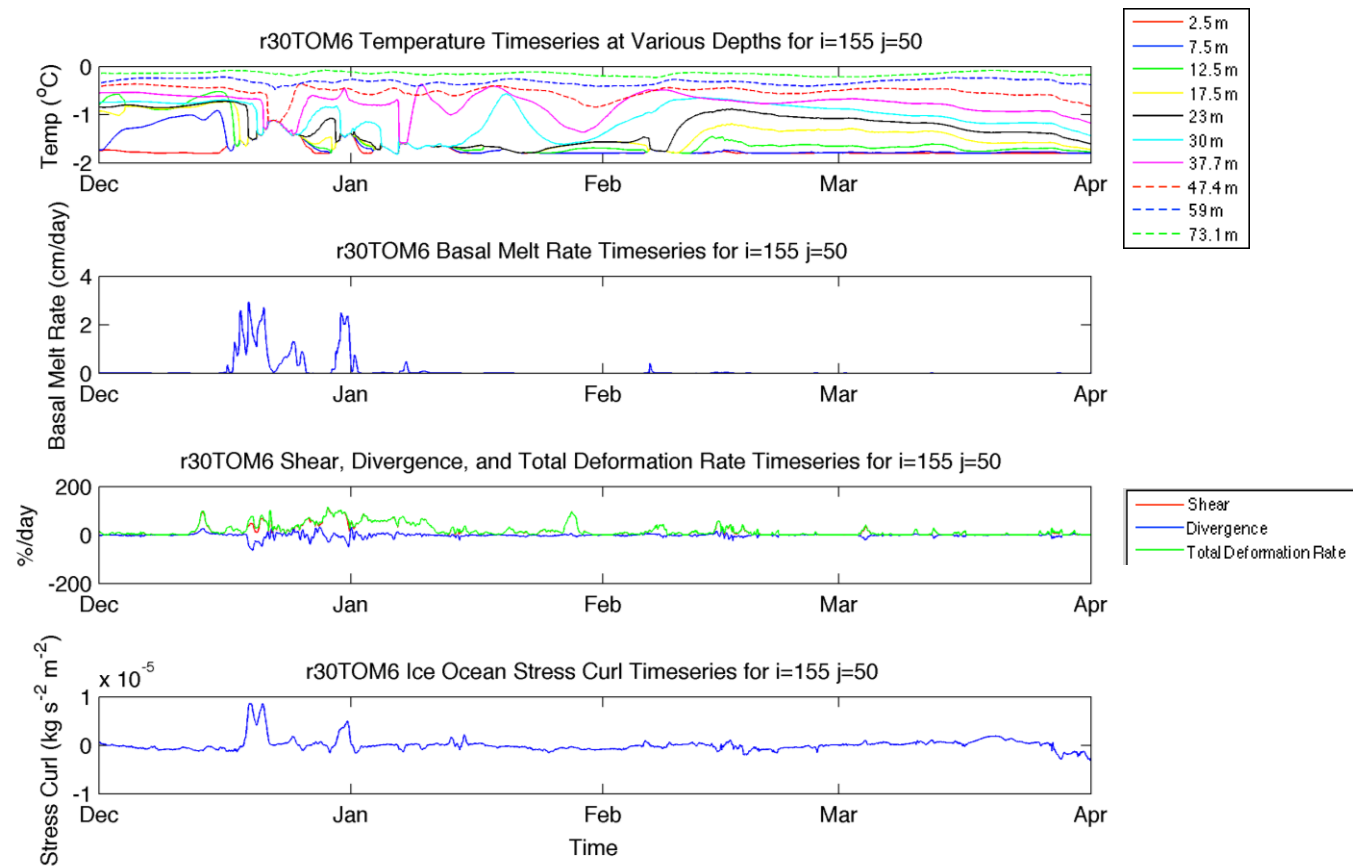
Figure 38.   Time series (DEC95-MAR96) comparison for grid point (155,50). (Top) Shows the time series for the top 10 layers of the ocean (2.5m–73.1m). (Top Middle) Shows the time series of the basal melt rate. (Bottom Middle) Shows the time series of the shear, divergence and total deformation rate. (Bottom) Shows the time series for the Ice-Ocean stress curl.

97

CASE STUDY C: GRID POINT (155,50)
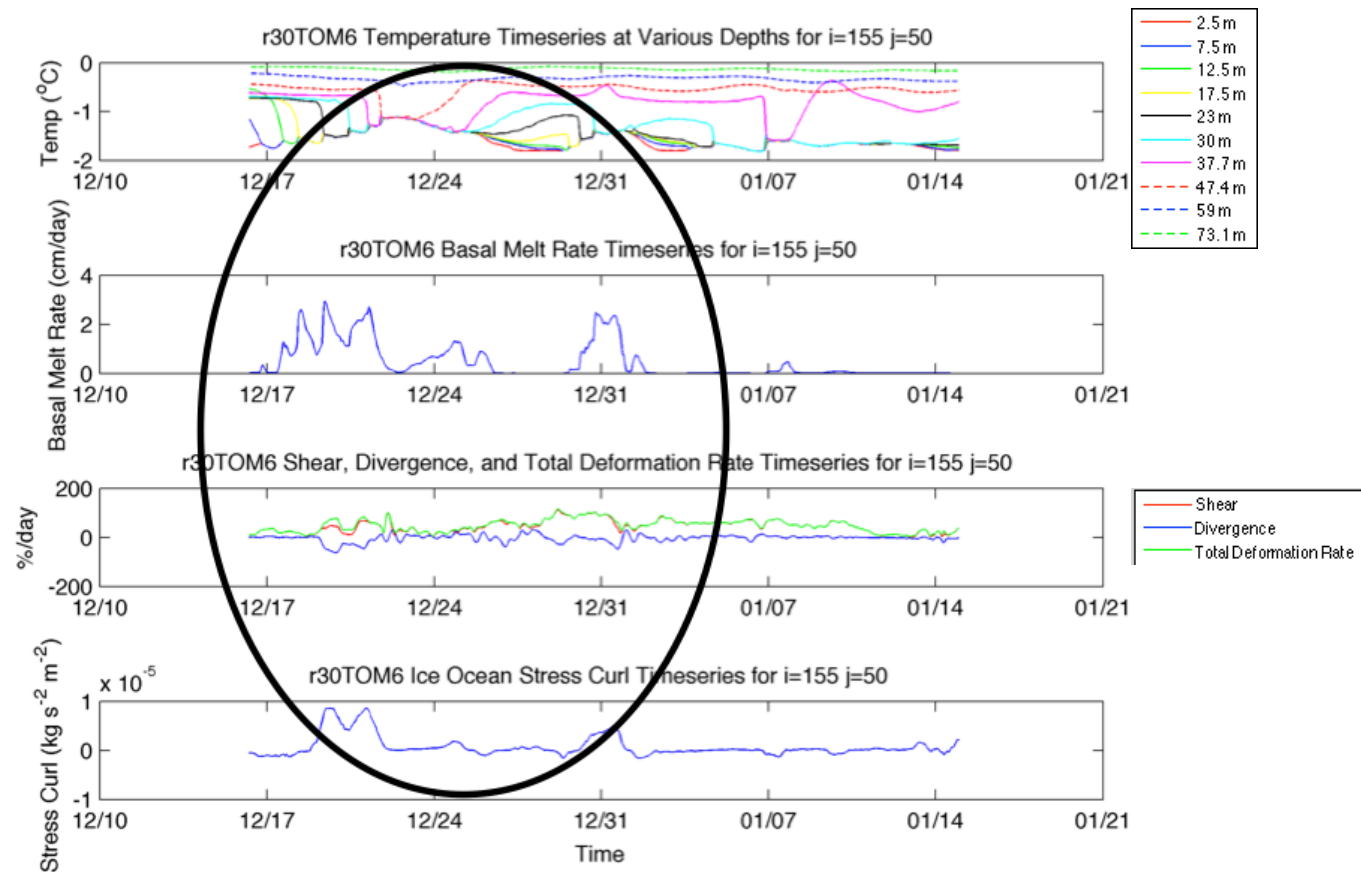
Figure 39. Zoomed in time series (15DEC95 -15JAN96) comparison for grid point (155,50). (Top) Shows the time series for the top 10 layers of the ocean (2.5m–73.1m). (Top Middle) Shows the time series of the basal melt rate. (Bottom Middle) Shows the time series of the shear, divergence and total deformation rate. (Bottom) Shows the time series for the Ice-Ocean stress curl. Black oval indicates the event of interest.
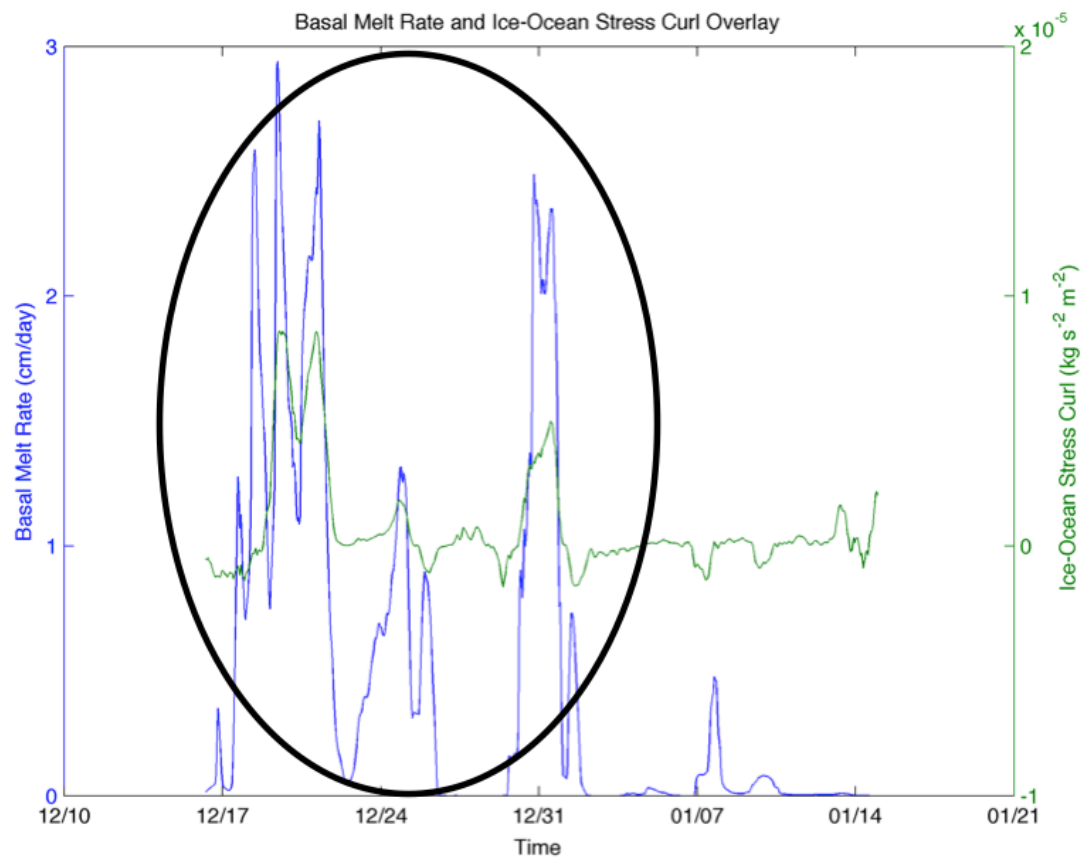
Figure 40.   Zoomed in basal melt rate and ice-ocean stress curl time series overlay (15DEC95–15JAN96). Black oval indicates the event of interest.

CASE STUDY C: GRID POINT (155,50)
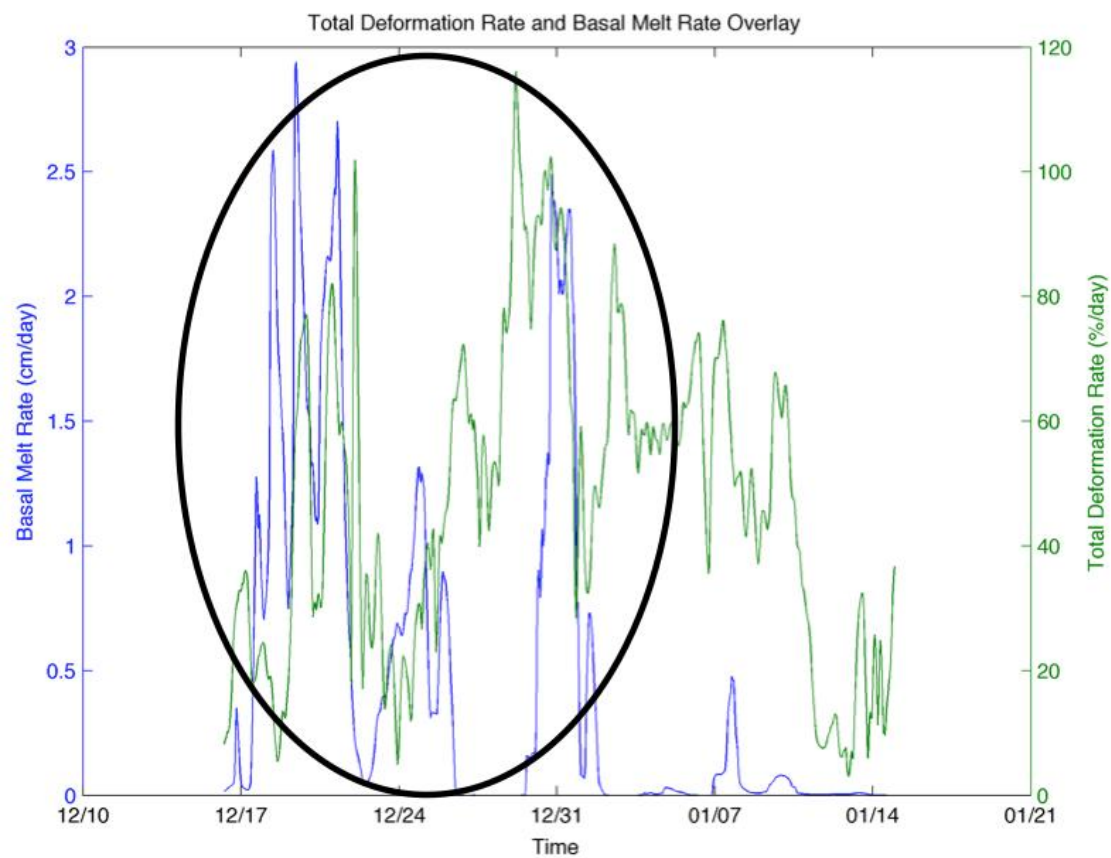
Figure 41.   Zoomed in total deformation rate and basal melt rate time series overlay (15DEC95–15JAN96). Black oval indicates the event of interest.

CASE STUDY C: GRID POINT (155,50)
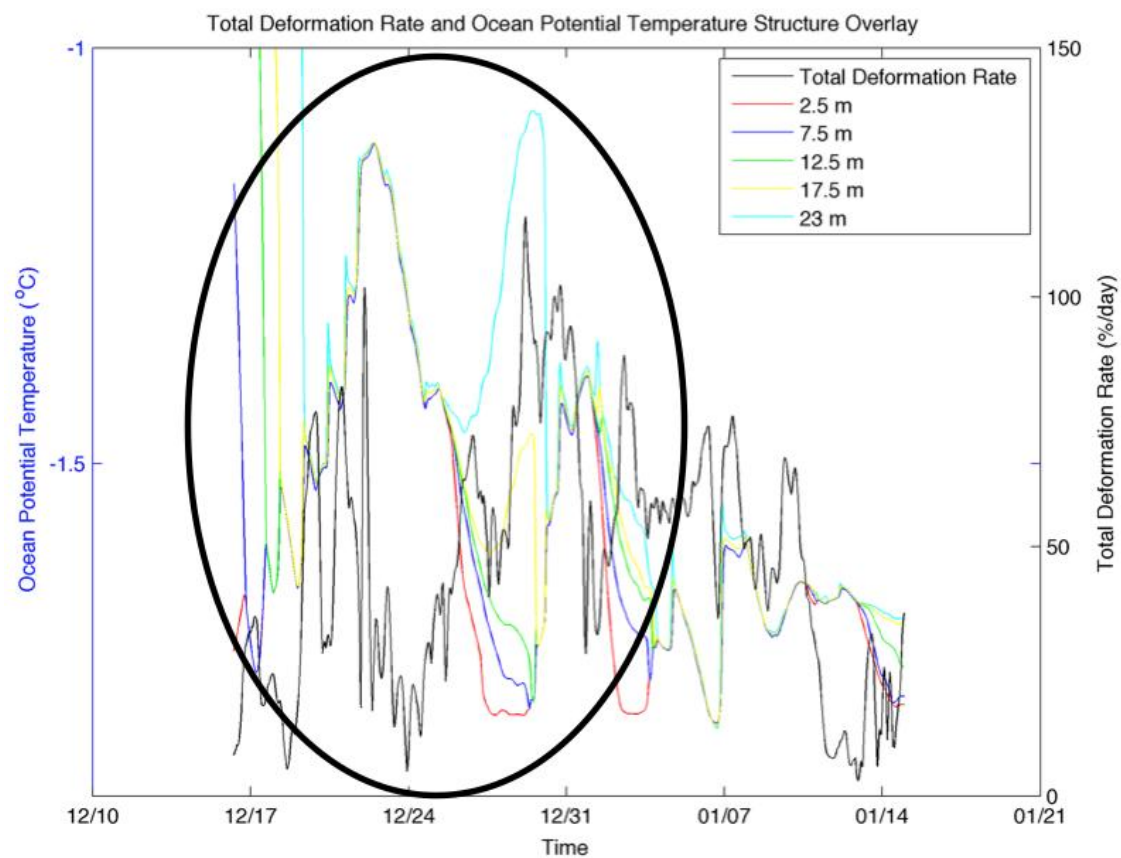
Figure 42.   Zoomed in total deformation rate and ocean potential temperature time series overlay (15DEC95–15JAN96). Black oval indicates the event of interest.

4. Answer to Question #1

Is a numerical model capable of representing the proposed dynamics and ice/ocean-coupling relationship for deformation induced upwelling?

Yes, the evaluation of the previous case studies has shown that there is consistency in shear deformation events generating an upper ocean response given the correct sign of the ice-ocean stress curl. Exchange of properties across the pycnocline follows if the ice-ocean stress curl is positive, i.e., induced by the counterclockwise rotation in the ice velocity field relative to the underlying ocean in the Northern Hemisphere. The high temporal and spatial resolution of RASM seems to do an adequate job representing these events. The time series showed that these events occur very infrequently and require a very specific set of conditions in order to take place. This raises the question of whether or not there are more events similar to this that occur more frequently, but at a lesser magnitude and RASM is just not capable of resolving them. This brings into focus the next research question of if these events do occur what are their statistical prevalence as well as their overall effect on the ice?

B. QUESTION #2: WHAT IS THE STATISTICAL PREVALENCE OF THESE EVENTS AND THEIR OVERALL EFFECT ON THE ICE PACK?

1. Spatial and Temporal Characterization of the Total Sea Ice Deformation

To begin the statistical analysis, the spatial characterization of the total sea ice deformation rate was first investigated as an independent verification of Marsan et al. (2004), Girard et al. (2009), Stern and Lindsay (2009), and Hutchings et al. (2010). This involved calculating the sea ice deformation rate at various spatial scales to analyze the rate of change of the total sea ice deformation. This calculation was done for all grid points in the Beaufort Sea region with an ice concentration greater than 85% at scale bins starting at 9km and increasing by 9km in each bin up to 99km. In order to look at the total deformation rates at different scale lengths, the model grid was "re-sized" for each calculation. For example, RASM outputs sea ice data at a $(9km)^2$ grid, in order to calculate the total sea ice deformation rate at an $(18km)^2$ grid, the total deformation rate was averaged for four $(9km)^2$ grid points resulting in a total deformation rate for an

$(18 \text{km})^2$ grid. The averaging was done so that no $(9 \text{km})^2$ grid point overlapped in subsequently larger scale length calculations, thus the results were statistically independent. This same calculation was done for al scale lengths that were a factor of 9 up to $(99 \text{km})^2$ metric. This change in grid size adjusted the grid area distribution within the calculation domain as seen in Figure 43.
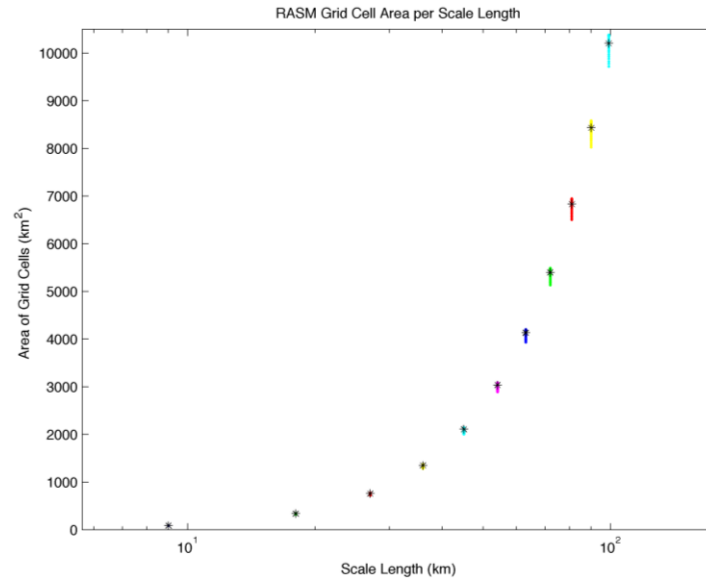
Figure 43.   Describes the RASM grid cell area as a function of scale length bins (9, 18, 27 36, 45, 54, 63, 72, 81, 90, & 99km). It should be noted that the x-axis is in log format. As the scale length increases so does the mean grid cell area. The black stars indicate these mean values.

At a higher resolution, ~9-km, the range of the size of grid areas is very small across the Arctic and North Pole, but as the scale grid size increases, the grid areas increase, and the range of the size of the grid areas increase as well. This is a result of the model domain encompassing a pole on the Earth where there is a convergence of longitude and latitude. The grid areas are smaller closer to the pole, thus combining smaller grids near the pole will result in smaller grid areas compared to grids combined at a lower-latitude. Figure 43 shows the exponential increase, on a logarithmic x-axis, of the range of grid area sizes as a function of increasing scale length. This indicates that calculations at a larger grid size are subject to a larger range of grid areas across the

domain and helps to describe the scale bins variability for which the total deformation rate will be calculated.

The results of the spatial characterization of the total deformation of sea ice at one hour temporal sampling can be seen in the upper right of Figure 44. The different colors of total sea ice deformation represent the results for the various scale bins $(9-99km)^2$. A black star indicates the average of each scale bin. The least squares fit, of the mean total deformation rate across the scale bins is represented by the solid black line. The gradient of the mean deformation rate was calculated for comparison purposes to other studies. The open circle represents the variance of the total deformation rate, at each scale bin. Again the dashed line represents the least squares fit of the variance.

In addition to the model verification of the total sea ice deformation rate, the analysis was taken a step further and the total deformation rate was calculated by averaging across different time scales from one hour, 3 days, 6 days, and 30 days, respectively. This allowed for a temporal characterization as well. Each of these respective time averaged cases are also found in Figure 44. Each of the time-averaged cases show that as the scale length decreases, larger strain rates become more apparent. Additionally, as the temporally averaging time is increases, the range of the total deformation rate, for each scale bin, decreases.

The mean deformation rate, D, was found to scale logarithmically with the length scale, L, such that D is proportional to L raised to the power of the exponent H. The exponent H more simply represents the gradient of the mean deformation rate.

$$D = L^H \qquad (9)$$

The deformation rate exhibited considerable localization and fractal behavior, in which the largest deformation rates are confined to smaller and smaller areas as the scale of the measurement decreases. Figure 45 shows a comparison of the mean deformation rates calculated for each temporal averaging case. As the temporal scale used for averaging increases so does the rate of change of the deformation at larger spatial scales.

This may indicate that the time scaling exponent depends on the spatial scale and the spatial exponent on the temporal scale indicating time/space coupling.

Table 2 compares these gradient values to other studies involving RGPS and buoy array observations. These observations also include various temporal sampling frequencies, hence multiple time averaging calculations. The results from RASM compare well with the other studies, given the respective sampling frequencies.

Table 2.   Gradient of mean total deformation rate comparison

Source	Method of Observation	Temporal Sampling	Exponent H
Marsan et al. (2004)	RGPS	3 Days	-0.2
Stern and Lindsay (2009)	RGPS	3 Days	~-0.2
Girard et al. (2009)	RGPS	3 Days	-0.18
Hutchings et al. (2010)	Buoy Arrays	10 Minutes	-0.19
Girard et al. (2009)	Model (LIM)	Unknown	Not well simulated
Mills (2012)	Model (RASM)	1 hr, 3, 6, and 30 Days	-0.23, -0.26, -0.28, -0.32*

Of particular interest is the study by Girard et al. (2009) where in addition to an evaluation of the RGPS, there was an evaluation of the Louvain-la-Neuve Ice Model (LIM), which was unable to reproduce the spatial and temporal correlations for the deformation field in both VP and EVP simulations. Girard et al. (2009) concluded that a different modeling framework based on elastic interactions could improve the representation of the statistical and scaling properties of sea ice. It was thought that there were issues misrepresenting sea ice as an isotropic material when it is actually anisotropic.

Strictly by modeling comparisons alone a few differences standout. Girard et al. (2009) did not indicate a specific atmospheric forcing component for the LIM simulations, but RASM utilizes the NCAR WRF model with continuous coupled input,

while many models that are not fully coupled use reanalysis and only update a couple cycles per day. Additionally, since RASM is fully coupled with all model components, it is able to represent the cascade of energy and background noise inherent in the signals much better than models that are not fully coupled. This indicates that even though the CICE model is not representing granular mechanics and anisotropic conditions, but isotropic conditions, the model does a reasonably good job simulating the same results as the observations. This result does not necessarily indicate the need for an anisotropic sea ice model as previous studies have indicated.

With the representation of the sea ice deformation rates similar to observations, mainly attributed to the fact that RASM is fully coupled, further analysis with respect to interactions with the upper ocean are assumed to be well represented and appropriate within the model. Overall, this type of statistical study is a way of understanding the importance of fine scale events and broad scale statistics. The results indicate that fine temporal and spatial resolution, on a statistical scale, are important for the overall energy budget of the Arctic.
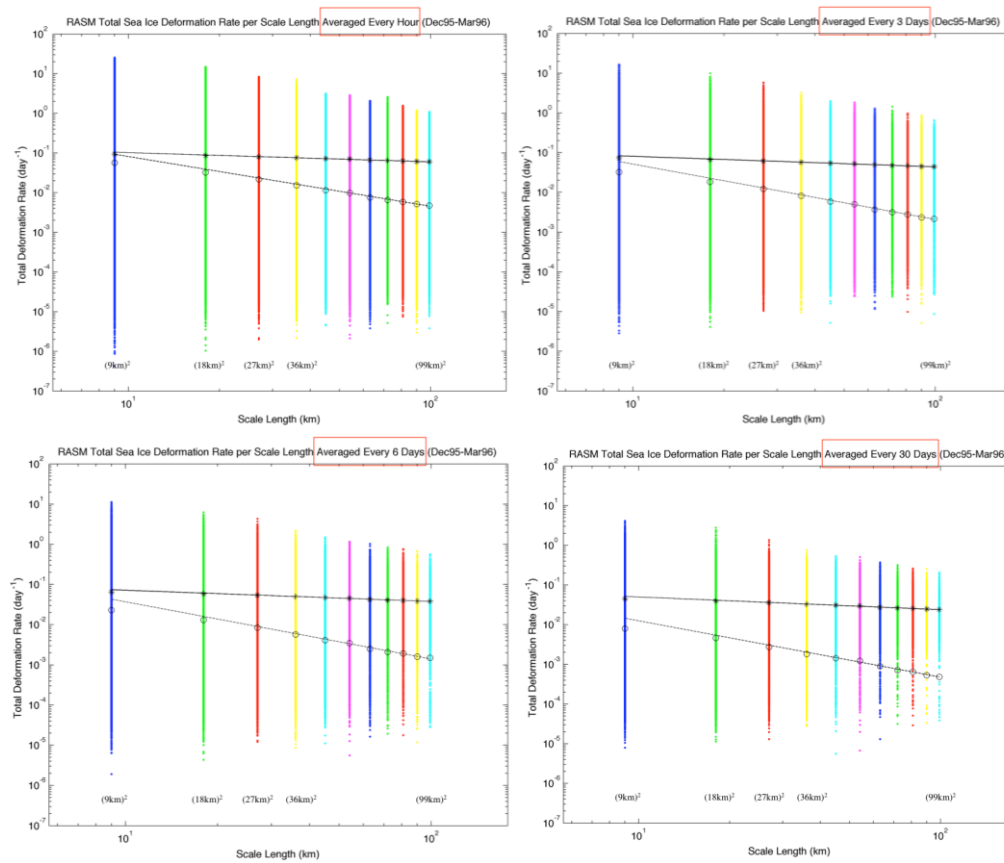
Figure 44. (Top left) describes the RASM total sea ice deformation rate as a function of scale length averaged every hour. The stars represent the mean deformation rate at each respective scale length and the black solid line is the line of best fit. The open circles represent the variance of deformation rate and the black dashed line is the line of best fit. (H = -0.23). (Top right) describes the RASM total sea ice deformation rate as a function of scale length averaged every 3 days. (H = -0.26). (Bottom left) describes the RASM total sea ice deformation rate as a function of scale length averaged every 6 days. (H = -0.28). (Bottom right) describes the RASM total sea ice deformation rate as a function of scale length averaged every 3 days. (H = -0.32)
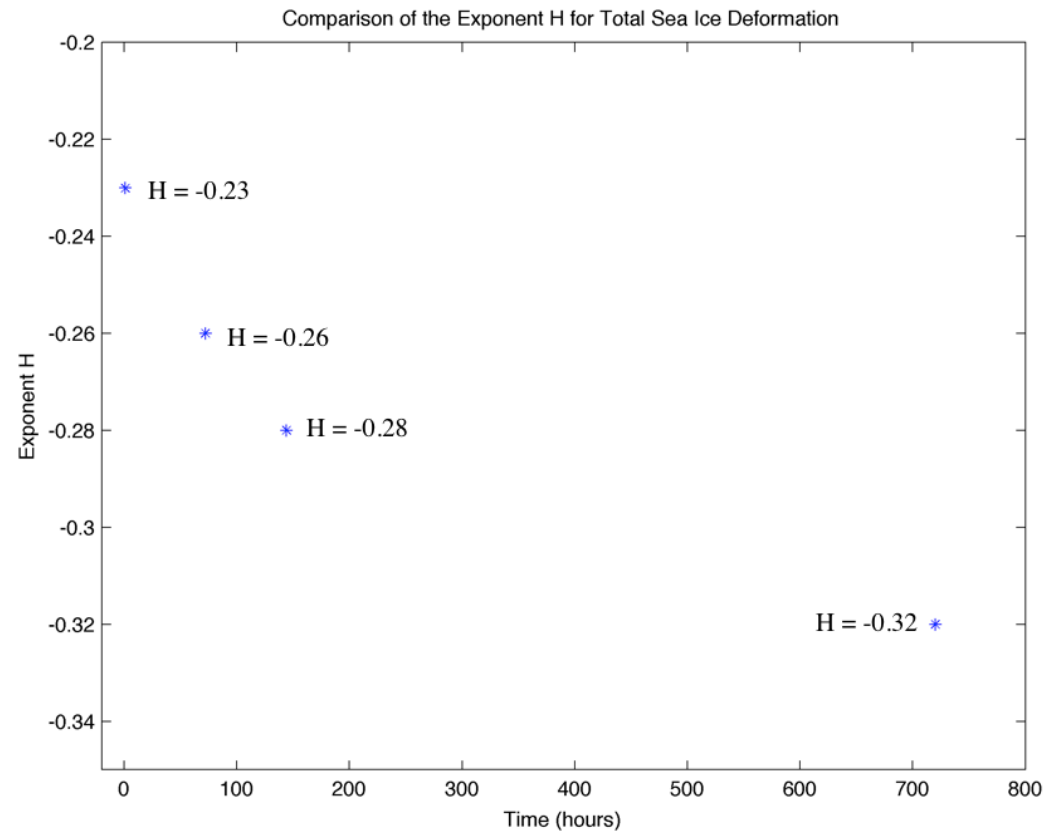
Figure 45. Describes how the exponent H changes over the various temporal averaging methods (1 hour, 3 days, 6 days, and one month). The exponent value decreases as the temporal scale increase

2. Spatial and Temporal Characterization of the Basal Melt Rate

A similar characterization of the total sea ice deformation rate was also done for the basal melt rate. Figure 46 shows a comparison of the mean basal rates calculated for each spatial scale bin as well as each temporal averaging case. Figure 47 shows a comparison of the mean basal rates calculated for each temporal averaging case. Each of the time-averaged cases show that as the scale length decreases, larger strain rates become more apparent. As the temporal scale used for averaging increases the rate of change of the basal melt rate becomes less negative at larger spatial scales. This, again, may indicate that the time scaling exponent depends on the spatial scale and the spatial exponent on the temporal scale indicating time/space coupling. Overall, this type of statistical study is a way of understanding the importance of fine scale events and broad scale statistics. The results re-affirm that fine temporal and spatial resolution, on a statistical scale, are important for the overall energy budget of the Arctic.
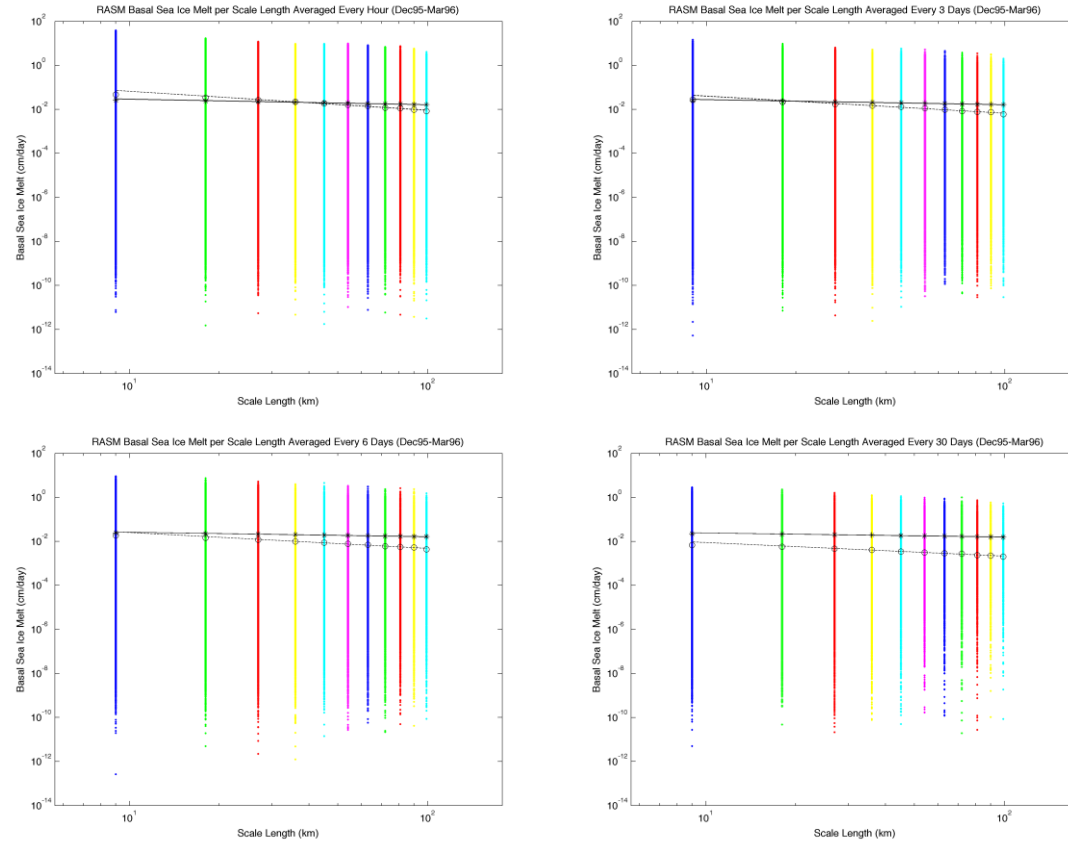
Figure 46. (Top left) describes the RASM basal melt rate as a function of scale length averaged every hour. The stars represent the mean basal melt rate at each respective scale length and the black solid line is the line of best fit. The open circles represent the variance of basal melt rate and the black dashed line is the line of best fit. (H = -0.25). (Top right) describes the RASM basal melt rate as a function of scale length averaged every 3 days. (H = -0.22). (Bottom left) describes the RASM basal melt rate as a function of scale length averaged every 6 days. (H = -0.20). (Bottom right) describes the RASM basal melt rate as a function of scale length averaged every 3 days. (H = -0.18).

110
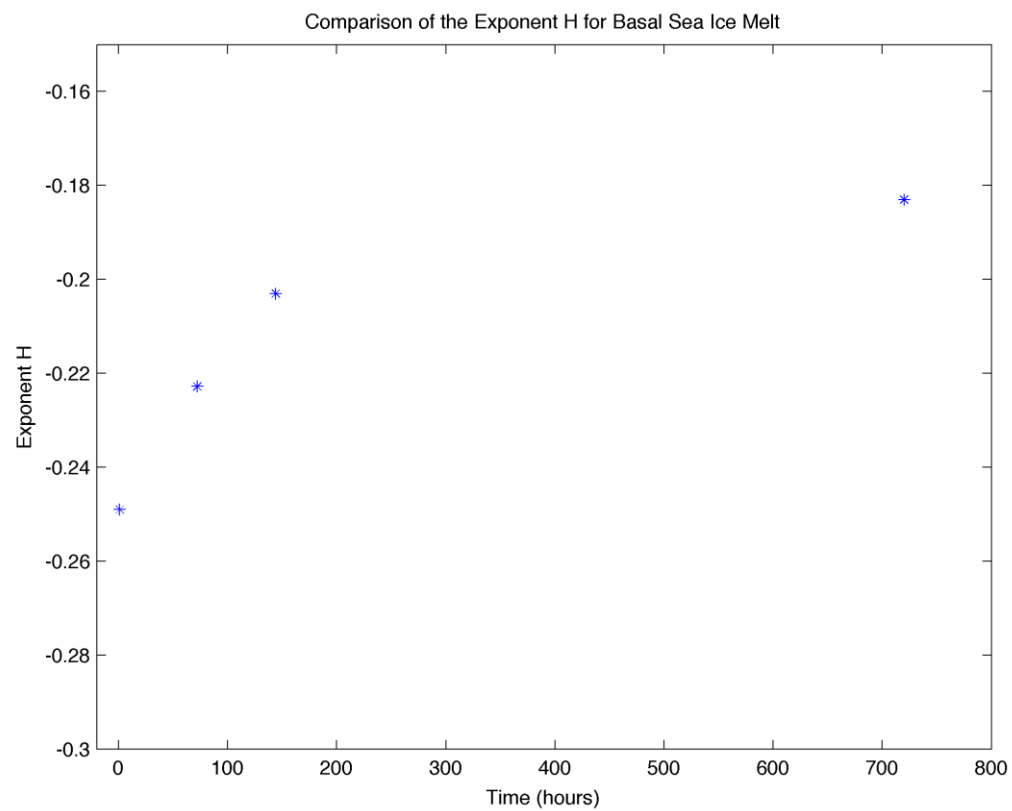
Figure 47.   Describes how the exponent H changes over the various temporal averaging methods (1 hour, 3 days, 6 days, and one month). The exponent values increase as the temporal scale increases.

3. Power Spectral Density Functions

The power spectral density functions for the ice-ocean stress curl, basal melt rate, and the shear deformation rate were calculated using the in house software package. All three of the data points from Case Studies A, B, and C were compared in each spectra to see if there were any common spectral peaks at a specific frequency. The results can be seen in Figures 48, 49, and 50, respectively. The function used generated a scalar power spectra using Welch's method to calculate a periodogram with degrees of freedom based on the amount of hamming-window averaging of data. A frequency resolution 0.25 was used resulting in a window size of 95 based on 2850 one-hour samples available. The 95% confidence interval in shown in the figures. The results were consistent for all three of the variables and indicated that there was no spectral power peak at a preferred frequency. In fact all three of spectra exhibited the classic energy cascade going from low frequency to higher frequency. It has already been mentioned that these events are infrequent based on the time series analysis, but the power spectra tells us that there is no common frequency band and that these events appear to be rather "random." This could also be due that fact that these events may be more dominant at higher frequency and are not apparent in the spectra because they may be lost in the naturally occurring high frequency noise. Another thought is that the numerical scheme in the model maybe working to filter these subtle events out through numerical dispersion. This means that though RASM is considered to have high spatial and temporal resolution, it may take even higher resolution to resolve the common frequency band of the subtler and possibly more frequent versions of this type of event. A complete analysis of the overall effect of these events on the ice pack and sea ice variability may not be possible without further research in this area.
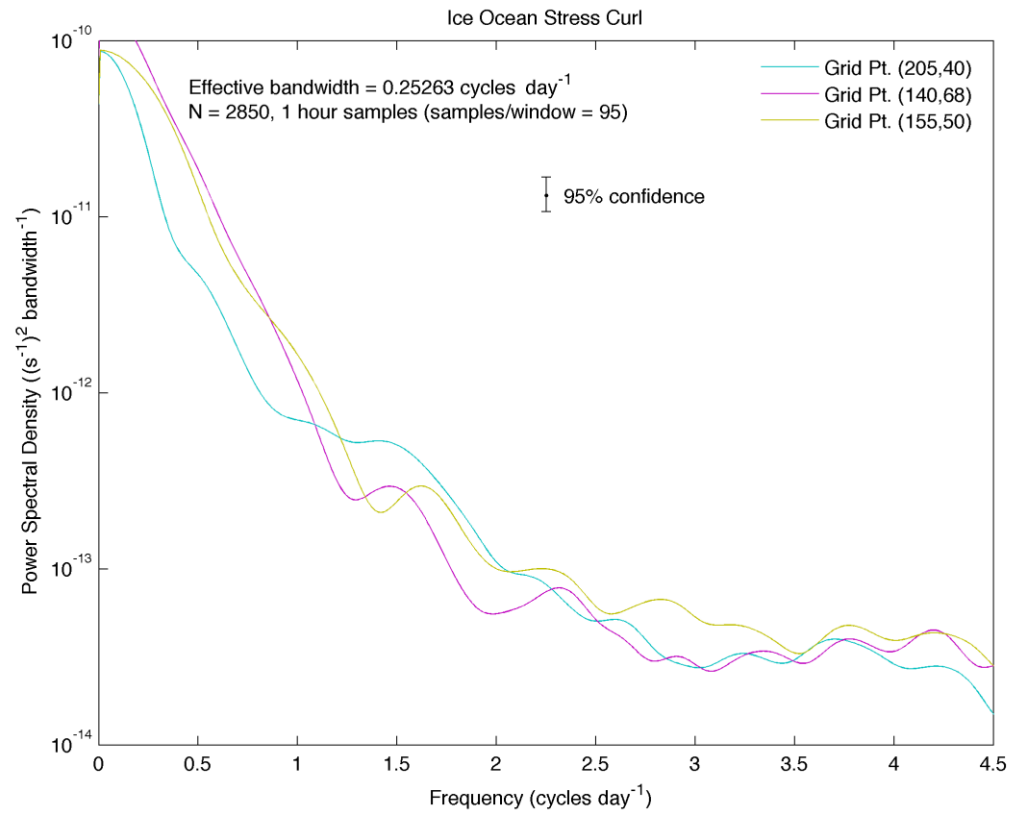
Figure 48.   Power Spectral Density Comparison of the Ice-Ocean Stress Curl for grid points from each case study (A, B, and C).
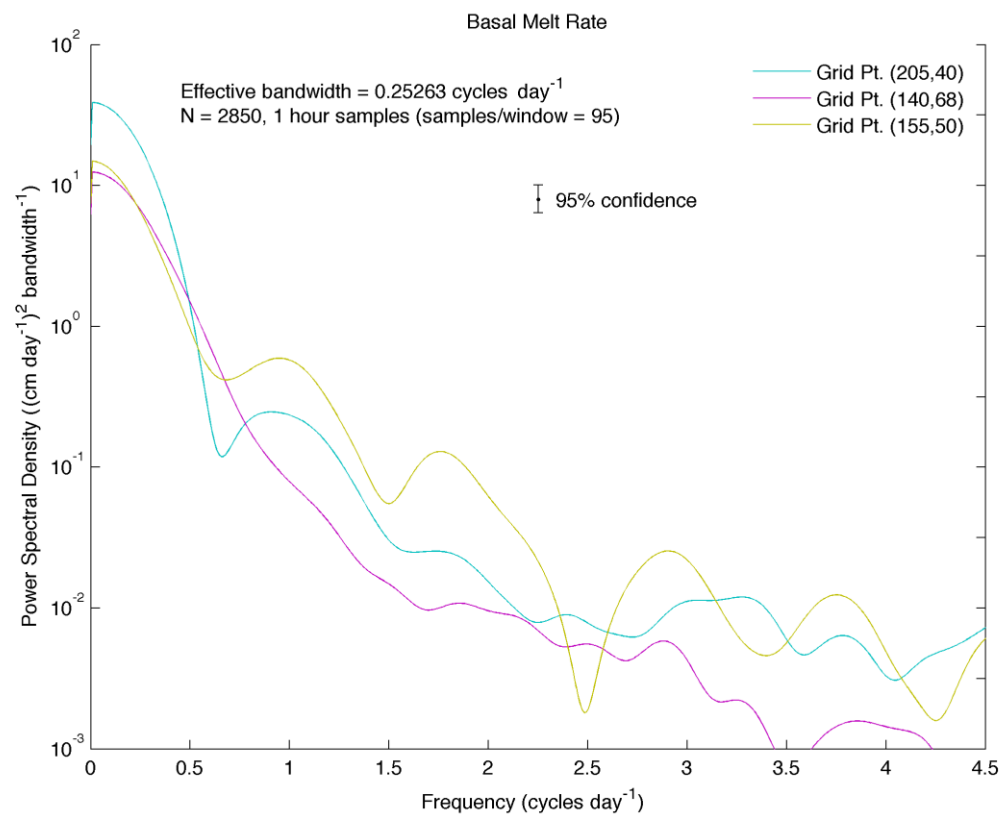
Figure 49.   Power Spectral Density Comparison of the Basal Melt Rate for grid points from each case study (A, B, and C).
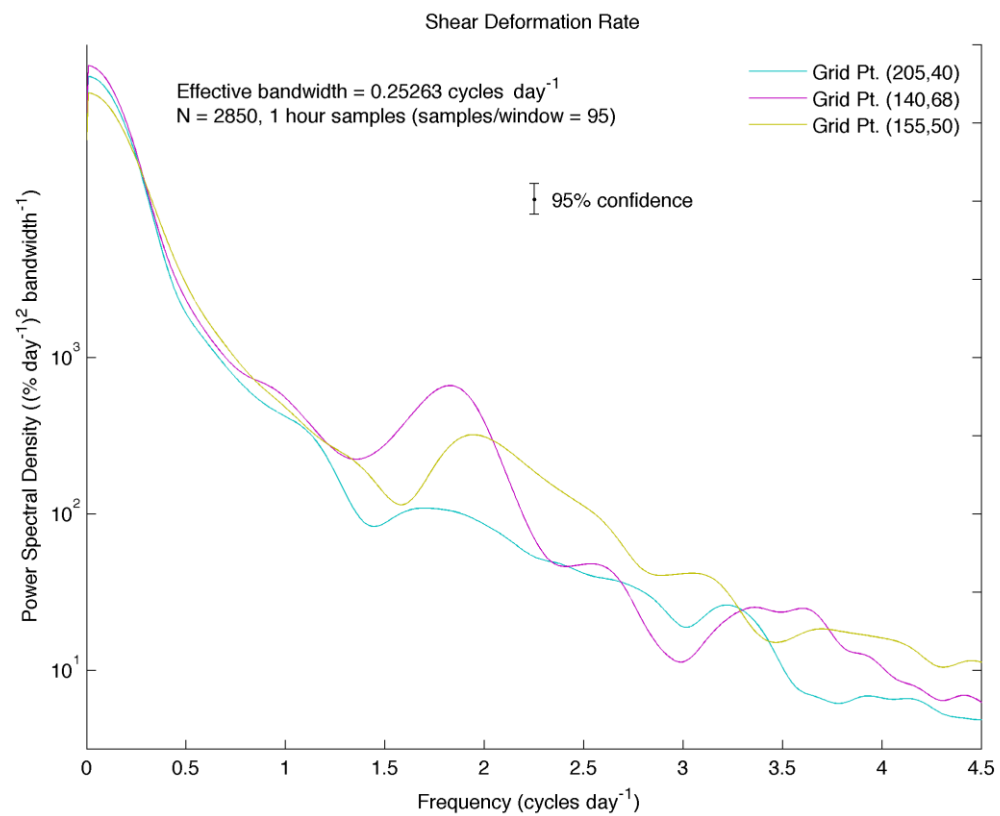
Figure 50.   Power Spectral Density Comparison of the Shear Deformation for grid points from each case study (A, B, and C).

4.   Coherence

Lastly, the standard spectral coherence was calculated in order to describe the strength of association between several time series variables where the possible dependence between two series may not be limited to simultaneous values, but may include leading, lagged and smoothed relationships. The coherence was calculated between: the ice-ocean stress curl and basal melt rate (Figure 51), the ice-ocean stress curl and the shear deformation rate (Figure 52), as well as the shear deformation rate and the basal melt rate (Figure 53). Again, this was done using in-house software. The function used Welch's method to calculate coherence using non-overlapping hamming-windowed data. Again the frequency resolution of 0.25 was used resulting in a window size of 95 based on 2850 one-hour samples available. The 99% confidence level is depicted by the dotted line in all of the figures. The results were consistent for all coherence calculations as the results show that there was little to no coherence exhibited between the variables time series for any of the comparisons. Not only is there little to no dependence between variables due to simultaneous values, but little to no dependence in leading, lagged, or smoother relationships. The small amount coherence that is shown in some of the comparisons is not consistent through all three of the grid points in each case study. Additionally, the coherence exhibited by some of the variable comparisons is at either extremely low or extremely high frequencies. The extremely low frequency coherence that is seen may be due to some diurnal variation where the extremely high frequency coherence that is seen is most likely coincidental to high frequency noise inherent in the signal. This is consistent with the results from the power spectral density calculations and again supports the conclusion that these events appear to be "random" and that if there is dependency or coherence between ice and ocean variables it may be washed out in high frequency noise or smoother/filtered out through the model's numerical calculation scheme.
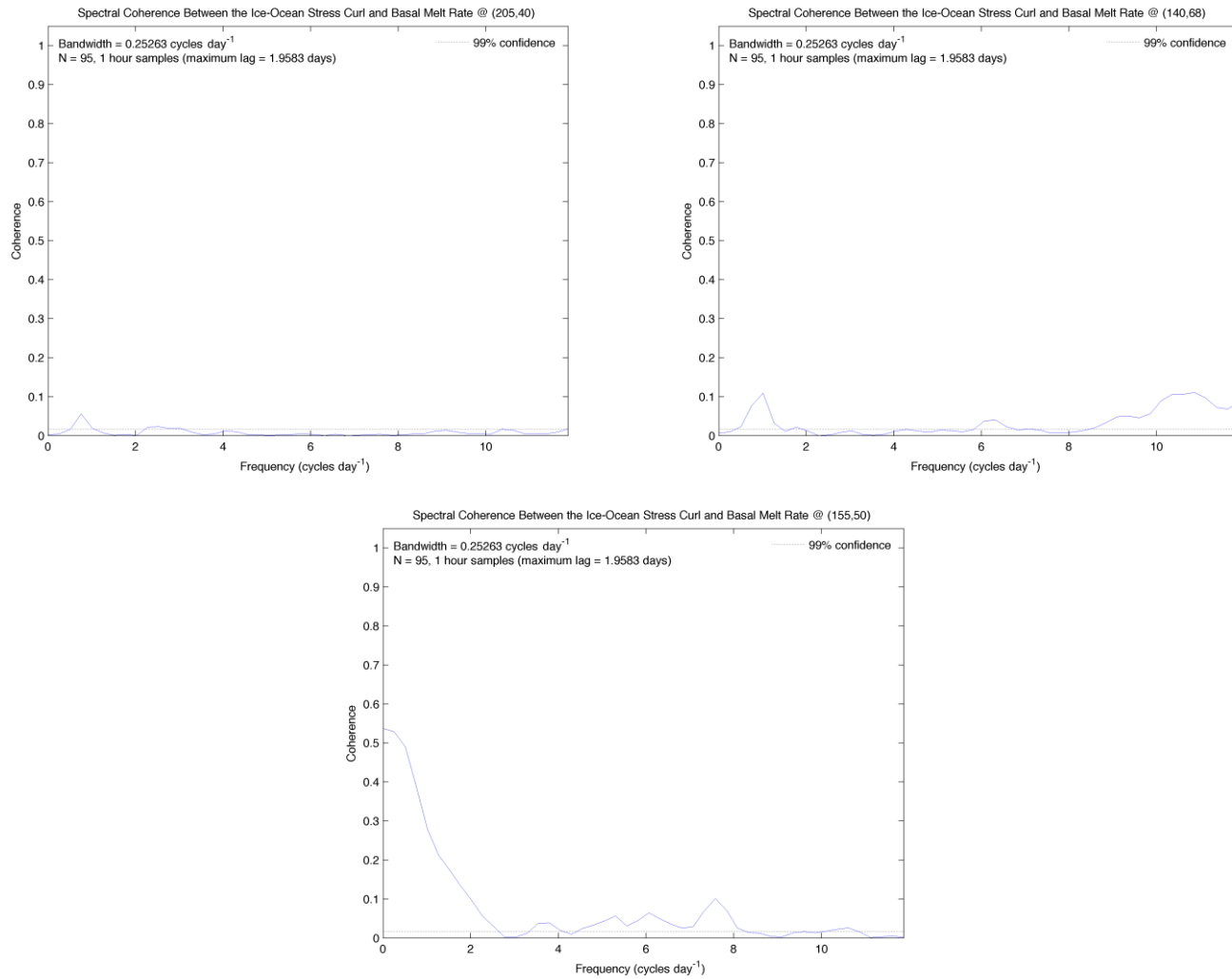
Figure 51.   Coherence between the ice-ocean stress curl and the basal melt rate. (Upper Left) Grid point (205,40) from Case Study A. (Upper Right) Grid point (140,68) from Case Study B. (Bottom) Grid point (155,50) from Case Study C.
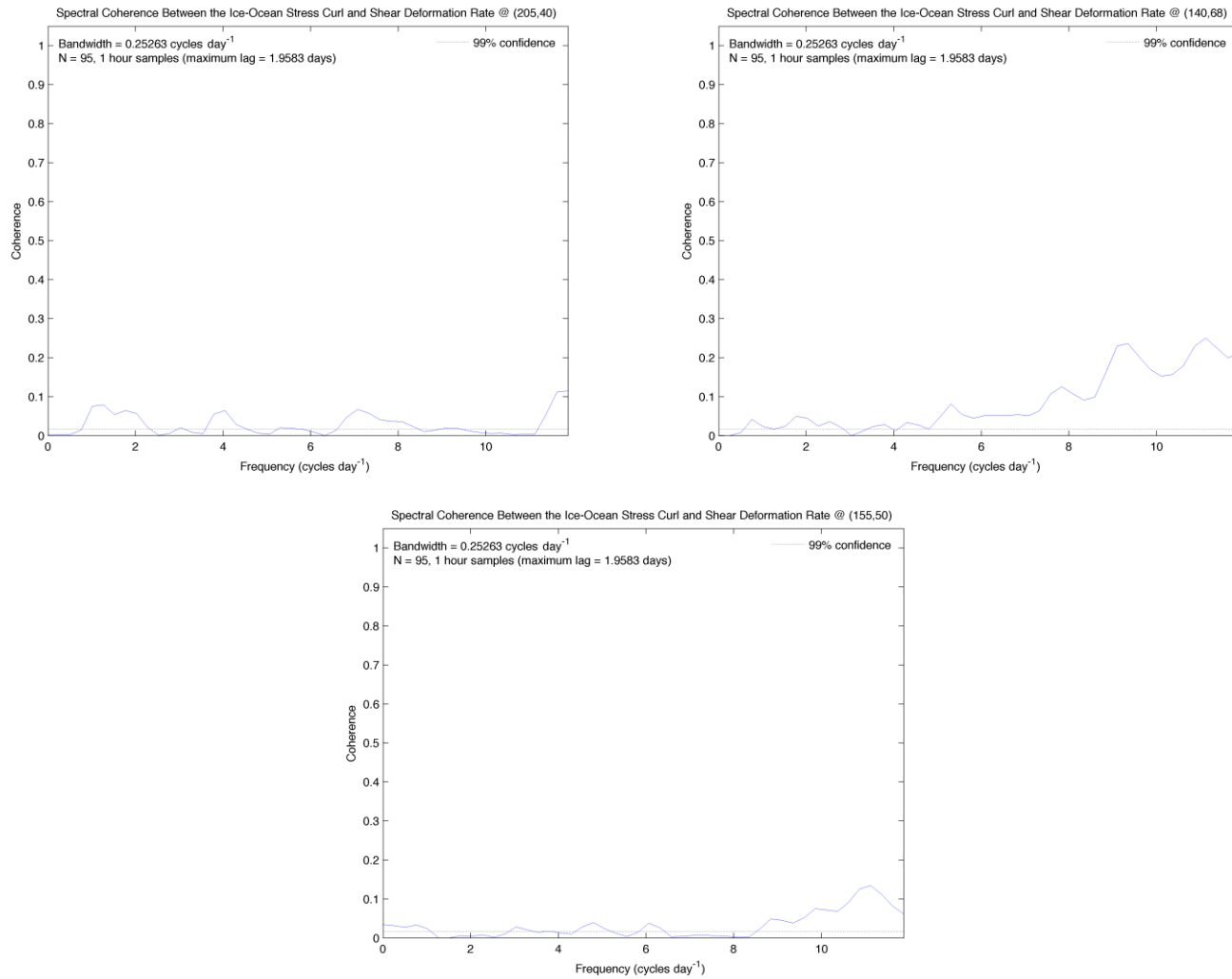
Figure 52.   Coherence between the ice-ocean stress curl and the shear deformation rate. (Upper Left) Grid point (205,40) from Case Study A. (Upper Right) Grid point (140,68) from Case Study B. (Bottom) Grid point (155,50) from Case Study C.
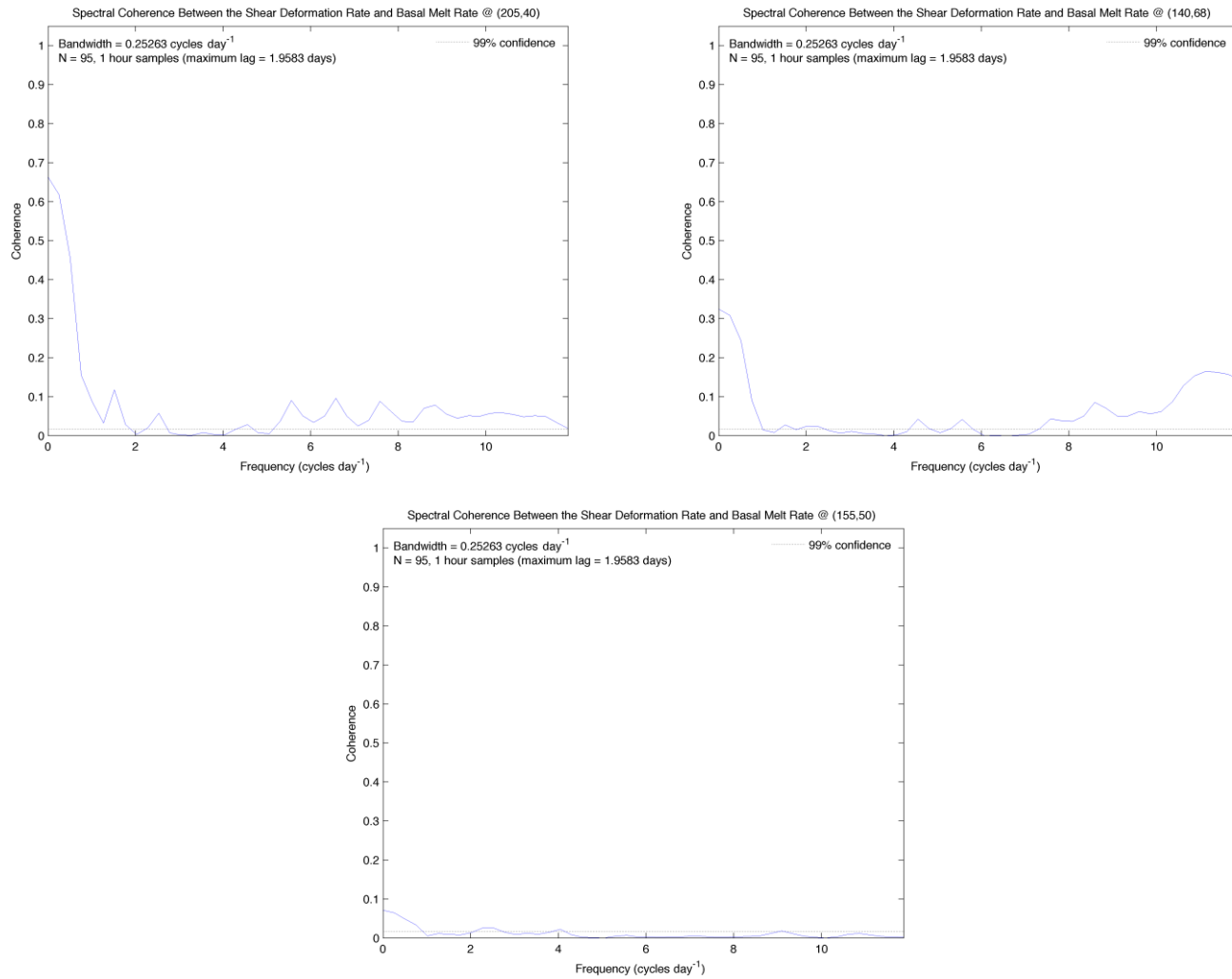
Figure 53.   Coherence between the shear deformation rate and the basal melt rate. (Upper Left) Grid point (205,40) from Case Study A. (Upper Right) Grid point (140,68) from Case Study B. (Bottom) Grid point (155,50) from Case Study C.

5. Answer to Question #2

What is the statistical prevalence of these events and their overall effect on the ice pack?

The spatial and temporal characterization of the total deformation rate of sea ice as well as the basal melt rate indicated that RASM was capable of demonstrating the power law relationship with respect to the mean total deformation rate across various spatial scales. Gradient values were consistent with previous studies. RASM was able to model this relationship despite being based on isotropic conditions and probably succeeded in doing so due to the fact that RASM is a fully coupled system model that allows for naturally occurring high frequency noise and the cascade of energy to flow between model systems. Overall, results indicated that fine temporal and spatial resolution, on a statistical scale, is important to the energy budget of the Arctic.

The hypothesized events seem to be very infrequent, spatially and temporally. This was supported not only through the time series analysis, but as well through the power spectral density calculations. There was no spectral power peak at a preferred frequency for either the ice-ocean stress curl, basal melt rate, or shear deformation rate. Additionally, coherence testing indicated little to coherence between variables. This may be a result of much more subtle events getting lost in high frequency noise and/or numerical schemes within the model that filter out these subtleties. RASM could only resolve the "extreme" events, while there may be more frequent subtle events taking place. Numerical dispersion within the models numerical scheme may also work to filter out the events and responses, which are being sought out. Overall, there is limited observations of these events due to their apparent "randomness," thus more research is necessary for a complete evaluation of the overall effect of these events on the ice pack.

VI.   CONCLUSIONS AND FUTURE RECOMMENDATIONS

A.   SUMMARY AND CONCLUSIONS

With only a single strong event ever being observed, such as that described in McPhee et al. (2005), a numerical model was best suited to evaluate how common and how important shear deformation events are to the upper ocean dynamics and overall sea ice variability. This lead to two research questions:

1.   Is a numerical model capable of representing the proposed dynamics and ice/ocean-coupling relationship for shear deformation induced upwelling?

2.   If so, what is the statistical prevalence of these events and their overall effect on the ice pack?

In order to answer the two research questions, this study analyzed the model output from a state-of-the-art high spatial and temporal resolution model known as the Regional Arctic System Model (RASM). RASM fully couples atmosphere, ocean, sea ice and land component models over a simulation domain that covers the entire pan-Arctic region. The ocean and sea ice model, within RASM, use a horizontal grid spacing of less than 10km, while the atmosphere and land component models use a horizontal grid spacing of 50 km or less. For this analysis, the temporal resolution was 1 hour. The deformation events to include shear, divergence, vorticity as well as the deformation rate were calculated from changes in the u- and v-components of the ice velocity field. The goal was to identify extreme deformation events in the ice pack that induced and upper ocean response demonstrating the tight coupling relationship between the ice and ocean.

Time series were made for variables within the ocean and sea ice for each grid point within the Beaufort Sea region. The time series were broken into three boxes leading to Case Studies A, B, and C. The boxes covered as much of the open ocean in Beaufort Sea as possible in an attempt to avoid the analysis of the thinner ice in the MIZs. Comparing still frames of the hourly time evolution of deformation events throughout the winter months to time series of the ocean response led to the positive identification of events in particular locations within the three boxes. Though many case studies were identified throughout the analysis of several RASM output sets this thesis focused

primarily on three case studies from the r30TOM6 output set which spanned from December 1, 2005 through March 31, 2006. The three case studies were presented with analyses of the upper ocean temperature structure, basal melt rate, shear, divergence, total deformation rate of sea ice and the ice-ocean stress curl.

Results indicated that, yes, these events do occur in the model. There was consistency in shear deformation events generating an upper ocean response given the correct sign of the ice-ocean stress curl. Exchange of properties across the pycnocline followed if the ice-ocean stress curl was positive, i.e., induced by counterclockwise rotation in the ice velocity field relative to the underlying ocean in the Northern Hemisphere. This lead to the question of to what extent do these events occur?

A spatial and temporal characterization of the total sea ice deformation rate was performed. This was a way of understanding the importance of fine scale events and broad scale statistics. For each of the temporal averaging cases it was found that as the scale length decreased larger strain rates became more apparent. The mean deformation rate, D, was found to scale logarithmically with the length scale, L, such that the exponent H represented the gradient of the mean deformation rate. As the temporal scale used for averaging increased so did the rate of change of the deformation at larger spatial scales. The comparison of the results to other studies was favorable and consistent given the method of observation and the respective spatial and temporal resolutions involved. Though Girard et al. (2009) was not able to simulate the power law relationship using the LIM model, RASM simulated this relationship well. The difference in results is probably due to the fully coupled system approach of RASM, which allows for naturally occurring high frequency noise and the cascade of energy to flow between model systems. The same sort of characterization analysis was also done for the basal melt rate yielding similar results. Overall, results indicated that fine temporal and spatial resolution, on a statistical scale, are very important for the overall energy budget of the Arctic.

Power spectral density analysis for individual model grid points indicated that there was no spectral peak at a preferred frequency for either the ice-ocean stress curl, basal melt rate, or shear deformation rate. The infrequency of these events based on the time series analysis along with the spectral density results indicated a temporal

122

"randomness" to these events. This could also be due that fact that these events may be more dominant at a higher frequency and are not apparent in the spectra because they may be lost in the naturally occurring high frequency noise. The numerical scheme in the model may also be working to filter these subtle events out through numerical diffusion, as mentioned with regard to ocean time stepping in Chapter IV. Additionally, coherence testing indicated little to no coherence between the aforementioned variables, thus, there was little to no strength of association between the variables where the possible dependence between them could have been in simultaneous values or leading, lagged or smoothed relationships.

Overall, yes, the hypothesized events occur and are represented in the model. Exchange of properties across the pycnocline follows if the ice-ocean stress curl is positive. Simulated events seem to be very infrequent, spatially and temporally, but may be a result of much more subtle events getting lost in high frequency noise and/or numerical schemes within the model that filter out these subtleties. The model can only resolve the "extreme" events. Numerical dispersion within the model may also work to filter out the events and the responses, which are being sought out. There are limited observations due to the "randomness" of these events, thus more research is necessary for a complete evaluation of the overall effect of these events on the ice pack.

B.   FUTURE RECOMMENDATIONS FOR RESEARCH

This study was able to demonstrate that shear deformation events resulting in the upwelling of the Arctic pycnocline are represented in RASM. The spatial and temporal characterization of the total sea ice deformation rate indicated that fine temporal and spatial resolution, on a statistical scale, are very important for the overall energy budget of the Arctic. More frequent and subtle events were not observed. Results indicated this could be the result of naturally occurring high frequency noise or numerical dispersion within the model. Further research is needed to evaluate the potential for subtle and more frequent events that may have important influences on the overall Arctic sea ice variability. These dynamics may be important in the current observed rate of decline of sea ice.

Additionally, this study evaluated timeframes (the 1990s) in which the overall sea ice thickness distribution was much different than it has been recently observed. Future studies could use this same methodology in order to evaluate the intensity, frequency distribution, and impact of these events within the currently observed sea ice thickness distribution.

On a broader scale, if sea ice deformations are an important factor shaping current sea ice variability and decline, GCMs would not be able represent these processes and thus their climate predictions would be incomplete. The question remains how important these processes are when it comes to climate prediction and further research is needed to continue to investigate the relationship.

C.   BROADER SCALE CONCLUSIONS FROM RESEARCH

Titley and St. John (2010) described Arctic security considerations relevant to the United States and more specifically the USN. Admiral Titley was the Oceanographer of the Navy and director of TFCC at the time. The publication made the connection between security concerns in the region with the USNs role and the USN Arctic roadmap. It was noted that although estimates for when the Arctic will experience ice-free conditions in the summer ranged from 2013 to 2060, the consensus of most models and researchers is that the Arctic will experience ice-free conditions for a portion of the summer by 2030. This is consistent with findings previously discussed in Stroeve et al. (2012), in which GCM output of sea ice extent projections were compared to observational data.

Maslowski et al. (2012), on the other hand, offered projections for ice-free conditions as early as 2016 +/- 3 years, based on the decline of sea ice volume from observations and model output. It has been previously argued that the decline in sea ice volume is a more complete measure of the state of sea ice and that it should be used in place of sea ice extent to better project future ice conditions. Additionally, the NAME model used in Maslowski et al. (2012) was of considerably higher resolution and much more capable of resolving features and processes that are of critical importance to the Arctic system. If you are missing a major pattern in circulation, how well is the overall circulation in the model represented? Specific to this study, if sea ice deformations are an

important factor shaping current sea ice variability and decline, how can we use GCMs that are not capable of resolving these processes to make climate projections into the future as well as base defense resource decisions on them? Thus, I would tend to lean toward projections closer to the lower bound of ~2016 offered by Maslowski et al. (2012).

Regardless, the uncertainty in projections tells us that we still have much to learn and understand about Arctic air/sea/ice interactions and more research is needed to truly understand the complex environmental system. The USN, and more specifically TFCC, has done a very thorough job, through CBAs, in identifying this shortcoming and is working to advocate for funding where necessary in order to learn more and overcome capability gaps. This uncertainty in the science, results in a military strategic uncertainty, as systems planning, acquisition and procurement processes are based of the scientific projections. When the scientific projections continue to have uncertainty, future military operations in the Arctic and levels of readiness and preparation needed become increasingly unclear.

While money has yet to be allocated for the development of future ice-strengthened surface ships or ice breakers, other countries such as Russia, China, South Korea and Ukraine have already laid plans to develop their own fleet of strengthened ships (Kent 2012). Titley and Freeman (2012) noted that, in a time of diminished federal funding it is essential that the USN spend budget funding with considerable care. The USN does not want to spend money well ahead of need nor does it want to leave itself unprepared for the future. This requires a better understanding of nature, timing and climate change in order to invest to appropriate amount at the appropriate time.

It can be argued that the rate of sea ice decline has been under-predicted by GCMs for years and thus using averages from their projections would also under-predict the timeframe in which ice-free summers may occur. What if ice-free summers come well before 2030? How will the USN maintain its strategic objectives for the Arctic if they are not capable of operating there until after 2030? Reliance on the USCG and other countries? Systems planning, acquisition and procurement processes do not have the flexibility built in to them in order to adjust to a dramatic timeline shift on the order of

magnitude seen in the current range scientific projections. Though joint operations with the USCG and reliance on allies such as Canada, may be adequate for a certain amount of time, how long can the USN allow for there not to be a USN-flagged ice-capable ship to provide visible U.S. sovereign maritime presence in the region?

The point is that despite the GCM consensus and the current budgetary climate, the USN should re-evaluate current timelines for systems planning, acquisition and procurement processes and realign them with the lower bound of the scientific projections (~2016) in order to guarantee a USN presence when the "gates" to the Arctic officially open. The USN needs to be ready, sooner rather than later, and cannot afford to be late to this party, as there is too much at stake. Establishing, protecting and maintaining seaways, natural resource exploration and territorial disputes will quickly shape the long-term landscape of the far north and the U.S. needs to have a say in how it all plays out. Nobody has ever been faulted for showing up to a meeting early, but showing up late usually has repercussions.

APPENDIX A: MODEL DOMAIN, SEA ICE DEFORMATION ANALYSIS CALCULATIONS AND EXAMPLES

Model output sets taken from RASM spanned the entire Arctic Ocean. A map projection of this area can be seen in Figure 54, which shows the ice concentration and ice thickness at a particular point in time. Sea ice deformations (vorticity, shear, and divergence) were calculated using Equations 4–6 and systematically analyzed for the Beaufort Sea region of the western Arctic north of the Alaskan coast. Grid cells with sea ice concentration less than 85% were filtered out of the calculation as they are determined to be outside the ice edge in the model or in open water. The ice edge in the model domain can be seen in Figure 54 where there is a sharp change in the color from red (ice) to blue (open water). Additionally, Figure 54 shows the sea ice thickness distribution across the domain. As previously discussed, thicker ice is generally older and has a higher internal strength against fracturing or faulting. Deformations are more likely to occur in regions of thinner ice, which has lower strength and generally has faster drift rates. The RASM sea ice thickness distribution is consistent with observations from other studies that have indicated that thicker ice tends to drift and build up along the northern coast of the CAA.

The deformations were calculated at a one-hour temporal resolution for RASM output sets representing various years in the 1990s. In order to identify shearing or deformation events potentially resulting in an upper ocean response, the SLP gradient, vorticity, shear, and divergence were analyzed in reference to the sea ice drift direction by producing movies of the calculated time-series on a map projection. Figure 55 depicts two examples of the four-quadrant depiction of sea ice kinematics, at a given time, from RASM. Both figures show the sea ice drift direction overlaid with the corresponding SLP field in the upper left. The upper right shows the calculated sea ice vorticity, while the lower left and lower right show the calculated sea ice shear and divergence, respectively. The image on the left shows the sea ice kinematics under a low SLP system, while the image on the right is under a high SLP system. The deformations manifest themselves into linear kinematic features (LKFs), which are common in sea ice kinematics, but

limited spatially and temporally (Kwok et al. 2008). The LKFs are clearly defined in the figure and their evolution of growth and decay are closely tied to strong SLP gradients and storms passing through the region. It is worth noting that while all deformations (vorticity, shear, and divergence) have a similar physical structure in space, the shear deformations are defined to be greater than or equal to zero while divergence and vorticity can be positive or negative. Shear is thus associated with both divergence and convergence as well as positive and negative vorticity. This indicates not all shearing events are alike.
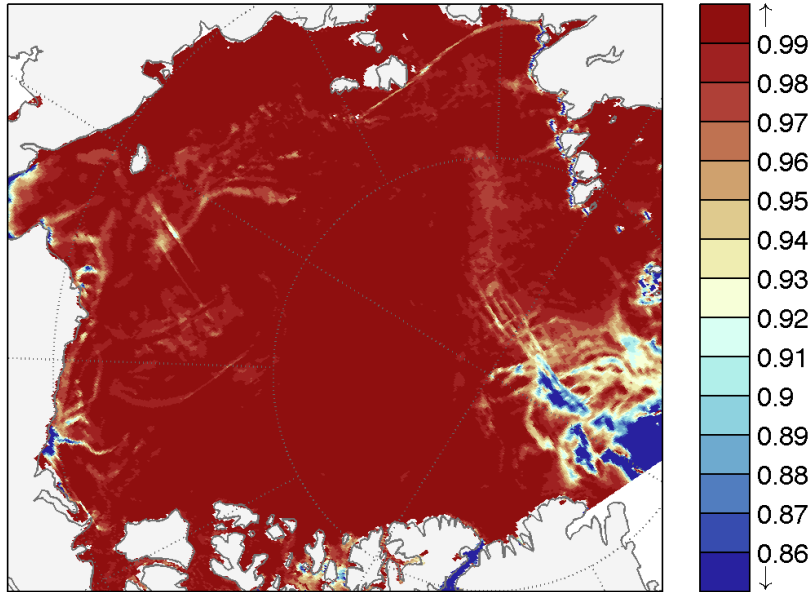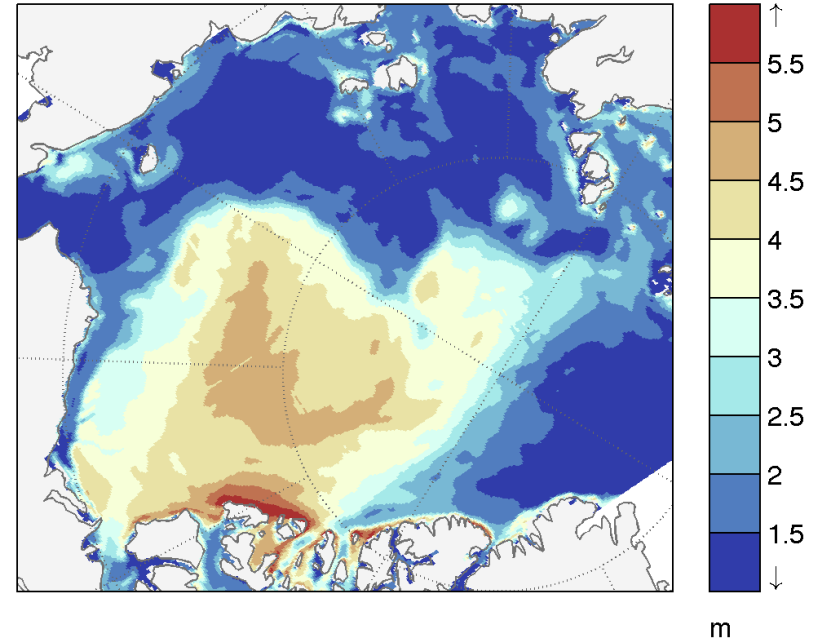
Figure 54.   (Left) Example of the sea ice concentration, a given time, within the domain used in this analysis from RASM. The area is measured by ice concentration within a gird cell. Anything below 85% is considered to be the edge of the ice pack. Beyond this ice deformation calculations are not computed. (Right) Example of the sea ice thickness, at a given time, with in the domain used in this analysis from RASM.
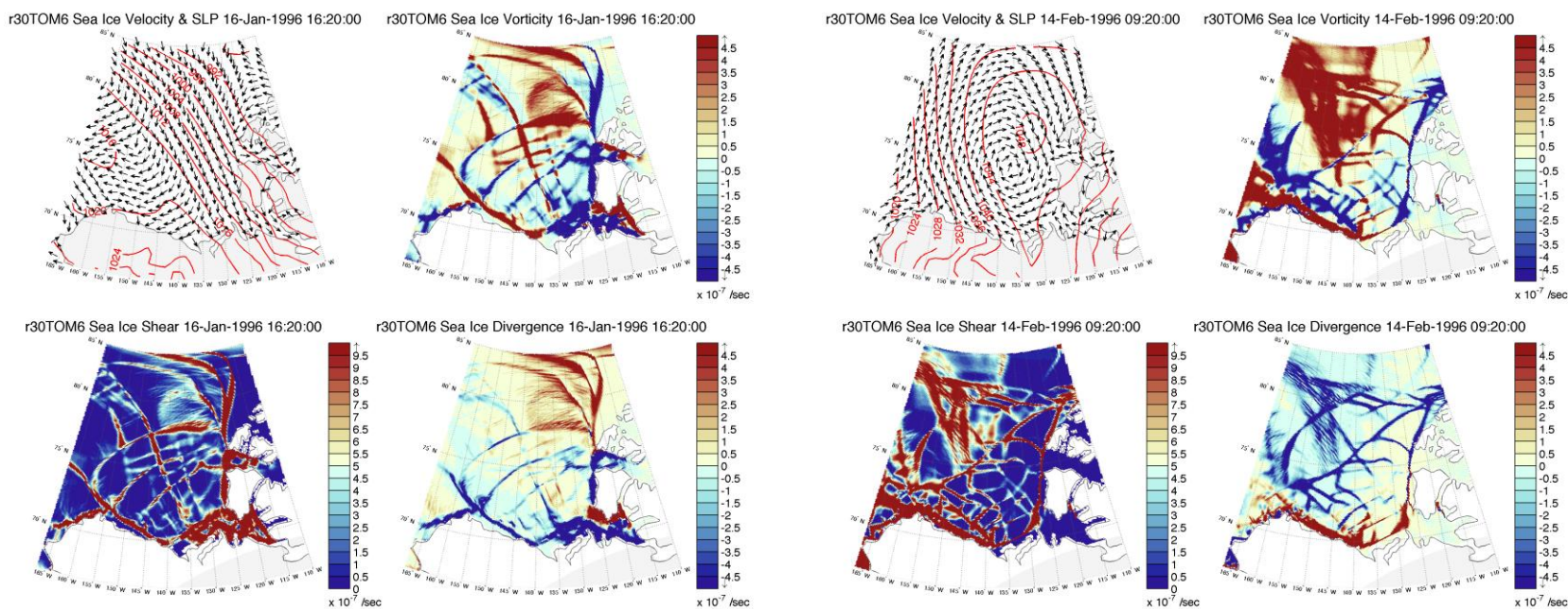
Figure 55. (Left) example of the sea ice kinematics under a low SLP system. This is a four-quadrant depiction of sea ice kinematics, at a given time, from the 1-hour temporal resolution and 9km spatial resolution output of RASM. The region analyzed is the Beaufort Sea in the western Arctic Ocean north of the Alaskan coast. The figure shows the sea ice drift direction overlaid with the corresponding SLP field in the upper left. The upper right shows the calculated sea ice vorticity, while the lower left and lower right show the calculated sea ice shear and divergence, respectively. (Right) example of the sea ice kinematics under a high SLP system. The four-quadrant structure is the same as above

APPENDIX B: INITIAL SEA ICE DEFORMATION AND UPPER OCEAN RESPONSE CASE STUDY RESULTS

The following are results from an initial methodology that led to inconclusive results, but ultimately motivated the methodology used in the primary analysis and results presented in this study.

Large magnitude or extreme deformation events, which could result in upwelling, were identified through movie runs and tagged in the time series. The temperature and salinity of the ocean were then analyzed, at the same spatial and temporal resolution, at the annotated time frames in order to identify any upper ocean response to the sea ice deformation events. Map projections were investigated at various depths as well as ocean cross-sections through the location of the deformation event were analyzed in case the map projection was inconclusive or did not offer enough insight into the possibility of an upwelling response. Though many events were investigated through many model output sets, only eight case studies are described here, as the results were fairly consistent. Each case study shows the four-quadrant depiction of sea ice deformations with SLP and sea ice drift; the map projections of the associated ocean temperatures at 12.5, 17.5, 23, and 29.7m depths; and the temperature cross-section of the upper ocean as well as its location.

Case study 1 is from December 27, 1995 and is presented in Figure 56. The case study has a temperature cross-section running approximately from west to east across the Beaufort Sea (grid cells 150–210) through the middle of the deformation events. Case study 2 is from January 30, 1996 and is presented in Figure 57 This case study has a temperature cross-section again running approximately from west to east across the Beaufort Sea (grid cells 140–205) through the middle of the deformation events. Both case studies have clear shear deformation events, but no clear response in the upper ocean to any individual event. Both show no evidence of a temperature signature with similar physical structure to the deformation events that occurred in the map projection. There is some upwelling noted in the figure, but it is likely to be from topographic interactions with the Northwind Ridge, which separates the Chukchi Shelf from the Beaufort Sea. The ocean cross-sections do show structural fluctuations in the pycnocline, but none

obviously related to the deformation events in the sea ice. Some of the inconsistencies in the pycnocline may be due to other factors or permanent/semi-permanent features in the ocean structure.

Case studies 3–5 are presented in Figure 58, 59 and 60. They span from February 11, through the 15, and 18, 1996, respectively. All three of their temperature cross-sections are from the north Alaskan coast (grid cell 70) to the middle of the Beaufort Sea (grid cell 140) through the middle of the analyzed region. All three results are the same in the fact that there does not seem to be any obvious response in the upper ocean to the individual deformation events. In fact, the three case studies are only separated out by a few days each, and the ocean structure looks to be entirely unchanged from both map projection and cross-section. These three cases do show how quickly deformation events form and decay in time as each case has a completely different physical appearance than the other two. Yet, the upper ocean shows no response to various forms of shear, divergence or vorticity. The cross-sections do show a pycnocline with some perturbations to the structure, but none collocated with the deformation events or evolving in time. This could resemble the mean ocean structure for this region throughout this winter season.

Case study 6, presented in Figure 61 has a temperature cross-section running north-south, from the north Alaskan Coast (grid cell 80) across the Beaufort Sea (to grid cell 150) through the middle of the deformation events. The clear events again result in no upper ocean response as seen in the map projection of temperatures and ocean temperature cross-section. The fluctuations in the pycnocline are again attributed to permanent/semi-permanent circulations in the Beaufort Sea, and not a result of deformation events.

Case Study #1: 27DEC1995
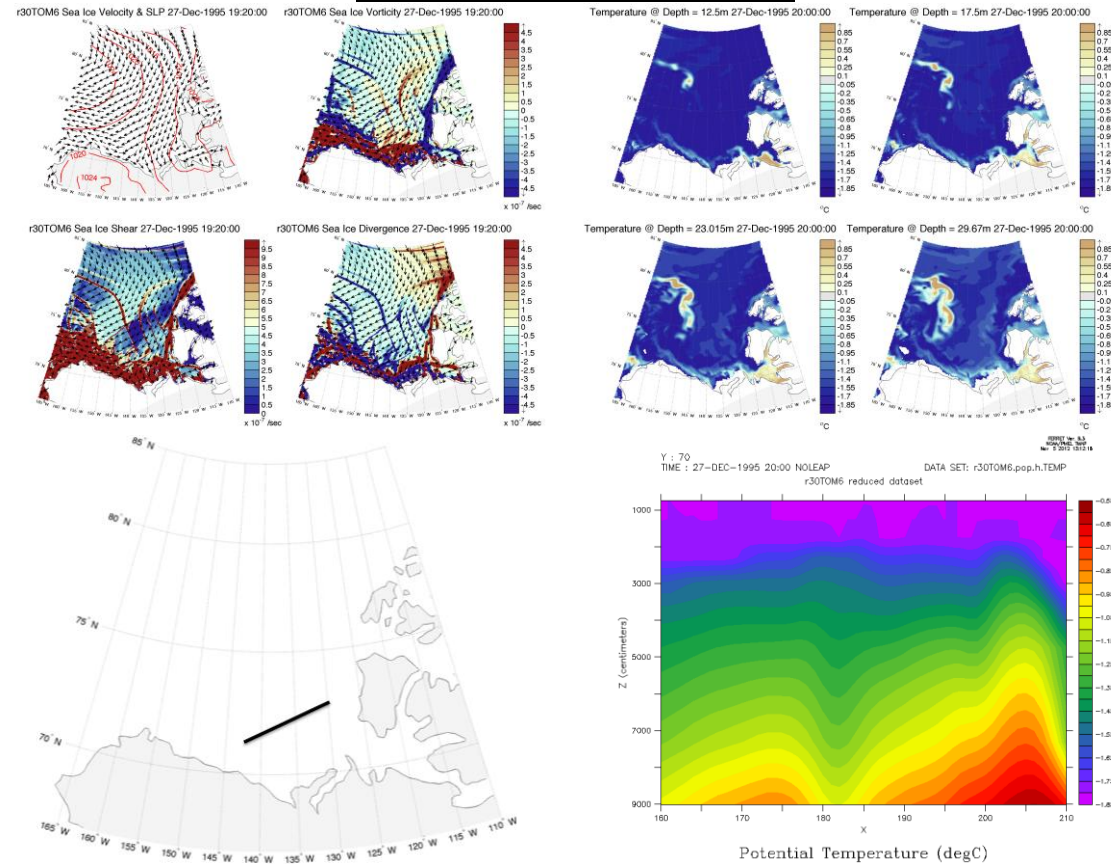
Figure 56. ((Top left) Sea ice drift direction is overlaid with the corresponding SLP field in the upper left. The upper right shows the calculated sea ice vorticity overlaid with the sea ice drift, while the lower left and lower right show the calculated sea ice shear and divergence, respectively, both overlaid with the sea ice drift. (Top right) Plan view projection of ocean temperature at 12.5, 17.5, 23, and 29.7m depths. (Bottom left) Location of ocean cross-section. (Bottom right) Ocean temperature cross-section running from west to east across the Beaufort Sea (grid cells 150–210) through the middle of the LKFs (west to east). The y-axis is depth in cm.

Case Study #2: 30JAN1996
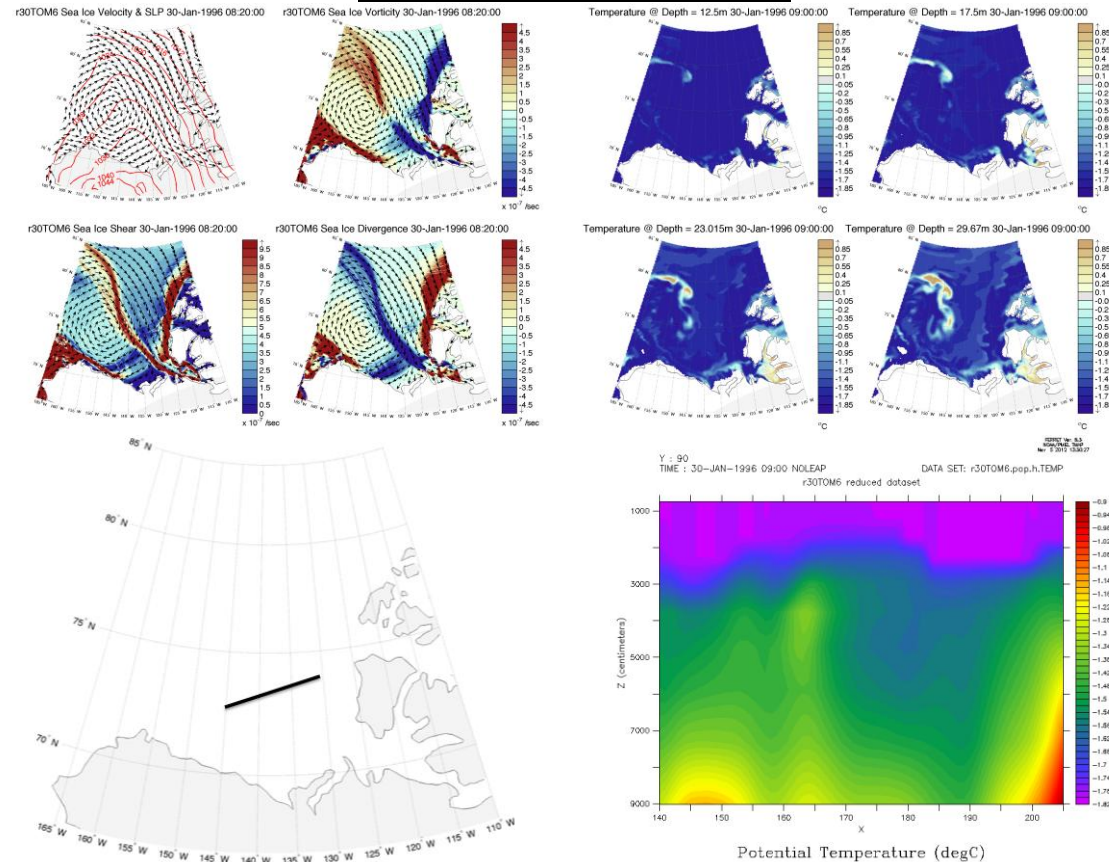
Figure 57.   (Top left) Sea ice drift direction is overlaid with the corresponding SLP field in the upper left. The upper right shows the calculated sea ice vorticity overlaid with the sea ice drift, while the lower left and lower right show the calculated sea ice shear and divergence, respectively, both overlaid with the sea ice drift. (Top right) Plan view projection of ocean temperature at 12.5, 17.5, 23, and 29.7m depths. (Bottom left) Location of ocean cross-section. (Bottom right) Ocean temperature cross-section running from west to east across the Beaufort Sea (grid cells 140–205) through the middle of the LKFs (west to east). The y-axis is depth in cm.

134

Case Study #3: 11FEB1996
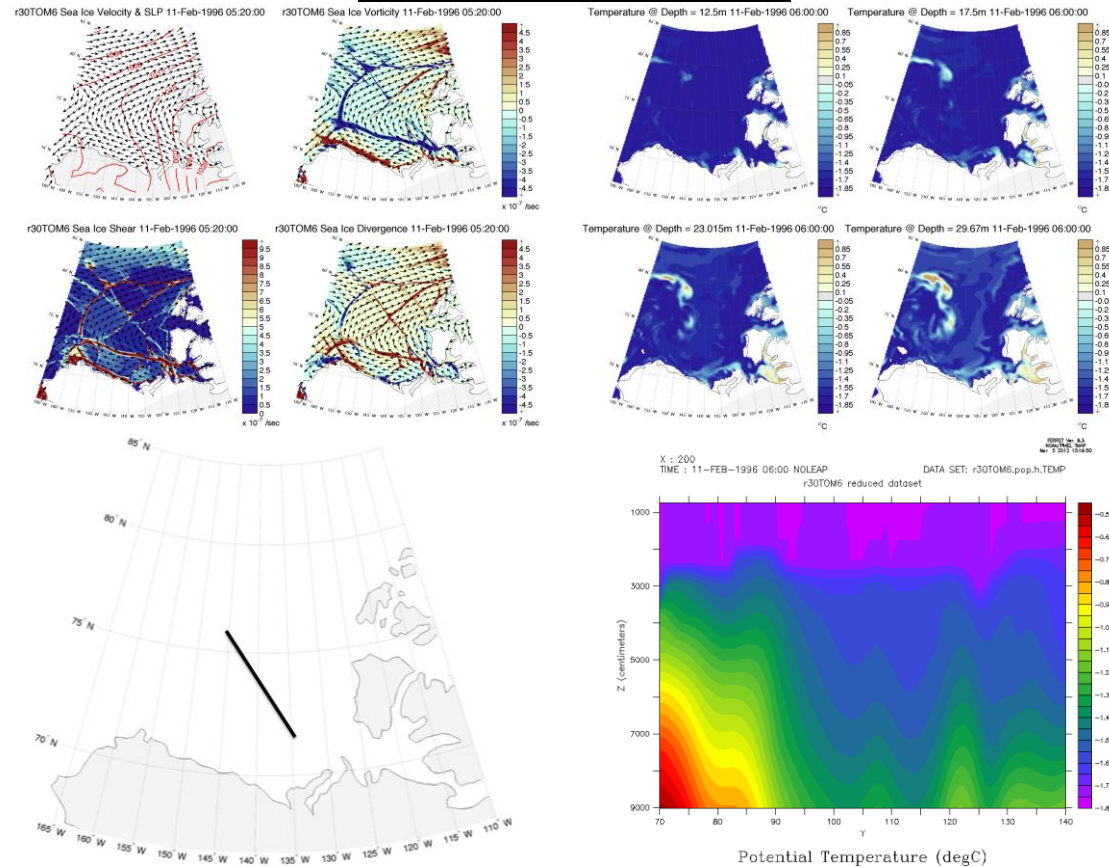
Figure 58.   (Top left) Sea ice drift direction is overlaid with the corresponding SLP field in the upper left. The upper right shows the calculated sea ice vorticity overlaid with the sea ice drift, while the lower left and lower right show the calculated sea ice shear and divergence, respectively, both overlaid with the sea ice drift. (Top right) Plan view projection of ocean temperature at 12.5, 17.5, 23, and 29.7m depths. (Bottom left) Location of ocean cross-section. (Bottom right) Ocean temperature cross-section from the north Alaskan coast (grid cell 70) to the middle of the Beaufort Sea (grid cell 140) through the middle of the analyzed region (south to north). The y-axis is depth in cm.

135

Case Study #4: 15FEB1996

Figure 59. (Top left) Sea ice drift direction is overlaid with the corresponding SLP field in the upper left. The upper right shows the calculated sea ice vorticity overlaid with the sea ice drift, while the lower left and lower right show the calculated sea ice shear and divergence, respectively, both overlaid with the sea ice drift. (Top right) Plan view projection of ocean temperature at 12.5, 17.5, 23, and 29.7m depths. (Bottom left) Location of ocean cross-section. (Bottom right) Ocean temperature cross-section from the north Alaskan coast (grid cell 70) to the middle of the Beaufort Sea (grid cell 140) through the middle of the analyzed region (south to north). The y-axis is depth in cm.

Case Study #5: 18FEB1996

Figure 60. (Top left) Sea ice drift direction is overlaid with the corresponding SLP field in the upper left. The upper right shows the calculated sea ice vorticity overlaid with the sea ice drift, while the lower left and lower right show the calculated sea ice shear and divergence, respectively, both overlaid with the sea ice drift. (Top right) Plan view projection of ocean temperature at 12.5, 17.5, 23, and 29.7m depths. (Bottom left) Location of ocean cross-section. (Bottom right) Ocean temperature cross-section from the north Alaskan coast (grid cell 70) to the middle of the Beaufort Sea (grid cell 140) through the middle of the analyzed region (south to north). The y-axis is depth in cm.

Case Study #6: 08MAR1996
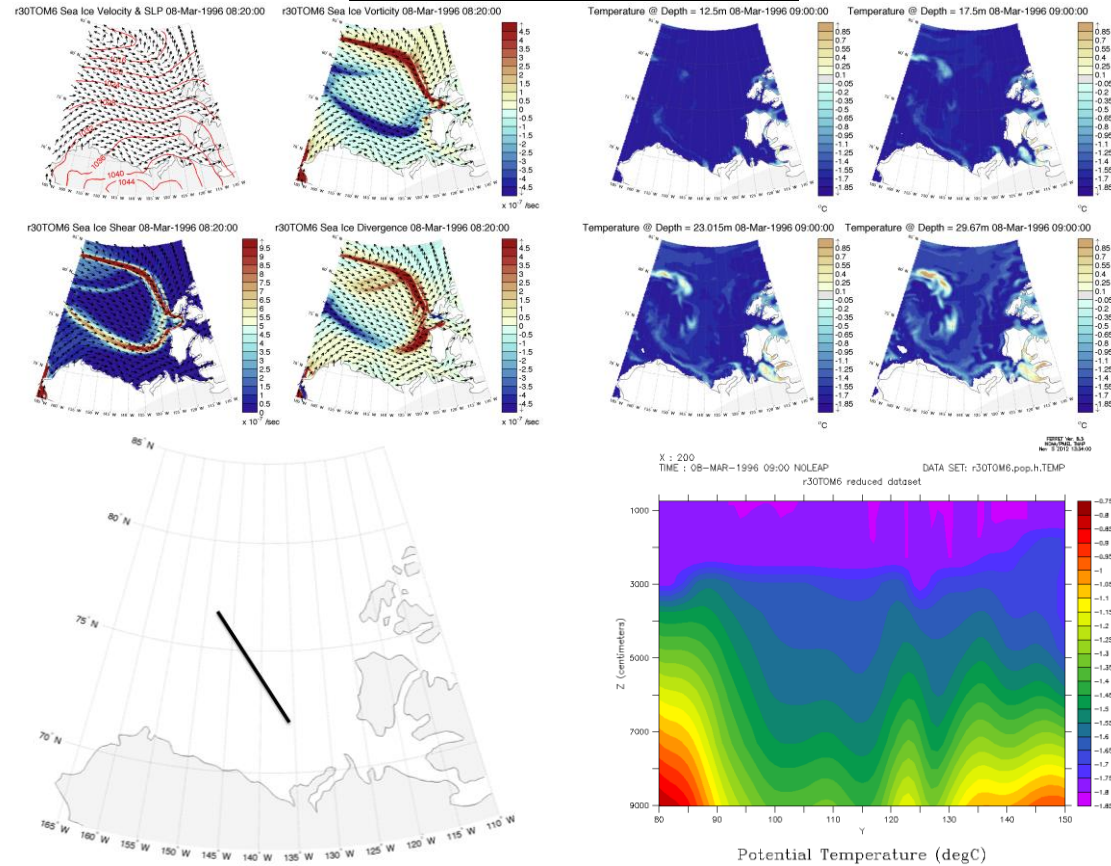
Figure 61.   (Top left) Sea ice drift direction is overlaid with the corresponding SLP field in the upper left. The upper right shows the calculated sea ice vorticity overlaid with the sea ice drift, while the lower left and lower right show the calculated sea ice shear and divergence, respectively, both overlaid with the sea ice drift. (Top right) Plan view projection of ocean temperature at 12.5, 17.5, 23, and 29.7m depths. (Bottom left) Location of ocean cross-section. (Bottom right) Ocean temperature cross-section from the north Alaskan Coast (grid cell 80) across the Beaufort Sea (to grid cell 150) through the middle of the LKFs (south to north). The y-axis is depth in cm.

138

Many other case studies (~150) displayed the same result as the first six case studies shown here, with the exception of two. Case studies 7 and 8 both yielded results with enough significance to warrant a discussion about their effect on the upper ocean and the need for further analysis. Case Study 7 is from January 17, 1996 (Figures 62–65) and also shows the four-quadrant depiction of sea ice deformations with SLP and sea ice drift. There is an obvious "cross-hatched" region of sea ice deformation, which is identified within the black oval, seen in Figure 62. The map projection of the ocean temperature, Figure 62, at various depths shows no clear indication of an anomalous upwelling resulting from the deformation events. Figure 63 depicts a zoomed in version of Figure 62. The sea ice drift in Figure 63 is color coded for magnitude, and shows in detail the shear event taking place with respect to speed and direction shifts of the ice field. Still there is no clear indication of an anomalous upwelling event resulting from the deformation events.

The ocean temperature cross-section, Figure 64, is taken from west to east (grid cell 150–220) through the middle of the deformation event and reveals a very strong upwelling in the pycnocline approximately coincident with the location of the deformation event. It is at a depth much lower than the map projections showed, thus was not noticed in the initial analysis. The upwelling is large and on the order of 10s of meters compared to the surrounding stratification levels and seems to be on the same magnitude scale as that described in McPhee et al. (2005). At first glance this appears to be an example of pycnocline upwelling due to an intense shearing event and there seems to be some indication that the hypothesized physics may be represented and resolved within the model. Furthermore, Figure 65 is a temperature profile of the ocean for the hours leading up to the intense shearing event and then after. The time evolution shows the upwelling of the pycnocline coincident with the deformation and then a decaying trend thereafter. This indicates that this was a time sensitive event.

But, when comparing this ocean temperature cross-section with other cross-sections taken at different times through the same region, a different conclusion emerges. The disturbance in the pycnocline seems to be a permanent/semi-permanent feature in this portion of the Beaufort Sea as other case studies indicate a similar ocean structure

with very differing sea ice deformation events. Case studies 1 and 2 both show cross-sections of the same region at different times and both indicate the same sort of upwelling event, without the similar deformation patterns. Other case studies, not presented here, also show the same result. This would indicate that this particular feature might be part of the ocean structure and permanent or semi-permanent to the region. The time evolution of the feature's magnitude indicates that the source producing the pattern is variable as well. This feature could be the result of subsurface currents, topographic interactions or some other dynamics not discussed here. While this was first thought to be an example of sea ice deformation induced upper ocean dynamics, it appears to be entirely coincidental that the deformation event was collocated with a semi-permanent upwelling feature in the Beaufort Sea.

The identification of this feature brings rise to questions about the feature's existence, source, variability, and potential contribution of heat advection into the upper ocean. This is beyond the scope of this analysis, but is an interesting topic that could warrant further future research.
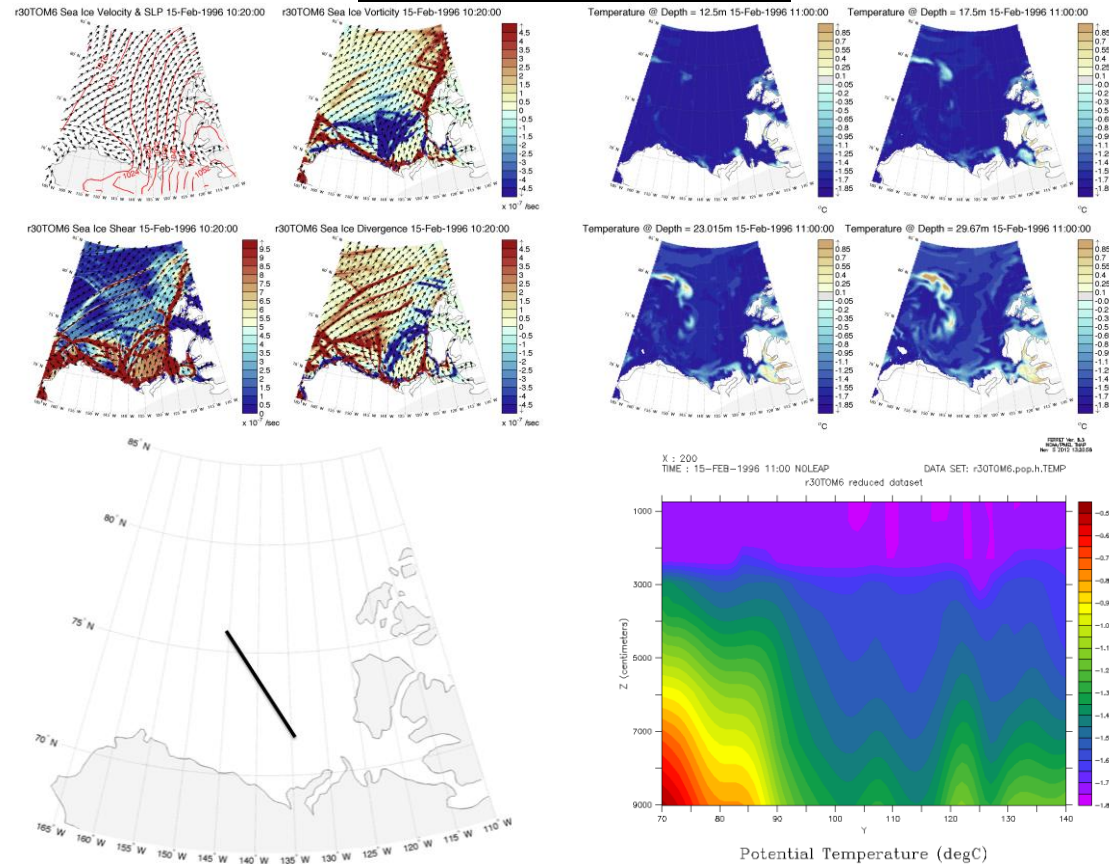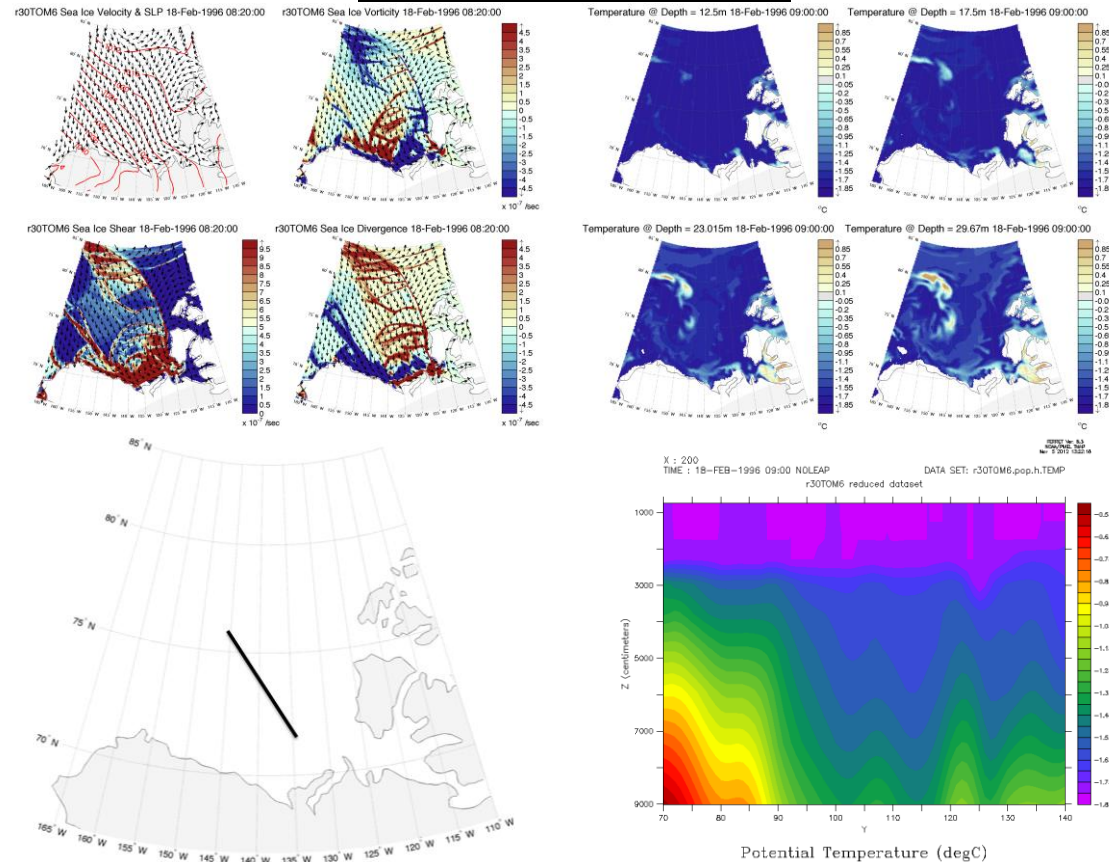
Case Study #7: 17JAN1996

Figure 62.   (Left) Sea ice drift direction is overlaid with the corresponding SLP field in the upper left. The upper right shows the calculated sea ice vorticity overlaid with the sea ice drift, while the lower left and lower right show the calculated sea ice shear and divergence, respectively, both overlaid with the sea ice drift. The region of particular interest is highlighted in the black ovals for the same location in each quadrant. (Right) Plan view projection of ocean temperature at 12.5, 17.5, 23, and 29.7m depths. The region of particular interest is highlighted in the black ovals for the same location in each quadrant.

Case Study #7: 17JAN1996

Figure 63. (Left) The zoomed in version of the sea ice drift direction overlaid with the corresponding SLP field in the upper left. The vectors are color coded to indicate the magnitude of the velocity. The upper right shows the calculated sea ice vorticity overlaid with the sea ice drift, while the lower left and lower right show the calculated sea ice shear and divergence, respectively, both overlaid with the sea ice drift. The region of particular interest is highlighted in the black ovals for the same location in each quadrant. (Right) Zoomed plan view projection of ocean temperature at 12.5, 17.5, 23, and 29.7m depths. The region of particular interest is highlighted in the black ovals for the same location in each quadrant.

Case Study #7: 17JAN1996

Figure 64.   (Left) Ocean temperature cross-section running from west to east across the Beaufort Sea (grid cells 150–210) through the middle of the LKFs (west to east). The y-axis is depth in cm. Two disturbances in the pycnocline are identified within the black ovals and correspond to the locations of the previously identified shearing events. The inset shows the location of the ocean cross-section.

Figure 65.   (Right) Temperature profile of the ocean for the hours leading up to the intense shearing event and then after. The time evolution shows the upwelling of the pycnocline coincident with the deformation and then a decaying trend thereafter.

143

Lastly, case study 8 (Figures 66 - 69) again shows the four-quadrant depiction of sea ice deformations with SLP and sea ice drift. Two strong shear events are identified within the black oval seen in Figure 66. Shortly later, the ocean temperature and salinity map projections, Figure 66, at 17.5m and 23m depth, show a "warm" temperature signature with a physical resemblance to the previously observed shearing event. It should be noted that for this case and this case only, the ocean model output was on a temporal scale of one day vice one hour. Temperature signatures like this have not yet been observed in the analysis process, thus they were an immediate indication of potential anomalous conditions. Figure 67 depicts a zoomed in version of Figure 66. The sea ice drift in Figure 67 is color coded for magnitude, and shows in detail the shearing event taking place with respect to speed and direction shifts in the ice field. The direction and magnitude of the vectors does not give a clear indication whether cyclonic or anticyclonic rotation results, which makes it difficult to directly correlate the deformation event with the coincident upper ocean dynamics. Figure 67, also shows the zoomed in version of the ocean temperature and salinity map projections, which again highlights the temperature signature in the black ovals that was previously identified.

Figure 68 is the temperature cross-section of the upper ocean, from the north Alaskan coast (grid cell 205) to the middle of the Beaufort Sea (grid cell 265). Two disturbances in the pycnocline are identified within the black ovals and correspond to the approximate locations of the previously identified shearing events. The upper ocean response to the deformation event appears to be pycnocline upwelling, which could result in heat entrainment to the underside of the sea ice and basal melting. Though this event is not on the same magnitude scale as that described in McPhee et al. (2005), there seems to be an indication that the hypothesized physics may be represented and resolved within the model. Figure 69 is a temperature profile of the ocean for the days leading up to the intense shear event and then after. Though it is subtle the time evolution shows the upwelling of the pycnocline coincident with the deformation indicating that this was a time sensitive or fine scale event.
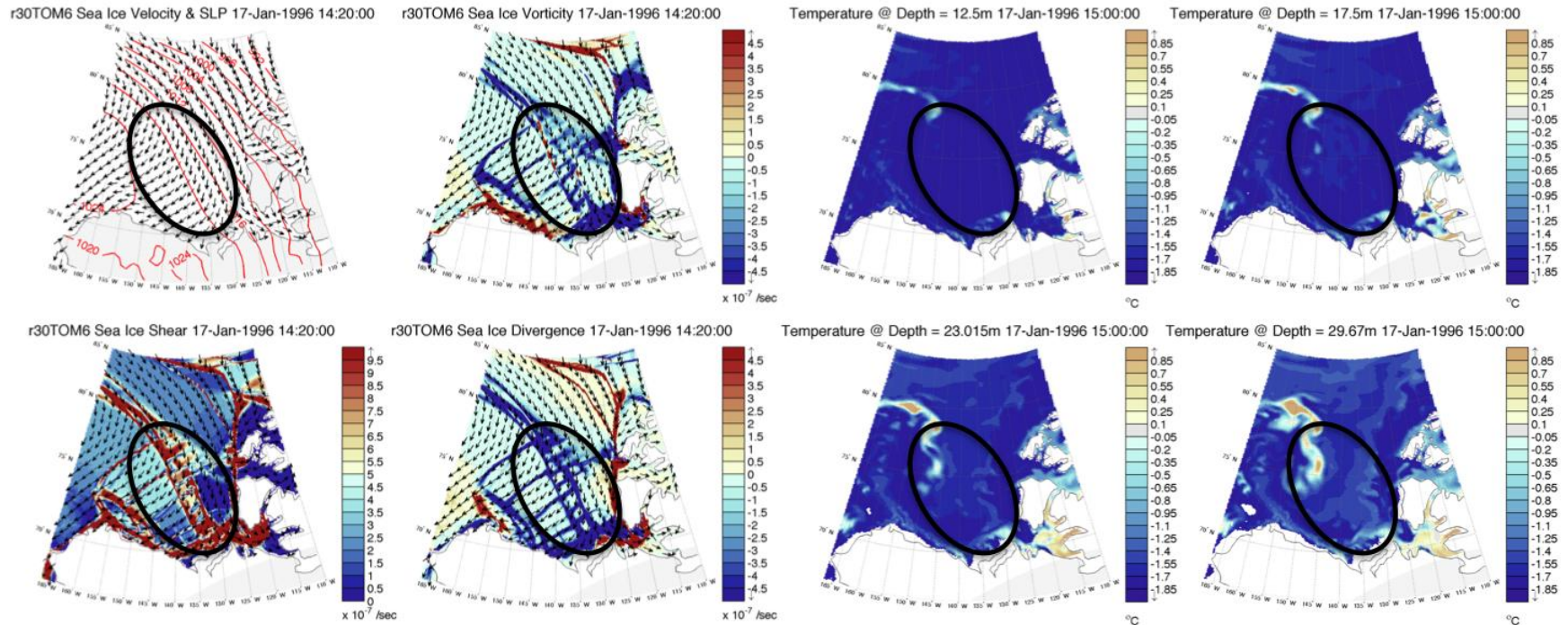
Case Study #8: 08JAN1990
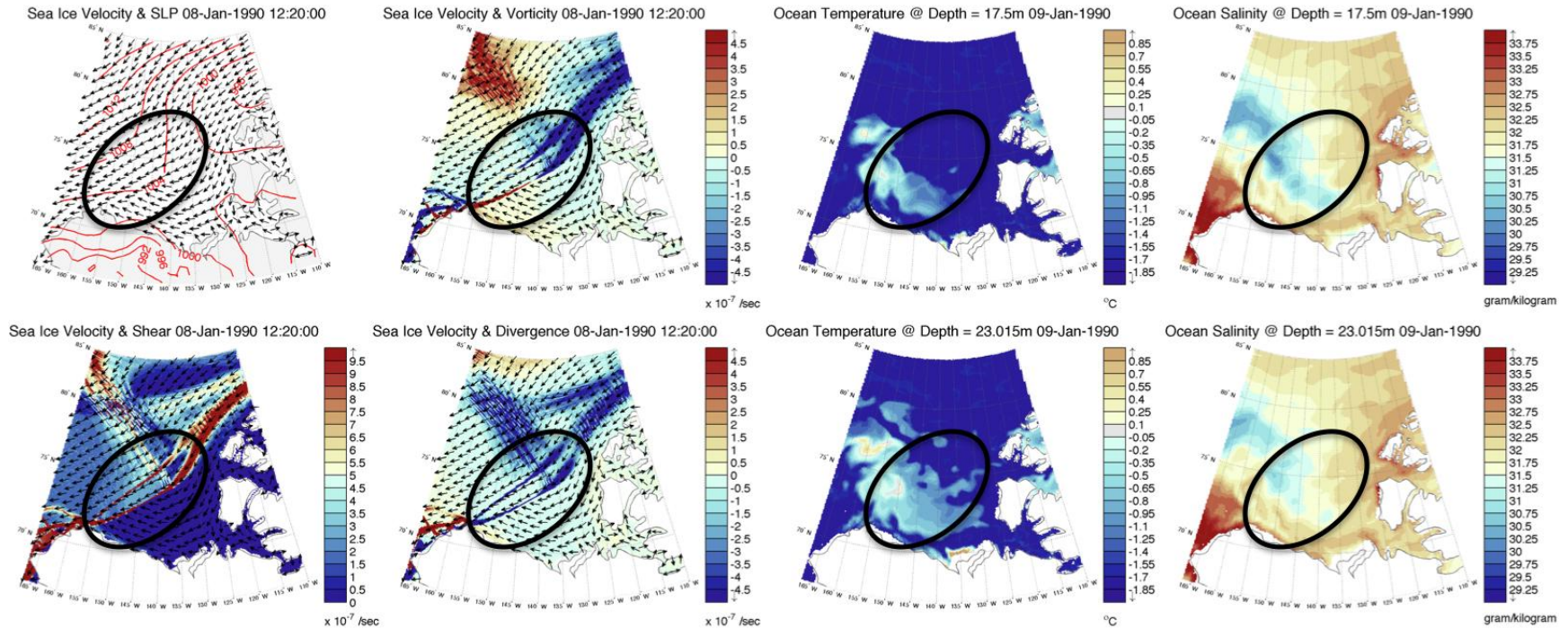
Figure 66. (Left) Sea ice drift direction is overlaid with the corresponding SLP field in the upper left. The upper right shows the calculated sea ice vorticity overlaid with the sea ice drift, while the lower left and lower right show the calculated sea ice shear and divergence, respectively, both overlaid with the sea ice drift. The region of particular interest is highlighted in the black ovals for the same location in each quadrant. (Right) Plan view projection of ocean temperature and salinity at 17.5 and 23m depths. The region of particular interest is highlighted in the black ovals for the same location in each quadrant.
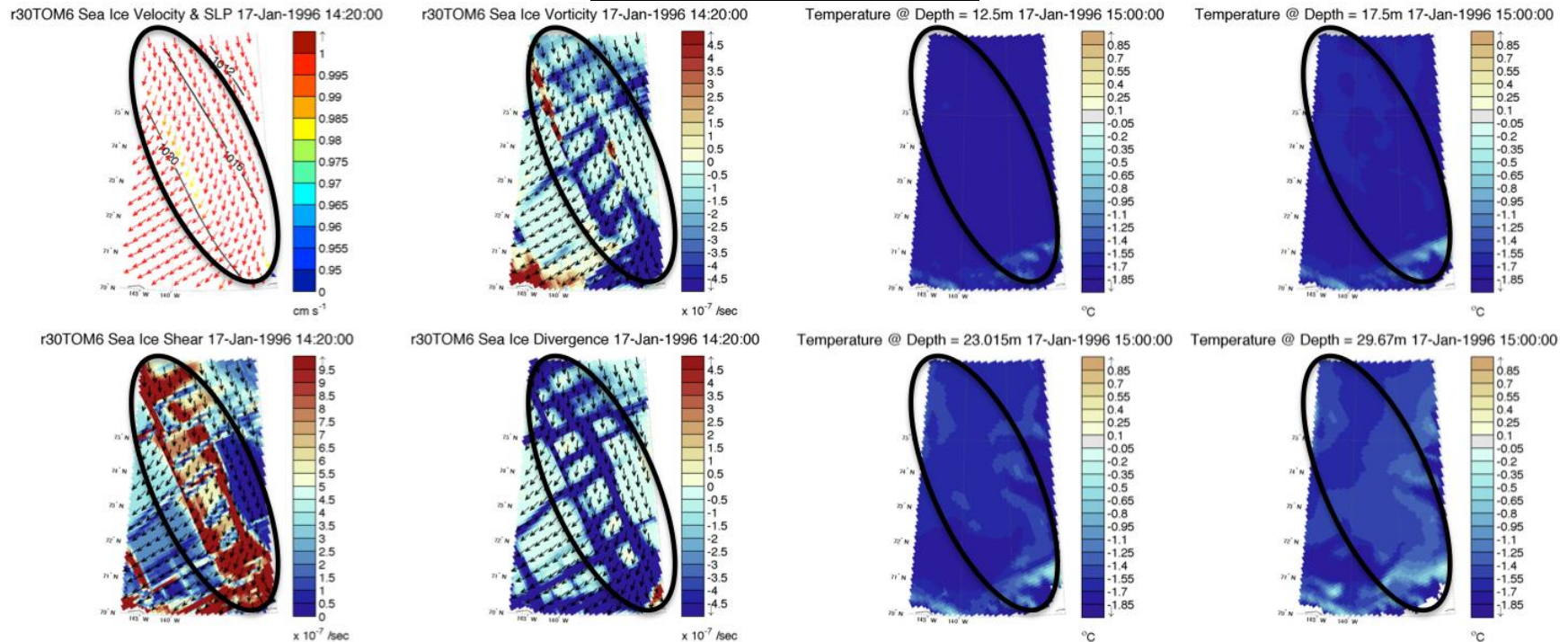
Case Study #8: 08JAN1990
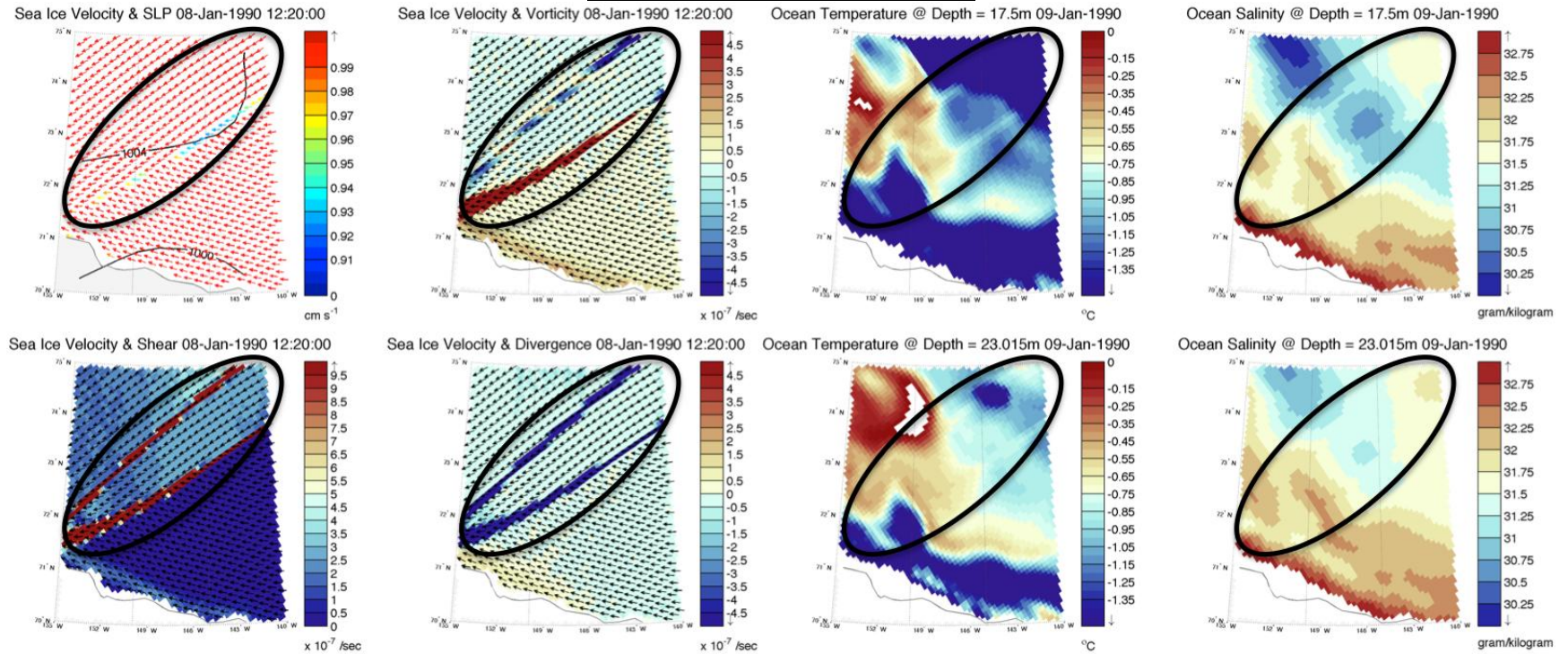
Figure 67.   (Left) The zoomed in version of the sea ice drift direction overlaid with the corresponding SLP field in the upper left. The vectors are color coded to indicate the magnitude of the velocity. The upper right shows the calculated sea ice vorticity overlaid with the sea ice drift, while the lower left and lower right show the calculated sea ice shear and divergence, respectively, both overlaid with the sea ice drift. The region of particular interest is highlighted in the black ovals for the same location in each quadrant. (Right) Zoomed plan view projection of ocean temperature and salinity at 17.5 and 23m depths. The region of particular interest is highlighted in the black ovals for the same location in each quadrant.

Case Study #8: 08JAN1990

Figure 68.   (Left) Ocean temperature cross-section of the upper ocean, from the north Alaskan coast (grid cell 205) to the middle of the Beaufort Sea (grid cell 265). The y-axis is depth in cm. Two disturbances in the pycnocline are identified within the black ovals and correspond to the locations of the previously identified shearing events. The inset shows the location of the ocean cross-section.

Figure 69.   (Right) Temperature profile of the ocean for the days leading up to the intense shear event and then after. Though it is subtle the evolution shows the upwelling of the pycnocline coincident with the deformation

Many cases were studied with no positive identification of pycnocline upwelling associated with an intense shearing event with the exception of one. The one case identified is curious as it happen to be through a POP ocean output set which had one-day temporal averaging compared to the one-hour averaging used in all other cases. Closer analysis of the shear motion was inconclusive in the sense that it was no clear whether or not the speed and directional differences would result in a cyclonic and anticyclonic response, which would indicate upwelling or downwelling. Overall, this leads to an inconclusive result and makes you wonder even if the isolated event actually occurred as a result of the deformation event or other processes.

Under the assumption that the current method of analysis has been insufficient in identifying occurrences of coincident deformation and pycnocline displacement, a different approach to the investigation is required. The results have shown the temporal frequency and spatial variation of deformation events, but has not lead to any insight into discriminating one event from another as far as which may result in a dynamical response. Deformations occur too commonly to investigate the ocean cross-section for every event and for every time slice. Thus, another approach is necessary in order to directly compare to the time evolution of multiple variables and then look at the statistical coherence of their occurrence.

APPENDIX C: TABLE OF POP OCEAN MODEL DEPTHS

Table 3.   Table of POP Ocean Model Depths

Layer	Thickness (cm)	Mid-Layer Depth (cm)
1	500	250
2	500	750
3	500	1250
4	500	1750
5	603	2301.5
6	728	2967
7	878	3770
8	1059	4738.5
9	1277	5906.5
10	15400	7315
11	1858	9014
12	2241	11063.5
13	2704	13536
14	3262	16519
15	3934	20117
16	4746	24457
17	5725	29692.5
18	6906	36008
19	8330	43626
20	10048	52815
21	12161	63919.5
22	15000	77500
23	20000	95000
24	20000	115000
25	20000	135000
26	20000	155000
27	20000	175000
28	20000	195000
29	20000	215000
30	20000	235000
31	20000	255000
32	20000	275000
33	20000	295000
34	20000	315000
35	25000	337500
36	25000	362500
37	25000	387500
38	25000	412500
39	25000	437500
40	25000	462500
41	30000	490000
42	30000	520000
43	30000	550000
44	30000	580000
45	30000	610000

THIS PAGE INTENTIONALLY LEFT BLANK

LIST OF REFERENCES

Andreadis, K., P. Storck, and D. P. Lettenmaier, 2009: Modeling snow accumulation and ablation processes in forested environments, *Wat. Resourc. Res*., **45**, W05429, doi: 10.1029/2008WR007042.

AMAP, 1998: AMAP Assessment Report: Arctic Pollution Issues. Arctic Monitoring and Assessment Programme (AMAP), Oslo, Norway. 859 pp.

Arctic Council, 1996: Declaration of the Establishment of the Arctic Council, Ottawa, Canada, 5 pp.

Arctic Marine Shipping Assessment (AMSA) 2009 Report, Arctic Council, April 2009 Retrieved from: http://www.arcticdata.is/index.php?option= com_phocadownload&view=file&id=106:sipping-routes

Arctic Observing Network (AON): 2010. Arctic Observing Network (AON) Program Status Report–2009. Results from the Third AON Principal Investigators (PI) Meeting, 30 November–2 December, 2009, Boulder, CO.

Belkin, I.M., S. Levitus, J. Antonov, and S-A Malmberg, 1998: "Great Salinity Anomalies" in the North Atlantic. *Progress in Oceanography*, **41**, 1–68.

Beszczynska-Möller, A., R.A. Woodgate, C. Lee, H. Melling, and M. Karcher, 2011: A synthesis of exchanges through the main oceanic gateways to the Arctic Ocean. *Oceanography,* **24**, 3, 82–99. Retrieved from http://dx.doi.org/10.5670/oceanog.2011.59

Bhatt, U.S., J. Zhang, C.S. Lingle, L.M. Phillips, and W.V. Tangborn, 2007: Examining Glacier Mass Balances with a Hierarchical Modeling Approach. *Computing in Science and Engineering*, **9**, 2, 60–67.

Borgerson, S. G., 2008: Arctic meltdown: the economic and security implications of global warming. *Foreign Affairs*, **8**, 63–77.

Bowling, L. C., and D. P. Lettenmaier, 2010: Modeling the Effects of Lakes and Wetlands on the Water Balance of Arctic Environments. *J. Hydrometeor*, **11**, 276–295. doi: http://dx.doi.org/10.1175/2009JHM1084.1

Broecker, W.S., 1991: The Great Ocean Conveyor, *Oceanography*, **4**, 2, 79–89.

Bromwich, D. H., K. M. Hines, and L.-S. Bai, 2009: Development and testing of Polar WRF: 2. Arctic Ocean. *J. Geophys. Res*., **114**, D08122, doi:10.1029/2008JD010300.

Carmack, E., F. McLaughlin, M. Yamamoto-Kawai, M. Itoh, K. Shimada, R. Krishfield, and A. Proshutinsky, 2008: Arctic-Subarctic Ocean Fluxes: Chapter 7 Freshwater Storage in the Northern Ocean and the Special Role of the Beaufort Gyre. *Springer*. 145–169.

Cherkauer, K. A., L. C. Bowling and D. P. Lettenmaier, 2003: Variable Infiltration Capacity (VIC) cold land process model updates, *Global and Planetary Change* **38**, 151–159.

Coachman, L.K., and C.A. Barnes, 1961: The Contribution of Bering Sea Water to the Arctic Ocean. *Arctic*. **14**, 3, 146–161.

Comiso, J.C., C.L. Parkinson, R. Gersten, and L. Stock, 2008: Accelerated decline in the Arctic sea ice cover. *Geophys. Res. Lett.* **35**, L01703, doi:10.1029/2007GL031972.

Coon, M., R. Kwok, G. Levy, M. Pruis, H. Schreyer, and D. Sulsky, 2007: Arctic Ice Dynamics Joint Experiment (AIDJEX) assumptions revisited and found inadequate, *J. Geophys. Res*., **112**, C11S90, doi:10.1029/ 2005JC003393.

Craig, T., 2012: CPL7 User's Guide. National Center for Atmospheric Research, Boulder, CO. 44 pp.

Curry, R., and C. Mauritzen, 2005: Dilution of the Northern North Atlantic Ocean in Recent Decades. *Science*, **308**, 1772, doi: 10.1126/science.1109477

Department of Defense (DoD), 2007: A Cooperative Strategy for 21st Century Seapower, 20 pp.

———, 2011: Report to Congress on Arctic Operations and the Northwest Passage, 32 pp.

Department of National Defence, 2008: Canada First Defence Strategy. 22 pp.

Derksen, and C., R. Brown, 2012: Spring snow cover extent reductions in the 2008–2012 period exceeding climate model projections. *Geophys. Res. Lett.*, **39**, L19504, doi:10.1029/2012GL053387.

———, S. L. Smith, M. Sharp, L. Brown, S. Howell, L. Copland, D. R. Mueller, Y. Gauthier, C. G. Fletcher, A. Tivy, M. Bernier, J. Bourgeois, R. Brown, C. R. Burn, C. Duguay, P. Kushner, A. Langlois, A. G. Lewkowicz, A. Royer, and A. Walker, 2012: Variability and change in the Canadian cryosphere. *Climatic Change*, **115**, 1, 59–88, doi: 10.1007/s10584–012–0470–0.

Deser, C., and H. Teng, 2008: Evolution of Arctic sea ice concentration trends and the role of atmospheric circulation forcing, 1979–2007. *Geophys. Res. Lett.*, **35**, L02504, doi:10.1029/2007GL032023.

Drobot, S., J. Stroeve, J. Maslanik, W. Emery, C. Fowler, and J. Kay, 2008: Evolution of the 2007–2008 Arctic sea ice cover and prospects for a new record in 2008. *Geophys Res Lett,* **35**, L19501, doi:10.1029/2008GL035316.

Eisenman, I., J.S. Wettlaufer. 2009: Nonlinear threshold behavior during the loss of Arctic sea ice. Proc. Natl. Acad. Sci. USA 106: 28–32.

Emery and Thomson, 2004, "Data Analysis Methods in Physical Oceanography," *Elsevier.*

Francis, J.A., and E. Hunter, 2006: New insight into disappearing Arctic sea ice. *Eos*, **87**, 46, 509–524.

Francis, J.A., and E. Hunter, 2007: Drivers of declining sea ice in the Arctic winter: a tale of two seas. *Geophys. Res. Lett.*, **34**, L17503, doi:10.1029/2007GL030995.

Francis, J. A., E. Hunter, J. R. Key, and X. Wang, 2005: Clues to variability in Arctic minimum sea ice extent, *Geophys. Res. Lett.*, **32**, L21501, doi:10.1029/ 2005GL024376.

Fowler, C., W. J. Emery, and J. Maslanik, 2004: Satellite-derived evolution of Arctic sea ice age: October 1978 to March 2003, *IEEE Geosci. Remote Sens. Lett.*, **1**, 2, 71–74, doi:10.1109/LGRS.2004.824741.

Gammelsrød, T., Ø. Leikvin, V. Lien, P. Budgell, H. Loeng, and W. Maslowski, 2009: Mass and heat transports in the NE Barents Sea: Observations and models. *J. Marine Systems*, **75**, 56–69, doi:10.1016/j.jmarsys.2008.07.010.

Gascard, J.C., J. Festy, H. Le Goff, M. Weber, B. Bruemmer, M. Offermann, M. Doble, P. Wadhams, R. Forsberg, S. Hanson, H. Skourup, S. Gerland, M. Nicolaus, J.-P. Metaxian, J. Grangeon, J. Haapala, E. Rinne, C. Haas, G. Heygster, E. Jakobson, T. Palo, J. Wilkinson, L. Kaleschke, K. Claffey, B. Elder, and J. Bottenheim, 2008: Exploring Arctic Transpolar Drift during dramatic sea ice retreat, *Eos*, **89**, 3, doi:10.1029/2008EO030001.

Geiger, C. A., and M. R. Drinkwater, 2005: Coincident buoy- and SAR-derived surface fluxes in the western Weddell Sea during Ice Station Weddell 1992, *J. Geophys. Res.*, **110**, C04002, doi:10.1029/2003JC002112.

Gill, A.E., 1982: Atmosphere-Ocean Dynamics. *Academic Press*. **30**.

Giorgi, F., 2005: Climate Change Prediction. *Climatic Change*, **73**, 239–265, doi: 10.1007/s10584–005–6857–4.

Girard, L., J. Weiss, J. M. Molines, B. Barnier, and S. Bouillon, 2009: Evaluation of high-resolution sea ice models on the basis of statistical and scaling properties of Arctic sea ice drift and deformation, *J. Geophys. Res.*, **114**, C08015, doi:10.1029/2008JC005182.

Gleckler, P.J., B. D. Santer, C. M. Domingues, D. W. Pierce, T. P. Barnett, J. A. Church, K. E. Taylor1, K. M. AchutaRao, T. P. Boyer, M. Ishii, and P. M. Caldwell1, 2012: Human-induced global ocean warming on multidecadal timescales. *Nature Climate Change*. **2**, 524–529, doi: 10.1038/NCLIMATE1553

Hawkins, E., and Sutton, R., 2009: The Potential to Narrow Uncertainty in Regional Climate Predictions. *Bulletin of the American Meteorological Society*, **90**, 8, 1095–1107, doi: 10.1175/2009BAMS2607.1

Haynes, J.E., 2010: Understanding the Importance of Oceanic Forcing on Sea Ice Variability. Advisor: W. Maslowski. Retrieved from: http://www.whoi.edu/fileserver.do?id=84184&pt=10&p=55455

Hibler III, W. D., 1979: A Viscous Sea Ice Law as a Stochastic Average of Plasticity. *J. Geophys. Lett.*. **82**, 27, 3932–3938.

———, 1979: A dynamic thermodynamic sea ice model. *Phys. Oceanogr.,* **9**, 817–846.

———, and K. Bryan, 1987. A diagnostic Ice-Ocean Model. *J. Phys. Oceanogr.*, 17, 987–1015.

Higgins, M. E., J. J. Cassano, A. Craig, W. Gutowski, J. He, J. Jakacki, D. Lettenmaier, and W. Maslowski, A. Roberts, and C. Zhu, 2012: The Regional Arctic Climate Model (RACM): Atmospheric implementation and validation, *J. Climate*, in review.

Holloway, G., F. Dupont, E. Golubeva, S. Häkkinen, E. Hunke, M. Jin, M. Karcher, F. Kauker, M. Maltrud, M. A. Morales Maqueda, W. Maslowski, G. Platov, D. Stark, M. Steele, T. Suzuki, J. Wang, and J. Zhang, 2007: Water properties and circulation in Arctic Ocean models, *J. Geophys. Res.*, **112**, C04S03, doi:10.1029/2006JC003642.

Hunke, E. C., 2001: Viscous-plastic sea ice dynamics with the EVP model: Linearization issues. *J. Comput. Phys.,* **170,** 18–38.

———, and J. K. Dukowicz, 1997: An elastic-viscous-plastic model for sea ice dynamics. J. Phys. Oceanogr., **27**, 1849–1867.

———, and W. H. Lipscomb, 2010: CICE: The Los Alamos Sea Ice Model, Documentation and Software, version 4.1., LA-CC-98–16, Los Alamos National Laboratory, Los Alamos, NM, 76 pp.

Hutchings, J.K., A. Roberts, C.A. Geiger, and J. Richter-Menge, 2011: Spatial and Temporal characterization of sea ice deformation. *Annals of Glaciology*, **52**, 57, 360–368.

Intergovernmental Panel on Climate Change (IPCC), 2007: Climate Change 2007: Synthesis Report. Cambridge University Press, 52 pp.

———, cited 2012: Organization. [Available online at: http://www.ipcc.ch/organization/organization.shtml]

Ip, C. F., W. D. Hibler, III, and G. M. Flato, 1991: On the effect of rheology on seasonal sea-ice simulations. *Ann. Glaciol*., **15**, 17–25.

Isachenkov, V., 2010: Russia Norway OK Barents Sea border in Arctic. The Associated Press. [Available online at: http://www.buffalonews.com/wire-feeds/24-hour-world-news/article190999.ece]

Jackson, J.M., E.C. Carmack, F.A. McLaughlin, S.E. Allen, and R.G. Ingram, 2010: Identification, characterization and change of the near-surface temperature maximum in the Canada Basin, 1993–2008. *J. Geophys. Res.*, **115**, C05021, doi:10.1029/2009JC005265.

———, S. E. Allen, F. A. McLaughlin, R. A. Woodgate, and E. C. Carmack, 2011: Changes to the near-surface waters in the Canada Basin, Arctic Ocean from 1993−2009: A basin in transition, *J. Geophys. Res.*, **116**, C10008, doi:10.1029/2011JC007069.

Jin, M., C. Deal, S.H. Lee, S. Elliott, E. Hunke, M. Maltrud, and N. Jeffery, 2011: Investigation of Arctic sea ice and ocean primary production for the period 1992–2007 using a 3-D global ice–ocean ecosystem model. *Deep-Sea Research II*, doi:10.1016/j.dsr2.2011.06.003

Johannessen, O.M., 2008: Decreasing Arctic sea ice mirrors increasing CO_2 on decadal time scale. *Atmospheric and Oceanic Science Letters*, **1**, 1, 51–56.

Kent, S., 2012: The world wants Canada's backyard: Russia, China, South Korea, and the Ukraine are just four countries building new ice breakers in an effort to lift their Arctic presence. The Toronto Sun. [Available online at: http://www.torontosun.com/2012/11/03/the-world-wants-canadas-backyard-kent]

Krishfield, R., J. Toole, A. Proshutinsky, and M.L. Timmermans, 2008: Automated ice-tethered profilers for seawater observations under pack ice in all seasons. *Journal of Atmospheric and Oceanic Technology*, **25**, 2091–2105.

Klauss, N., 2012: U.S. Navy lacks ability to operate in Arctic, games reveal. Kodiak Daily Mirror. [Available online at: http://www.adn.com/2012/04/28/2444408/us-navy-lacks-ability-to-operate.html]

Kovacs, A., 1996: Sea ice: Part II. Estimating the full-scale tensile, flex- ural, and compressive strength of first-year ice, Rep. 96–11, Cold Reg. Res. and Eng. Lab., Hanover, N. H., 17 pp.

Kramer, A. E., and A. C. Revkin, 2009: Arctic Shortcut Beckons Shippers as Ice Thaws. The New York Times.

Kwok, R., 2001: Deformation of the Arctic Ocean Sea Ice Cover Between November 1996 and April 1997: A Survey. IUTAM Symposium on Scaling Laws in Ice Mechanics and Ice Dynamics, *Kluwer Academic Publishers*. 315–322

———, 2006: Contrasts in sea ice deformation and production in the Arctic seasonal and perennial ice zones, *J. Geophys. Res*., **111**, C11S22, doi:10.1029/2005JC003246.

———, 2007: Near zero replenishment of the Arctic multiyear sea ice cover at the end of 2005 summer, *Geophys. Res. Lett.*, **34**, L05501, doi:10.1029/2006GL028737.

———, and G. F. Cunningham, 2008: ICESat over Arctic sea ice: Estimation of snow depth and ice thickness, *J. Geophys. Res*., **113**, C08010, doi:10.1029/2008JC004753.

———, and G. F. Cunningham, 2010: Contribution of melt in the Beaufort Sea to the decline in Arctic multiyear sea ice coverage: 1993–2009, *Geophys. Res. Lett*., **37,** L20501, doi: 10.1029/2010GL044678.

———, G.F. Cunningham, M. Wensnahan, I. Rigor, H.J. Zwally, and D. Yi, 2009: Thinning and volume loss of Arctic Ocean sea ice cover: 2003–2008. *J. Geophys. Res.*, **114**, C07005, doi:10.1029/2009JC005312.

———, E.C. Hunke, W. Maslowski, D. Menemenlis, and J. Zhang, 2008: Variability of sea ice simulations assessed with RGPS kinematics. *J. Geophys. Res.*, **113**, C11012, doi:10.1029/2008JC004783.

———, and D. A. Rothrock, 2009: Decline in Arctic sea ice thickness from submarine and ICESat records: 1958–2008, *Geophys. Res. Lett*., **36**, L15501, doi:10.1029/2009GL039035.

———, and D. Sulsky, 2010: Arctic Ocean Sea Ice Thickness and Kinematics: Satellite Retrievals and Modeling, *Oceanography*, **23**, 4.

———, N. Untersteiner, 2011: The thinning of Arctic sea ice. *Physics Today*, **64**, 36. http://dx.doi.org/10.1063/1.3580491.

Langen, P. L. and V. A. Alexeev, 2007: Polar amplification as a preferred response in an aquaplanet GCM. *Climate Dynamics,* **29**, 2–3, 305–317, doi:10.1007/ s00382–006–0221-x.

Lawrence, D.M., A.G. Slater, R.A. Tomas, M.M. Holland, and C. Deser, 2008: Accelerated Arctic land warming and permafrost degradation during rapid sea ice loss. *Geophys. Res. Lett.*, **35**, L11506, doi:10.1029/2008GL033985

Lindsay, R. W. and H. L. Stern. 2003: The RADARSAT geophysical processor system: quality of sea ice trajectory and deformation estimates. *J. Atmos. Oceanic Technol.,* **20**, 9, 1333–1347.

———, J. Zhang, and D. A. Rothrock, 2003: Sea-ice deformation rates from satellite measurements and in a model, Atmosphere-Ocean, 41, 1, 35–47, http://dx.doi.org/10.3137/ao.410103

———, and J. Zhang, 2005: The thinning of Arctic sea ice, 1988–2003: have we passed a tipping point?, *J. Climate*, **18**, 4879–4894.

Lipscomb, W. H., 2001: Remapping the thickness distribution in sea ice models. *J. Geophys. Res.*, **106**, 13989–14000.

Macdonald, R.W., F.A. McLaughlin, and E.C. Carmack, 2002: Fresh water and its sources during the SHEBA drift in the Canada Basin of the Arctic Ocean. *Deep-Sea Research Part I*, **49**, 1769–1785.

Marsan, D., H. Stern, R. Lindsay, and J. Weiss, 2004: Scale Dependence and Localization of the Deformation of Arctic Sea Ice. *Phys. Rev. Lett.*, **93**, 17, doi: 10.1103/PhysRevLett.93.178501

Maslanik, J. A., M. C. Serreze, and R. G. Barry, 1996: Recent decreases in Arctic summer ice cover and linkages to atmospheric circulation anomalies. *Geophys. Res. Lett*., **23**, 13, 1677–1680.

———, C. Fowler, J. Stroeve, S. Drobot, J. Zwally, D. Yi, and W. Emery, 2007: A younger, thinner Arctic ice cover: Increased potential for rapid, extensive sea-ice loss, *Geophys. Res. Lett*., **34**, L24501, doi:10.1029/2007GL032043.

———, J. Stroeve, C. Fowler, and W. Emery, 2011: Distribution and trends in Arctic sea ice age through spring 2011, *Geophys. Res. Lett*., **38**, LXXXXX, doi:10.1029/2011GL047735.

Maslowski, W., and W. H. Lipscomb, 2003: High resolution simulations of Arctic sea ice, 1979–1993. *Polar Research*, **22**, 1, 67–74.

———, D. Marble, W. Walczowski, U. Schauer, J. L. Clement, and A. J. Semtner, 2004: On climatological mass, heat, and salt transports through the Barents Sea and Fram Strait from a pan-Arctic coupled ice-ocean model simulation, *J. Geophys. Res.,* **109**, C03032, doi:10.1029/2001JC001039.

———, and J. Clement Kinney, 2010: Influence of oceanic circulation, heat fluxes and eddies on recent warming in the western Arctic: results of a high-resolution ice-ocean model. *J. Geophys. Res*. (in review).

———, J. Clement-Kinney, and J. Jakacki, 2007: Toward Prediction of Environmental Arctic Change, *Comp. in Sci. & Eng.*, **9**, 6, 29–34.

———, J. L. Clement Kinney, D. C. Marble, and J. Jakacki, 2008: Towards eddy-resolving models of the Arctic Ocean. *Ocean Modeling in an Eddying Regime*, Eds. M.W. Hecht and H. Hasumi, American Geophysical Union, 241–264.

———, J. Clement Kinney, M. E. Higgins, and A. Roberts (2012), Future of Arctic Sea Ice, *Annu. Rev. Earth Pl. Sc*., **40**, 625–654.

———., J. Clement Kinney, S.R. Okkonen, R. Osinski, A.F. Roberts, W. Williams, 2012b: The Large Scale Ocean Circulation and Physical Processes Controllin Pacific-Arctic Interaction, In: The Pacific Arctic Region: Ecosystem Status and Trends in a Rapidly Changing Environment, J. M. Grebmeier and W. Maslowski, eds., (in review).

———, D.C. Marble, W. Walczowski, and A.J. Semtner, 2001: On Large Scale Shifts in the Arctic Ocean and Sea Ice Conditions during 1979–1998. *Annals of Glaciology*. **33**. 545–550.

Maykut, G.A., and M.G. McPhee, 1995: Solar Heating of the Arctic Mixed Layer. *J. Geophys. Res.*, **100**, C12, 691–703.

McGeehan, T., and W. Maslowski, 2011: Impact of Shelf–Basin Freshwater Transport on Deep Convection in the Western Labrador Sea, *J. Phys. Ocean.*, **41**, 2187–2210.

———, and W. Maslowski, 2012: Evaluation and control mechanisms of volume and freshwater export through the Canadian Arctic Archipelago in a high-resolution pan-Arctic ice-ocean model, *J. Geophys. Res.*, **117**, C00D14, doi:10.1029/2011JC007261.

McPhee, M.G., 1990: Polar Oceanography, Part A: Physical Science, Chapter 6 Small-Scale Processes. *Academic Press*.

———, T. Kikuchi, J.H. Morison, and T.P. Stanton, 2003: Ocean-to-ice heat flux at the North Pole environmental observatory. *Geophys. Res. Lett*., **30**, 24, 2274, doi:10.1029/2003GL018580.

———, R. Kwok, R. Robins, and M. Coon, 2005: Upwelling of Arctic pycnocline associated with shear motion of sea ice. *Geophys. Res. Lett.,* **32**, L10616, doi:10.1029/2004GL021819.

———, A. Proshutinsky, J.H. Morison, M. Steele, and M.B. Alkire, 2009: Rapid change in freshwater content of the Arctic Ocean. Geophys. Res. Lett., 36, L10602, doi:10.1029/2009GL037525.

———, and J.D. Smith, 1976: Measurements of the Turbulent Boundary Layer under Pack Ice. *J. Phys. Ocean.*, **6**, 696–711.

———, T. P. Stanton, J. H. Morison, and D. G. Martinson, 1998: Freshening of the upper ocean in the Arctic: Is perennial ice disappearing?, *Geophys. Res. Lett*., **25**, 10, 1729–1732.

———, A. Proshutinsky, J.H. Morison, M. Steele, and M.B. Alkire, 2009: Rapid change in freshwater content of the Arctic Ocean. *Geophys. Res. Lett*., **36**, L10602, doi:10.1029/2009GL037525.

Meehl, G.A., W.M. Washington, J.M. Arblaster, A. Hu, H. Teng, C. Tebaldi, B.N. Sanderson, J.-F. Lamarque, A. Conley, W.G. Strand, J.B. White III, 2012: Climate System Response to External Forcings and Climate Change Projections in CCSM4. *J. Climate*, **25**, 3661–3683, doi: 10.1175/JCLI-D-11–00240.1.

Murnane, M., 2012: Evaluation of sea ice kinematics and their impact on ice thickness distribution in the Arctic. Advisor: W. Maslowski. Retrieved from: http://calhoun.nps.edu/public/handle/10945/6838

National Snow and Ice Data Center (NSIDC), 2007: Arctic sea ice shatters all previous record lows. Retrieved from http://nsidc.org/news/press/2007_seaiceminimum /20071001_pressrelease.html

National Snow Ice Data Center (NSIDC), 2012. Retrieved from: http://nsidc.org/

Nicolsky, D. J., V. E. Romanovsky, V. A. Alexeev, and D. M. Lawrence, 2007: Improved modeling of permafrost dynamics in a GCM land-surface scheme, *Geophys. Res. Lett.*, **34**, L08501, doi:10.1029/2007GL029525.

Nøst, O.A., P.E. Isachsen, 2003: The large-scale time-mean ocean circulation in the Nordic Seas and Arctic Ocean estimated from simplified dynamics. *J.Marine Res.,* **61**(2), pp. 175–210(36).

Oberhuber, J.M., 1993a: Simulation of the Atlantic Circulation with a Coupled Sea Ice-Mixed Layer-Isopycnal General Circulation Model. Part I: Model Description. *J. Phys. Ocean.*, **23**, 808–829.

———, 1993b: Simulation of the Atlantic Circulation with a Coupled Sea Ice-Mixed Layer-Isopycnal General Circulation Model. Part II: Model Experiment. *J. Phys. Ocean.*, **23**, 830–845.

Office of the Secretary of Defense (OSD), 2010: Quadrennial Defense Review Report, February 2010, 128 pp.

O'Rourke, R., 2011: Changes in the Arctic: Background and Issues for Congress. Congressional Research Service (CRS), 82 pp.

Overland, J. E., M. C. Spillane, D. B. Percival, M. Wang, and H. O. Mofjeld, 2004: Seasonal and regional variation of pan-Arctic surface air temperature over the instrumental record, *J. Clim.*, **17**, 3263–3282, doi:10.1175/1520–0442(2004)017<3263:SARVOP>2.0.CO;2.

———, and M. Wang, 2010: Large- scale atmospheric circulation changes are associated with the recent loss of Arctic sea ice, *Tellus*, Ser. A, **62**, 1–9, doi:10.1111/j.1600–0870.2009.00421.x.

Overpeck, J.T., M. Sturm, J.A. Francis, D.K. Perovich, M.C. Serreze, R. Benner, E.C. Carmack, F.S. Chaplin, S.C. Gerlach, L.C. Hamilton, L.D. Hinzman, M. Holland, H.P. Huntington, J.R. Key, A.H. Lloyd, G.M. MacDonald, J. McFadden, D. Noone, T.D. Prowse, P. Schlosser, and C. Vorosmarty, 2005: Arctic system on trajectory to a new, seasonally ice-free state, *Eos*, **86**, 34, 309–316.

Perovich, D. K., and B. Elder, 2002: Estimates of ocean heat flux at SHEBA. Geophys. Res. Lett., 29, 9, 1344, doi: 10.1029/2001GL014171.

———, T. C. Grenfell, B. Light, and P. V. Hobbs, 2002: Seasonal evolution of the albedo of multiyear Arctic sea ice, *J. Geophys. Res.*, **107**(C10), 8044, doi:10.1029/2000JC000438.

———, B. Light, H. Eicken, K. F. Jones, K. Runciman, and S. V. Nghiem, 2007: Increasing solar heating of the Arctic Ocean and adjacent seas, 1979–2005: Attribution and role in the ice-albedo feedback, *Geophys. Res. Lett.*, **34**, L19505, doi:10.1029/2007GL031480.

———, J.A. Richter-Menge, K.F. Jones, and B. Light, 2008: Sunlight, water and ice: extreme Arctic sea ice melt during the summer of 2007. *Geophys. Res. Lett.*, **35**, L11501, doi:10.1029/2008GL034007.

Priestley, 1981, "Spectral Analysis and Time Series," *Academic Press*.

Proshutinsky, A., R. H. Bourke, and F. A. McLaughlin, 2002: The role of the Beaufort Gyre in Arctic climate variability: Seasonal to decadal climate scales, *Geophys. Res. Lett.*, **29**, 23, 2100, doi:10.1029/2002GL015847.

———, and M.A. Johnson, 1997: Two circulation regimes of the wind-driven Arctic Ocean. *J. Geophys. Res.*, **102**, C6, 12493–12514.

———, R. Krishfield, M.-L. Timmermans, J. Toole, E. Carmack, F. McLaughlin, W.J. Williams, S. Zimmerman, M. Itoh, and K. Shimada, 2009: Beaufort Gyre freshwater reservoir: state and variability from observations. *Journal of Geophysical Research*, **114**, C00A10, doi:1029/2008JC005104.

Rampal, P., J. Weiss, C. Dubois, and J.-M. Campin: 2011 IPCC climate models do not capture Arctic sea ice drift acceleration: Consequences in terms of projected sea ice thinning and decline, *J. Geophys. Res.*, **116**, C00D07, doi:10.1029/2011JC007110.

———, J. Weiss, and D. Marsan, 2009: Positive trend in the mean speed and deformation rate of Arctic sea ice, 1979–2007, *J. Geophys. Res*., **114**, C05013, doi:10.1029/2008JC005066.

———, J. Weiss, D. Marsan, R. Lindsay, and H. Stern (2008), Scaling properties of sea ice deformation from buoy dispersion analysis*, J. Geophys. Res.*, **113**, C03002, doi:10.1029/2007JC004143.

Rawlins, M.A., M Steele, M.M. Holland, J.C. Adam, J.E. Cherry, J.A. Francis, P.Y. Groisman, L.D. Hinzman, T.G. Huntington, D.I. Kane, J.S. Kimball, R. Kwok, R.B. Lammers, C.M. Lee, D. P. Lettenmaier, K.C. McDonald, E. Podest, J.W. Pundsack, B. Rudels, M.C. Serreze, A. Shiklomanov, Ø. Skagseth, T.J. Troy, C.J. V □örösmarty, M. Wensnahan, E.F. Wood, R. Woodgate, D. Yang, K. Zhang, and T. Zhang, 2010: Analysis of the Arctic System for Freshwater Cycle Intensification: Observations and Expectations. *J. Climate*. **23**, 5715–5737, doi: 10.1175/2010JCLI3421.1.

Richter-Menge, J.A., D.K. Perovich, B.C. Elder, K. Claffey, I. Rigor, and M. Ortmeyer, 2006: Ice mass-balance buoys: a tool for measuring and attributing changes in the thickness of the Arctic sea-ice cover. *Annals of Glaciology*, **44**, 205–210.

Rigor, I. G., R.L. Colony, and S. Martin, 2000: Variations in Surface Air Temperature Observations in the Arctic, 1979–97. *J. Climate*, **13**, 896–914.

———, J. M. Wallace, and R.L. Colony, 2002: Response of Sea Ice to the Arctic Oscillation. *J. Climate*, **15**, 2648–2663.

———, and J. M. Wallace, 2004: Variations in the age of Arctic sea-ice and summer sea-ice extent, *Geophys. Res. Lett*., **31**, L09401, doi:10.1029/2004GL019492.

Rind, D., R. Healy, C. Parkinson, and D. Martinson, 1995: The role of sea ice in 2 CO2 climate model sensitivity. Part I: The total influence of sea ice thickness and extent. *J. Climate*. **8**, 449–463.

Rinke, A., K. Dethloff, J.J. Cassano, J.H. Christensen, J.A. Curry, P. Du, E. Girard, J.-E. Haugen, D. Jacob, C. G. Jones, M. Køltzow, R. Laprise, A.H. Lynch, S. Pfeifer, M. C. Serreze, M. J. Shaw, M. Tjernström, K. Wyser, and M. Zagar, 2006: Evaluation of an ensemble of Arctic regional climate models: spatiotemporal fields during the SHEBA year. *Climate Dynamics*, **26**, 459–472, doi: 10.1007/s00382–005–0095–3

———, W. Maslowski, K. Dethloff, and J. Clement, 2006b: Influence of sea ice on the atmosphere: A study with an Arctic atmospheric regional climate model, *J. Geophys. Res., 111*, D16103, doi:10.1029/2005JD006957.

Roberts, A., 2012: Introduction to the geophysics of sea ice Part 3: Sea ice dynamics. *Naval Postgraduate School*, OC3212 Lecture Series.

———, A. Hinzman, J.E. Walsh, M. Holland, J. Cassano, R. Doscher, H. Mitsudera, and A. Sumi, 2010: A science plan for regional Arctic system modeling: A report to the National Science Foundation from the International Arctic Science Community, International Arctic Research Center Technical Papers 10–0001. International Arctic Research Center, University of Alaska Fairbanks.

———, J. Clement-Kinney, 2011: ICEPACK Index. *Naval Postgraduate School*.

Rothrock, D. A., 1975: The energetics of the plastic deformation of pack ice by ridging. *J. Geophys. Res., 80*, 4514–4519.

———, Y. Yu, and G. A. Maykut, 1999: Thinning of the arctic sea-ice cover, *Geophys. Res. Lett*., **26**(23), 3469–3472.

———, D.B. Percival, and M. Wensnahan, 2008: The decline in Arctic sea-ice thickness: separating the spatial, annual, and interannual variability in a quarter of a century of submarine data. *J. Geophys. Res*., **113**, C05003, doi:10.1029/2007JC004252.

——— and M. Wensnahan, 2007: The accuracy of sea ice drafts measured from U.S. Navy submarines. *Journal of Atmospheric and Oceanic Technology*, **24**, 1936–1949.

———, and J. Zhang, 2005: Arctic Ocean sea ice volume: What explains its recent depletion?, *J. Geophys. Res*., **110**, C01002, doi:10.1029/2004JC002282.

Rysgaard, S., J. Bendtsen, L. T. Pedersen, H. Ramløv, and R. N. Glud, 2009: Increased CO2 uptake due to sea ice growth and decay in the Nordic Seas, *J. Geophys. Res.*, **114**, C09011, doi:10.1029/2008JC005088.

Schauer, U., E. Fahrbach, S. Osterhus, and G. Rohardt, 2004: Arctic warming through the Fram Strait: Oceanic heat transport from 3 years of measurements, *J. Geophys. Res.*, **109**, C06026, doi:10.1029/2003JC001823.

Schulson, E. M., 2004, Compressive shear faults within arctic sea ice: Fracture on scales large and small, *J. Geophys. Res.*, **109**, C07016, doi:10.1029/2003JC002108.

SCICEX Science Advisory Committee, 2010: SCICEX Phase II Science Plan, Part I: Technical Guidance for Planning Science Accommodation Missions. U.S. Arctic Research Commission, Arlington, VA, 76pp.

Serreze, M. C., and R.G. Barry, 2005: The Arctic Climate System. *Cambridge University Press*.

———, M. M. Holland, and J. Stroeve, 2007: Perspectives on the Arctic's Shrinking Sea-Ice Cover. *Science,* **315,** 1533–1536.

———, A. P. Barrett, J. C. Stroeve, D. N. Kindig, and M. M. Holland, 2009: The emergence of surface-based Arctic amplification. *The Cryosphere* **3,** 11–19.

Shaw, W.J., T.P. Stanton, M.G. McPhee, J.H. Morison, and D.G. Martinson, 2009: Role of the upper ocean in the energy budget of Arctic sea ice during SHEBA. *J. Geophys. Res*., **114**, C06012, doi:10.1029/2008JC004991.

Shepherd, A., E. R. Ivins, A. Geruo, V. R. Barletta, M. J. Bentley, S. Bettadpur, K. H. Briggs, D. H. Bromwich, R. Forsberg, N Galin, M. Horwath, S. Jacobs, I. Joughin, M. A. King, J. T. M. Lenaerts, J. Li, S. R. M. Ligtenberg, A. Luckman, S. B. Luthcke, M. McMillan, R. Meister, G. Milne, J. Mouginot, A. Muir, J. P. Nicolas, J. Paden, A. J. Payne, H. Pritchard, E. Rignot, H. Rott, L. S. Sørensen, T. A. Scambos, B. Scheuchl, E. J. O. Schrama, B. Smith, A. V. Sundal, J. H. van Angelen, W. J. van de Berg, M. R. van den Broeke, D. G. Vaughan, I. Velicogna, J. Wahr, P. L. Whitehouse, D. J. Wingham, D. Yi, D. Young, H. J. Zwally, 2012: A reconciled Estimate of Ice-Sheet Mass Balance. *Science*, **30**, 338(6111), pp. 1183–1189. doi: 10.1126/science.1228102.

Shimada, K., T. Komoshida, M. Itoh, S. Nishino, E. Carmack, F. McLaughlin, S. Zimmerman and A. Proshutinsky, 2006: Pacific Ocean inflow: influence on catastrophic reduction of sea ice cover in the Arctic Ocean. *Geophys. Res. Lett.*, **33**, L08605, doi:10.1029/2005GL025624.

Skamarock, W. C., J. B. Klemp, J. Dudhia, D. O. Gill, D. M. Barker, W. Wang, and J. G. Powers, 2008: A Description of the Advanced Research WRF Version 3, National Center for Atmospheric Research, Boulder, Colorado, 125 pp.

Smith, R., P. Jones, B. Briegleb, F. Bryan, G. Danabasoglu, J. Dennis, J. Dukowicz, C. Eden, B. Fox-Kemper, P. Gent, M. Hecht, S. Jayne, M. Jochum, W. Large, K. Landsay, M. Maltrud, N. Norton, S. Peacock, M. Vertenstein, and S. Yeager, 2010: The Parallel Ocean Program (POP) Reference Manual. Los Alamos National Laboratory (LANL), New Mexico, 141 pp.

Spreen, G., R. Kwok, D. Menemenlis, A.T. Nguyen, 2010: Sea Ice Deformation in a Coupled Sea Ice-Ocean Model and from Satellite Remote Sensing: Comparison and Model Adaptation. *AOMIP 2011 Conference Preceding's*.

Stern, H. L., and R. W. Lindsay, 2009: Spatial scaling of Arctic sea ice deformation, *J. Geophys. Res.,* **114**, C10017, doi:10.1029/2009JC005380.

Stroeve, J., M.M. Holland, W. Meier, T. Scambos, and M. Serreze, 2007: Arctic sea ice decline: faster than forecast. *Geophys. Res. Lett.*, **34**, L09501, doi:10.1029/2007GL029703.

———, V. Kattsov, A. Barrett, M. Serreze, T. Pavlova, M. Holland, and W. N. Meier, 2012: Trends in Arctic sea ice extent from CMIP5, CMIP3 and observations, *Geophys. Res. Lett.*, **39**, L16502, doi:10.1029/ 2012GL052676.

———, J. Maslanik, M. C. Serreze, I. Rigor, W. Meier, and C. Fowler, 2011: Sea ice response to an extreme negative phase of the Arctic Oscillation during winter 2009/2010, *Geophys. Res. Lett.*, **38**, L02502, doi:10.1029/2010GL045662.

———, and W. Maslowski, 2008: Arctic sea ice variability during the last half century. *Climate Variability and Extremes During the Past 100 Years*, **33**, 2, 143–154.

Task Force Climate Change (TFCC) / Oceanographer of the Navy, 2009: U.S. Navy Arctic Roadmap, 35 pp.

———, 2010: U.S. Navy Climate Change Roadmap, 28 pp.

———, 2011a: Arctic Environmental Assessment and Outlook Report, 30 pp.

———, 2011b: Navy Arctic Capabilities Based Assessment, 104 pp.

———, 2011c: Navy Arctic Environmental Capabilities Based Assessment, 112 pp.

Thompson, D.W.J, and J.M. Wallace, 1998: The Arctic Oscillation signature in the wintertime geopotential height and temperature fields. *Geophys. Res. Lett.,* **25**, 1297–1300.

Thorndike, A.S., D.A. Rothrock, G.A. Maykut, and R. Colony, 1975: The thickness distribution of sea ice. *J. Geophys. Res.*, **80**, 33, 4501–4513.

Timmermans, M.-L., J. Toole, A. Proshutinsky, R. Krishfield, and A. Plueddemann, 2008: Eddies in the Canada Basin, Arctic Ocean, observed from ice-tethered profilers. *J. Phys. Ocean.*, **38**, 133–145.

Titley, D.W., R.S. Freeman, 2012: The U.S. Navy–Navigating Through a Changing Climate. *e-International Relations*. Retrieved from: http://www.e-ir.info/2012/03/23/the-u-s-navy-navigating-through-a-changing-climate/

———, and C.C. St. John, 2010: Arctic security considerations and the U.S. Navy's Roadmap for the Arctic. *Naval War College Review*, **63**, 35–48.

Tjernström, M., M. Zagar, G. Svensson, J.J. Cassano, S. Pfeifer, A. Rinke, K. Wyser, K. Dethloff, C. Jones, T. Semmler, and M. Shaw, 2005: Modeling The Arctic Boundary Layer: An Evaluation of Six Arcmip Regional-Scale Models Using Data From the Sheba Project. *Boundary-Layer Meteorology*, **00**: 1–45.

Toole, J.M., M.-L. Timmermans, D.K. Perovich, R.A. Krishfield, A. Proshutinsky, and J.A. Richter-Menge, 2010: Influences of the ocean surface mixed layer and thermohaline stratification on Arctic sea ice in the central Canada Basin. *J. Geophys. Res.*, **115**, C10018, doi:10.1029/2009JC005660.

Tseng, H-L.R., 2010: Toward quantifying the impact of atmospheric forcing on Arctic sea ice variability using the NPS 1/12 degree pan-Arctic coupled ice-ocean model. Advisor: W. Maslowski. Retrieved from http://edocs.nps.edu/npspubs/scholarly/theses/2010/Mar/10Mar_Tseng.pdf

Tucker, W. B., III, D. K. Perovich, A. J. Gow, W. F. Weeks, and M. R. Drinkwater, 1992: Physical properties of sea ice relevant to remote sensing, in *Microwave Remote Sensing of Sea Ice*, *Geophys. Monogr. Ser.*, vol. **68**, edited by F. D. Carsey, pp. 9–28, AGU, Washington, D. C., doi:10.1029/GM068p0009.

United Nations, 1982: The United Nations Convention on the Law of the Sea Annex 2 Article 4. United Nations Division for Ocean Affairs and the Law of the Sea. Retrieved from: https://www.un.org/depts/los/convention_agreements/texts/unclos/UNCLOS-TOC.htm

Uttal, T., J.A. Curry, M.G. McPhee, D.K. Perovich, R.E. Moritz, J.A. Maslanik, P.S. Guest, H.L. Stern, J.A. Moore, R. Turenne, A. Heiberg, M.C. Serreze, D.P. Wylie, O.G. Persson, C.A. Paulson, C. Halle, J.H. Morison, P.A. Wheeler, A. Makshtas, H. Welch, M.D. Shupe, J.M. Intrieri, K. Stamnes, R.W. Lindsey, R. Pinkel, W.S. Pegau, T.P. Stanton and T.C. Grenfeld, 2002: Surface Heat Budget of the Arctic Ocean. *Bulletin of the American Meteorological Society*, **83**, 255–275.

Vörösmarty, C.J., A.D. McGuire, and J.E. Hobbie, 2010: Scaling Studies in Arctic System Science and Policy Support. *U.S. Arctic Research Commission*. Retrieved from: http://www.arctic.gov/publications/arctic_scaling.pdf

Wadhams, P., 2000: *Ice in the Ocean*, Gordon and Breach Science Publishers, 351pp.

Walsh, J.E., W.L. Chapman, T.L. Shy, 1996: Recent Decrease of Sea Level Pressure in the Central Arctic. *J. Climate*, **9**, 480–486.

Wang, M., and J.E. Overland, 2009: A sea ice free summer in the Arctic within 30 years? *Geophys. Res. Lett.*, **36**. L07502, doi:10.1029/2009GL037820.

Wang, J., J. Zhang, E. Watanabe, M. Ikeda, K. Mizobata, J. E. Walsh, X. Bai, and B. Wu 2009: Is the Dipole Anomaly a major driver to record lows in Arctic summer sea ice extent?, *Geophys. Res. Lett*., **36**, L05706, doi:10.1029/2008GL036706.

Watanabe, E., J. Wang, A. Sumi, and H. Hasumi 2006: Arctic dipole anomaly and its contribution to sea ice export from the Arctic Ocean in the 20th century, *Geophys. Res. Lett*., **33**, L23703, doi:10.1029/ 2006GL028112.

Wei, H., W.J. Gutowski Jr., C.J. Vörösmarty, and B.M. Fekete, 2002: Calibration and Validation of a Regional Climate Model for Pan-Arctic Hydrologic Simulation. *J. Climate*, **15**, 3222–3236.

Weiss, J. D. Marsan, P. Rampal, 2009: Space and Time Scaling Laws Induced by the Multiscale Fracturing of The Arctic Sea Ice Cover. IUTAM Symposium on Scaling in Solid Mechanics, *Springer (P. Borodich Ed.) IUTAM Bookseries*, **10**, 101–109. Retrieved from: http://web.mit.edu/~rampal/rampal_homepage/Publications_files/SpaceTimeCoupling.pdf

———, E.M. Shulson, H.L. Stern, 2007: Sea ice rheology from in-situ, satellite and laboratory observations: Fracture and friction. *Earth and Planetary Science Letters*, **255**, 1–8, doi:10.1016/j.epsl.2006.11.033.

The White House, 2009: National Security Presidential Directive (NSPD-66) and Homeland Security Presidential Directive (HSPD-25). 14 pp.

Woitkowitz, J., 2012: Arctic Sovereignty and the Cold War. eHistory at The Ohio State University. Retrieved from: http://ehistory.osu.edu/osu/mmh/arctic-sovereignty/

Woodgate, R. A., K. Aagaard, and T. J. Weingartner, 2006: Interannual changes in the Bering Strait fluxes of volume, heat and freshwater between 1991 and 2004, *Geophys. Res. Lett.*, **33**, L15609, doi:10.1029/2006GL026931.

Woods Hole Oceanographic Institution (WHOI), 2007: Ice-tethered profiler. http://www.whoi.edu/itp.

Wu, B., J. Wang, and J. E. Walsh, 2006: Dipole Anomaly in the winter Arctic atmosphere and its association with Arctic sea ice motion, *J. Clim.,* **19**, 210–225, doi:10.1175/JCLI3619.1.

Yamamoto-Kawai, M., F. A. McLaughlin, E. C. Carmack, S. Nishino, K. Shimada, and N. Kurita, 2009: Surface freshening of the Canada Basin, 2003–2007: River runoff versus sea ice meltwater, *J. Geophys. Res.*, **114**, C00A05, doi:10.1029/2008JC005000.

Zhang, J., M.D. Prater, T. Rossby, 2001: Isopycnal Lagrangian statistics from the North Atlantic Current RAFOS float observations. *J. Geophys. Res.*, **106**, C7, 13817–13836.

———, Y. H. Spitz, M. Steele, C. Ashjian, R. Campbell, L. Berline, and P. Matrai, 2010: Modeling the impact of declining sea ice on the Arctic marine planktonic ecosystem, *J. Geophys. Res.*, **115**, C10015, doi:10.1029/2009JC005387.

THIS PAGE INTENTIONALLY LEFT BLANK

INITIAL DISTRIBUTION LIST

1. Defense Technical Information Center
    Ft. Belvoir, Virginia

2. Dudley Knox Library
    Naval Postgraduate School
    Monterey, California

3. Dr. Wieslaw Maslowski
    Naval Postgraduate School
    Monterey, California

4. Dr. Andrew Roberts
    Naval Postgraduate School
    Monterey, California

5. Dr. Jaclyn Clement Kinney
    Naval Postgraduate School
    Monterey, California

6. Dr. Robert Osinski
    Institute of Oceanology Polish Academy of Sciences
    Sopot, Poland

7   Dr. Miles McPhee
    McPhee Research Company
    Naches, Washington

8. RADM Jonathan White, USN
    Oceanographer and Navigator of the Navy
    Washington, DC

9. CAPT Joseph Brenner, USN
    OPNAV N2/N6E5&6, Oceanographer of the Navy Staff
    Washington, DC

10. CDR Angela Walker, USN
    Task Force Climate Change
    Washington, DC

11. CDR Blake McBride, USN
    Office of Naval Research Global–Asia
    Tokyo, Japan

12. LT Thomas J. Mills, USN
Joint Typhoon Warning Center
Pearl Harbor, HI